RPN47

EXPERIMENTAL INVESTIGATION OF HIGH-CURRENT, RELATIVISTIC ELECTRON-BEAM INTERACTIONS

PIFR-095

by

R. Block, D. Wood,
R. Busher, and D. Pellinen

February 1970

A Report to

Space and Missile Systems Command
Air Force Systems Command
Norton Air Force Base, California 94209

Under Contract AF 04(694)-901, CC N 6

Prepared by

Physics International Company
2700 Merced Street
San Leandro, California 94577

FOREWORD

This report presents the results of an effort to develop a source of electron beams that are fully diagnosed, that are more reproducible, and that have a wider range of beam parameters than previously attainable. The program was funded by the USAF Space and Missile Systems Organization under Contract AF 04(694)-901, CCN 6. The work was carried out during the period from August 1967 through August 1968. Experimental work on this contract was conducted by Messrs. L. Hatch, D. Wood, D. Pellinen, and R. Buscher.

CONTENTS

ILLUSTRATIONS

ILLUSTRATIONS (cont.)

ILLUSTRATIONS (cont.)

ILLUSTRATIONS (cont.)

ILLUSTRATIONS (cont.)

ILLUSTRATIONS (cont.)

ILLUSTRATIONS (cont.)

TABLES

SECTION I

INTRODUCTION

Uses for high current, relativistic electron beams have been rapidly increasing in recent years. High-intensity bremsstrahlung sources, thermomechanical shock simulation, and plasma heating represent currently important electron beam applications with considerable future potential. This program was authorized in response to the need for electron beams that are more fully diagnosed, are more reproducible, and are more varying in their parameters. Investigations were undertaken specifically (1) to develop more sophisticated beam diagnostics; (2) to explore the uses of shaped scattering foils in producing a variety of shaped electron beams; and (3) to study the possible use of beam-shaping magnetic fields.

The results of this work are summarized in Section II with comments concerning the direction for future work. In addition, each of the three topics above is presented in some detail in Section III.

SECTION II

SUMMARY OF RESULTS AND RECOMMENDATIONS FOR FUTURE WORK

A. DIAGNOSTICS

Devices for providing the required beam parameters to document the electron-beam environment include (1) self-integrating magnetic probes, (2) high-current Faraday cups, (3) high-voltage capacitative probes, and (4) a magnetic-spectrum analyzer (MSA). Each of these devices has subnanosecond risetime response and has been used extensively on the Model 1140 Pulserad (mean electron energy = 3 to 4 MeV). With the exception of the MSA, the devices have also been operated successfully on the Model 730 low-impedance Pulserad (mean electron energy = 0.2 to 1.0 MeV). At present, the MSA is limited to low current density, i.e., less than 500 A/cm^2, which is consistent with the Model 1140 high-energy beam current density. On the other hand, current densities of the order of 10^4 A/cm^2 are typical for low-energy, high-current beams. At these current densities, a variety of difficulties are encountered with the MSA. One such problem, thermomechanical damage to the apertures, is permanent. Another problem is plasma formation around the entrance slits, which can substantially alter the MSA entrance conditions. These problems need to be solved if the MSA or similar devices are to be used effectively on low-voltage, high-current electron beams. Future work is recommended in these areas.

Various probes developed during this program are being used routinely; they can be modified easily for specific applications where slight changes in the size of the device are required.

Urgent diagnostic requirements exist in very low-dose (< 1 cal/cm^2) and very high-dose (10^2 to 10^4 cal/g) regimes. In most cases the high-dose region implies low-energy electron beams; the basic diagnostic problem is the failure (spallation or fracture) of the absorber. Possible new techniques involve a series of simultaneous measurements, such as pinhole X-ray photographs, Faraday-cup measurements, and cross correlation of results to predict fluence profiles and electron spectra. In the low-dose region, the requirement is principally for more sensitive calorimetry.

B. BEAM SHAPING WITH FOILS

Beam scattering experiments were undertaken to check multiple-scattering theory for high current electron beams, and also to explore the use of shaped foils to obtain shaped beams. Such beams have more uniform fluence profiles for specific applications requiring larger areas for sample irradiation. The multiple-scattering experiments were performed with approximately 3.8-MeV and 1-MeV mean energy electron beams. Despite some discrepancies in the 3.8-MeV beam-scattering results, the data generally agree with scattering theory in that the mean scattering angle scales with the square root of the foil thickness. The lower-energy results, however, indicate discrepancies in even the mean-angle scaling. Since the data are generally limited, the experiments should be extended to explore these discrepancies more fully. Details of the discrepancies are discussed in Section III, B.

The shaped-foil experiments were inconclusive, primarily because variations in beam centering on the scattering foils made interpretation difficult. Better beam control has since been achieved by using a new anode-cathode configuration, so these experiments should be repeated for a more conclusive evaluation of this technique. Present evidence, however, suggests that

other approaches, such as beam shaping with a variable-diode geometry, should be evaluated also in future beam shaping studies.

C. BEAM SHAPING WITH MAGNETIC FIELDS

Experiments were conducted to discover whether more optimum shaped beams could be obtained by using a magnetic quadrupole system. The goals were (1) elliptical beams using a single quadrupole, and (2) focused, ultrahigh fluence beams using a double focusing quadrupole system. The results were:

1. Elliptical beams can be obtained with reasonable ease and offer attractive features for irradiation of long, thin targets. If injection into the quadrupole is not done carefully, however, resultant inefficiency in the beam transport diminish the total energy of the shaped beam.

2. Focused beam experiments were not successful, apparently due to the extreme sensitivity of focusing on the injection conditions and the alignment of the transport system. Conductive cones and solonoidal magnets appear more promising for future experiments desiring highly focused, reproducible electron beams.

SECTION III

TECHNICAL DISCUSSION

A. DEVELOPMENT OF DIAGNOSTICS

1. Magnetic Probe Development

a. Introduction

A fast-risetime magnetic-field probe that generates a voltage output directly proportional to the magnetic field was developed for use as a beam-current monitor on the Pulserad accelerators.

The probe is a conducting loop of wire shorted by a small resistor. If a magnetic field attempts to thread the loop, it will induce a voltage around the loop which, since the loop is virtually shorted, will cause a current to flow. This creates a magnetic field of polarity opposite to the external field. If the resistance is small, the circuit will maintain the current so that there is no net flux threading the circuit. Or

$$\phi_{ex} = \phi_s$$

where ϕ_{ex} and ϕ_s are used to denote external and self-induced components of flux, respectively. Since by definition

$$\phi = \int \vec{B} \cdot d\vec{A}$$

where $\vec{B}$ is the magnetic field intensity and $d\vec{A}$ the surface vector, and noting that inductance is defined as

$$L = \frac{\int \vec{B}_s \cdot d\vec{A}}{i}$$

where i is the current flowing in the circuit element, then we can combine the above equations

$$\phi_{ex} = Li$$

which indicates that the current flowing in the circuit is proportional to the strength of the magnetic field. This suggests that the magnetic fields can be measured directly by measuring the voltage across the resistor.

A rigorous solution, obtained from Faraday's law, is given by

$$i = \exp\left(-\frac{t}{L/R}\right) \int_o^t \left[\frac{1}{L} \frac{\partial \phi_{ex}}{\partial t} \exp\left(\frac{t}{L/R}\right)\right] dt$$

We can distinguish two limiting cases; the first where

$$\frac{L}{R} << t_o$$

and t_o is the period of the event. The solution approaches the condition for an open-circuit loop, or

$$|V| \cong \frac{\partial \phi}{\partial t}$$

In the case where $L/r >> t_o$

$$i \approx 1/L \ \phi_{ex}(t)$$

or

$$V \approx R/L \ \phi_{ex}(t)$$

Since the current flowing in the circuit is proportional to the flux threading the circuit, to monitor the magnetic flux faithfully, it is necessary only to build a nonreactive resistor.

b. Design Criteria

The design criteria for the B-probes were not arbitrary but were tailored to the requirements of the oscilloscopes used as the read-out systems and the characteristics of the pulsers.

1. Risetime

The initial criterion for risetime on the B-probe was that it should not be the limiting factor in monitoring. Since the normal coaxial cable and oscilloscope combinations have approximately a 1-nsec risetime, it is unnecessary to design or test the probes at a risetime much faster than that.

2. Decay Constant

A reasonable decay constant for a detector is 10 times the risetime to peak of the phenomenon being measured. For the Model 1150 Pulserad owned by the USAF Space and Missile Systems Organization (SAMSO) and operated by PI, this is about 50 nsec, so L/R was chosen to be about 500 nsec. To place any ringing due to transit time effects and reflections in the coil beyond the frequency response of the oscilloscope, the maximum diameter of the loop was set at 5 cm. The inductance of a single turn of wire is given by

$$L = 12.5\ a \left[\ell n \frac{169}{d} - Z \right] \text{ mH}$$

where a is the radius of the ring in cm, and d is the diameter of the wire forming the ring. For a 5-cm loop and a 1.7-mm-diam wire, the inductance is about 105 nH.

To have an L/R time constant of 500 nsec, the resistance must be about 0.2 Ω. The design parameters for the B-probe are as follows:

$$t_r < 1 \text{ nsec (risetime)}$$

$$L/R > 500 \text{ nsec (decay time)}$$

$$a = 5 \text{ cm}$$

$$R \approx 0.2 \ \Omega$$

c. Calibration

The easiest (and most economical) way to test the probes was to construct a coaxial transmission line and a reasonably high-repetition-rate pulser that would provide a fast rising, rectangular current pulse. Such a system would enable the experimenter to directly measure the risetime, transient characteristics, and decay constant of the probe, and to determine the absolute calibration of the probe in terms of voltage output as a function of magnetic field. A 13-in.-diam, 2-ft-long, 50-Ω terminated coaxial line and associated pulser were constructed and are shown in Figure 1. The pulser is shown schematically in Figure 2. It consists of a dc charged transmission line switched into a load by a mercury-wetted relay, pulsed at repetition rate of 120 Hz. The pulser risetime was less than the risetime (0.3 nsec) of any oscilloscope at Physics International Company. It is capable of delivering 750-V pulses into a 50-Ω load, such as the coaxial model. The waveform across the termination of the line-pulser combination is shown in Figure 3. The waveform on the termination indicates an e-folding risetime of the electric and magnetic fields of less than 1 nsec.

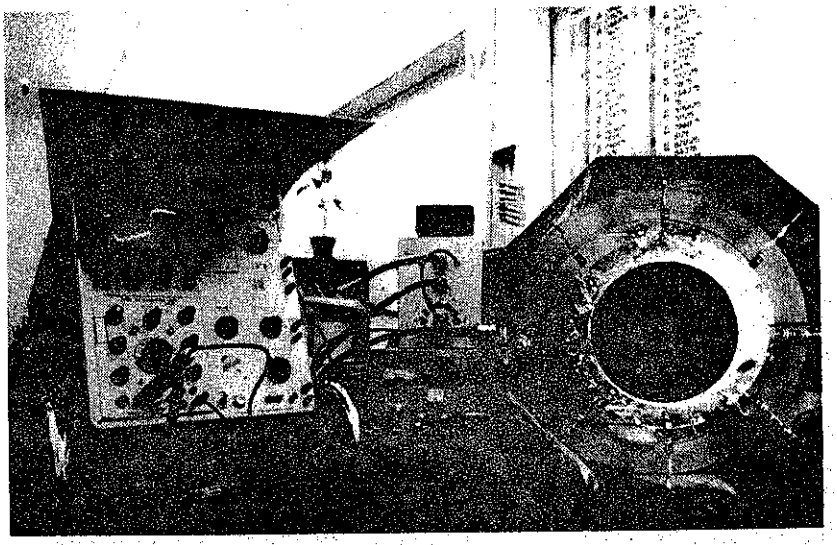

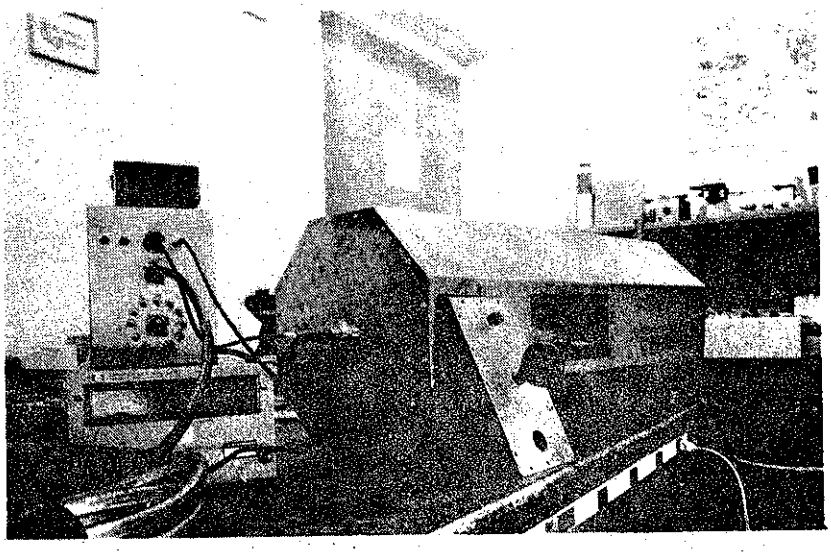

FIGURE 1. TWO VIEWS OF TRANSMISSION LINE CALIBRATION SET-UP FOR B-PROBES

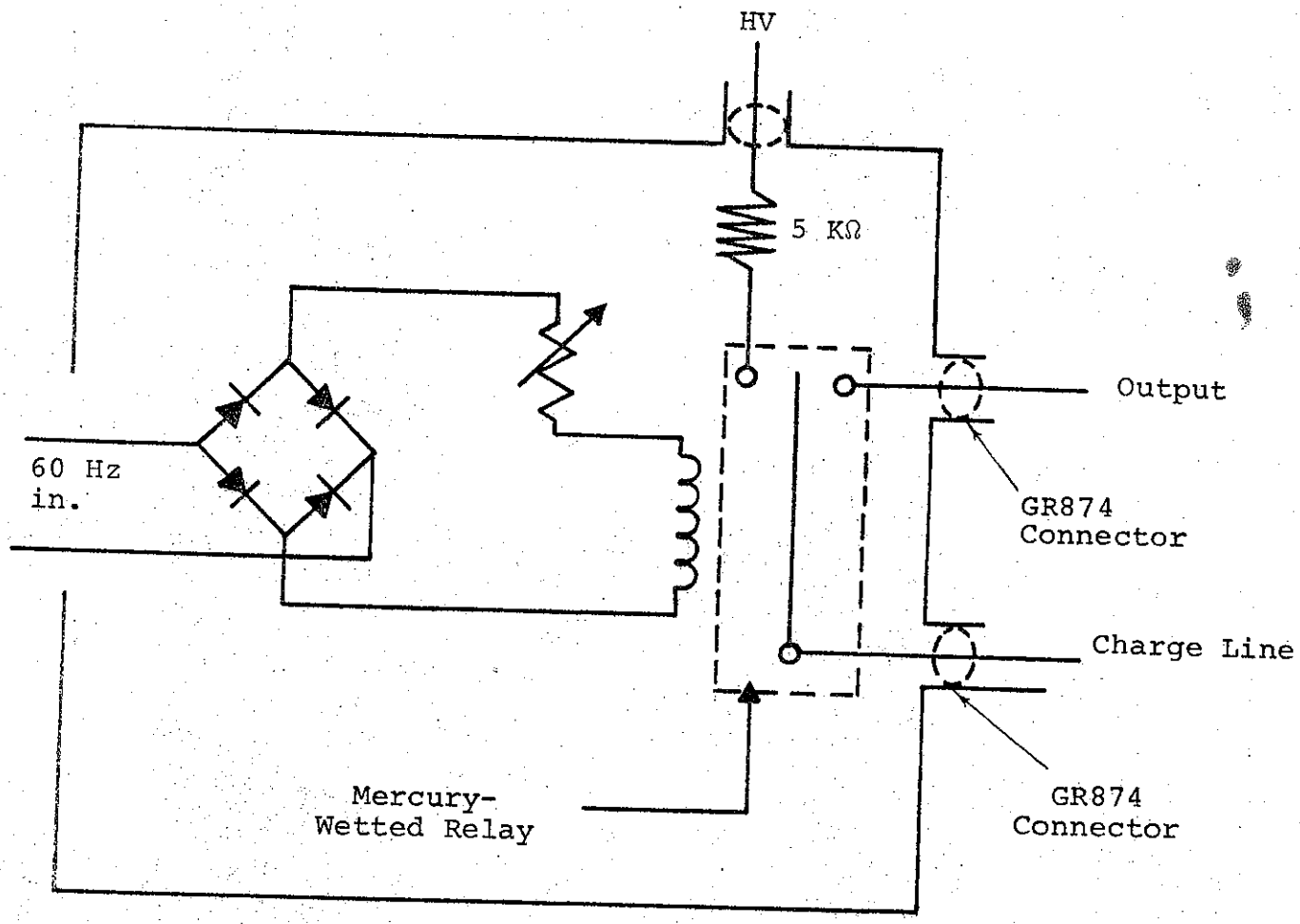

FIGURE 2. SCHEMATIC OF HIGH VOLTAGE PULSER USED TO FEED B-PROBE CALIBRATION APPARATUS

7501

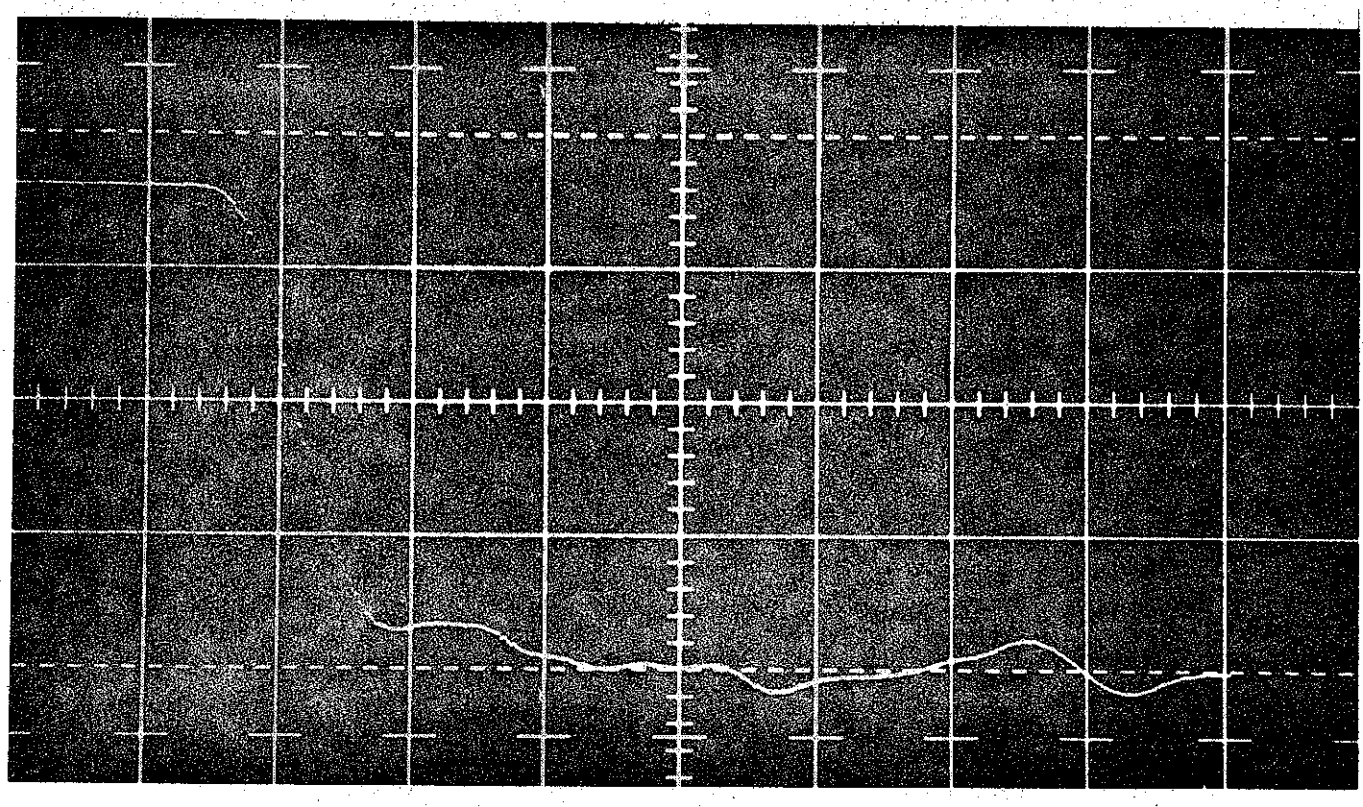

FIGURE 3. VOLTAGE AND CURRENT WAVEFORM ACROSS MODEL TERMINATION (Horizontal Scale 1 nsec/div, Vertical Scale Arbitrary)

With the model completed and the probe parameters decided upon, it was easy to begin testing and developing prototypes. A number of unsuccessful combinations and their characteristics are tabulated below:

Integrating Resistor	Characteristics
Carbon composition	Far too inductive; good power handling capacity
Stainless steel strip across loop	Far too inductive; used as a fast trigger on the 1140
Stainless steel strip laminated above ground plane, two-terminal resistor	Fair frequency response; monitoring across loop leads gave a fair amount of inductance; worked well at accelerator frequency

The last material worked adequately, except for the inductance associated with the connection to the loop. It was decided to develop a three-terminal device where the signal output carried only the current to drive the recording oscilloscope. Schematically, the device appears as shown below:

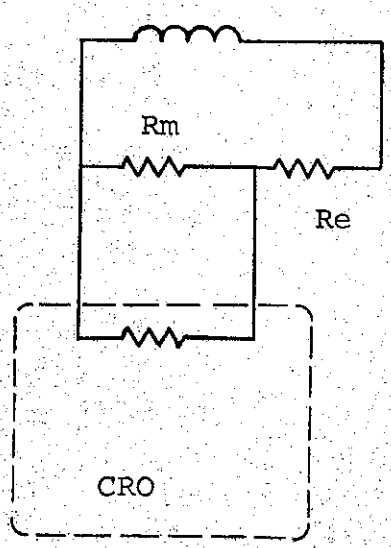

The resistor chosen is made of 0.00075-cm-thick 302 stainless steel alloy. The strip was soldered at one end to a copper tube and a sheet of thin copper was soldered over it. The tube was later soldered to the body of a hermetically sealed coaxial header.

A partially completed resistor assembly is shown in Figure 4. Two Mylar dielectric sheets, 1.25 mil thick (not shown), are inserted between the conductors, and the assembly is rolled tightly around the center post. Connection is made to the center conductor of the header, the pickup loop is connected, and the device is potted in epoxy.

Looking from above, the resistor appears as shown in Figure 5. The resistor dimensions are shown below:

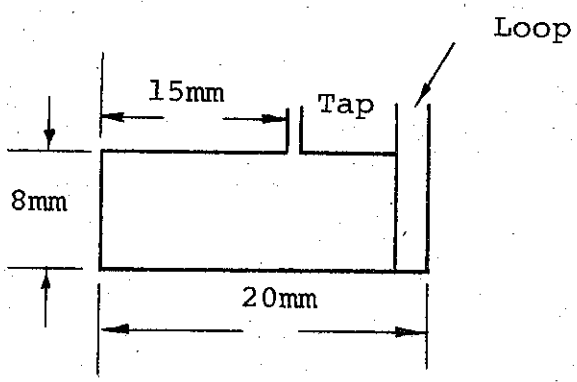

The calculated self inductance of this resistor, when laminated, is approximately 3×10^{-11} H.

The completed B-probe was mounted in the model and tested for transient response, electrostatic pickup, and decay constant, and the absolute calibration was measured.

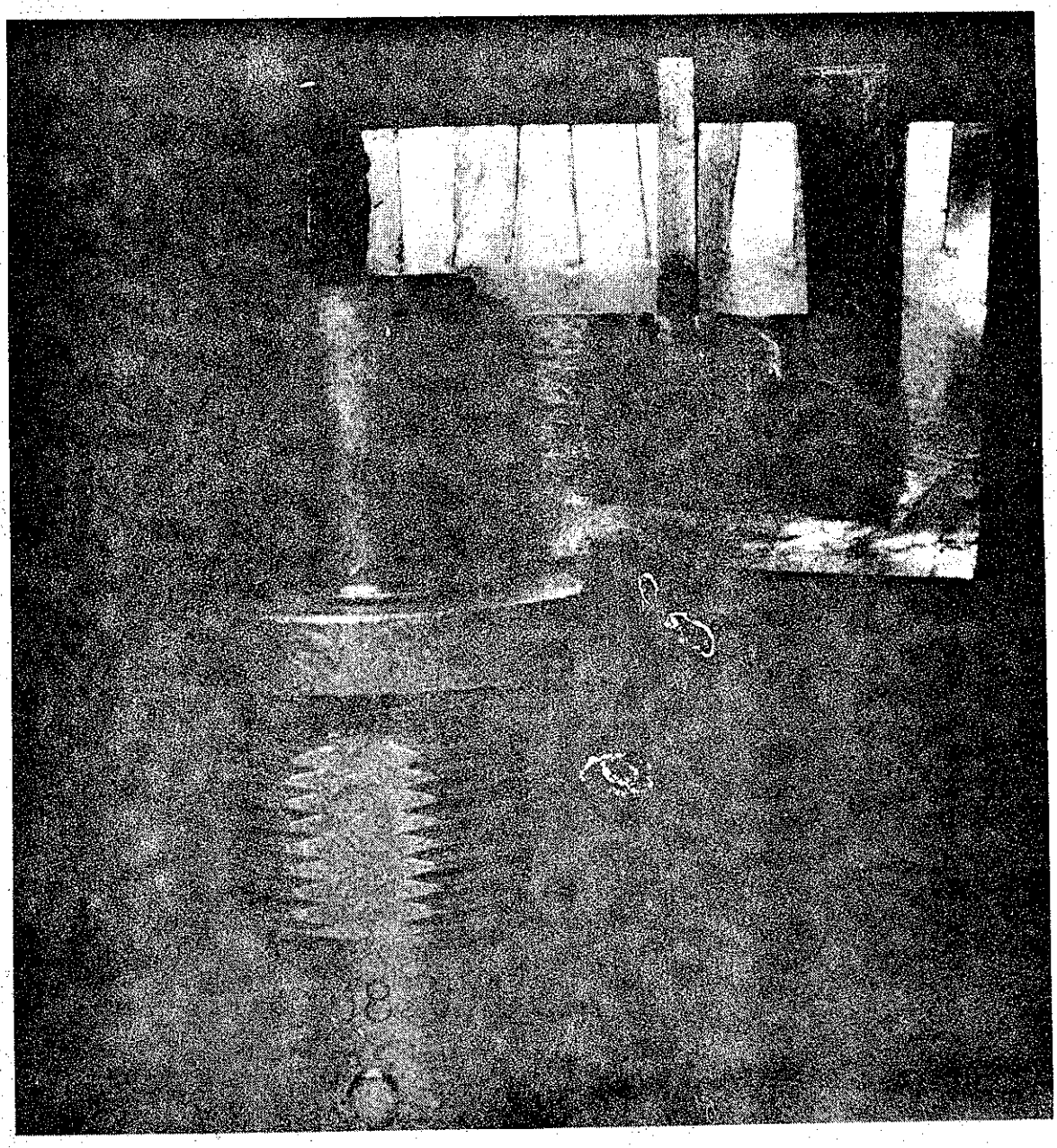

FIGURE 4. PARTIALLY COMPLETED RESISTOR ASSEMBLY

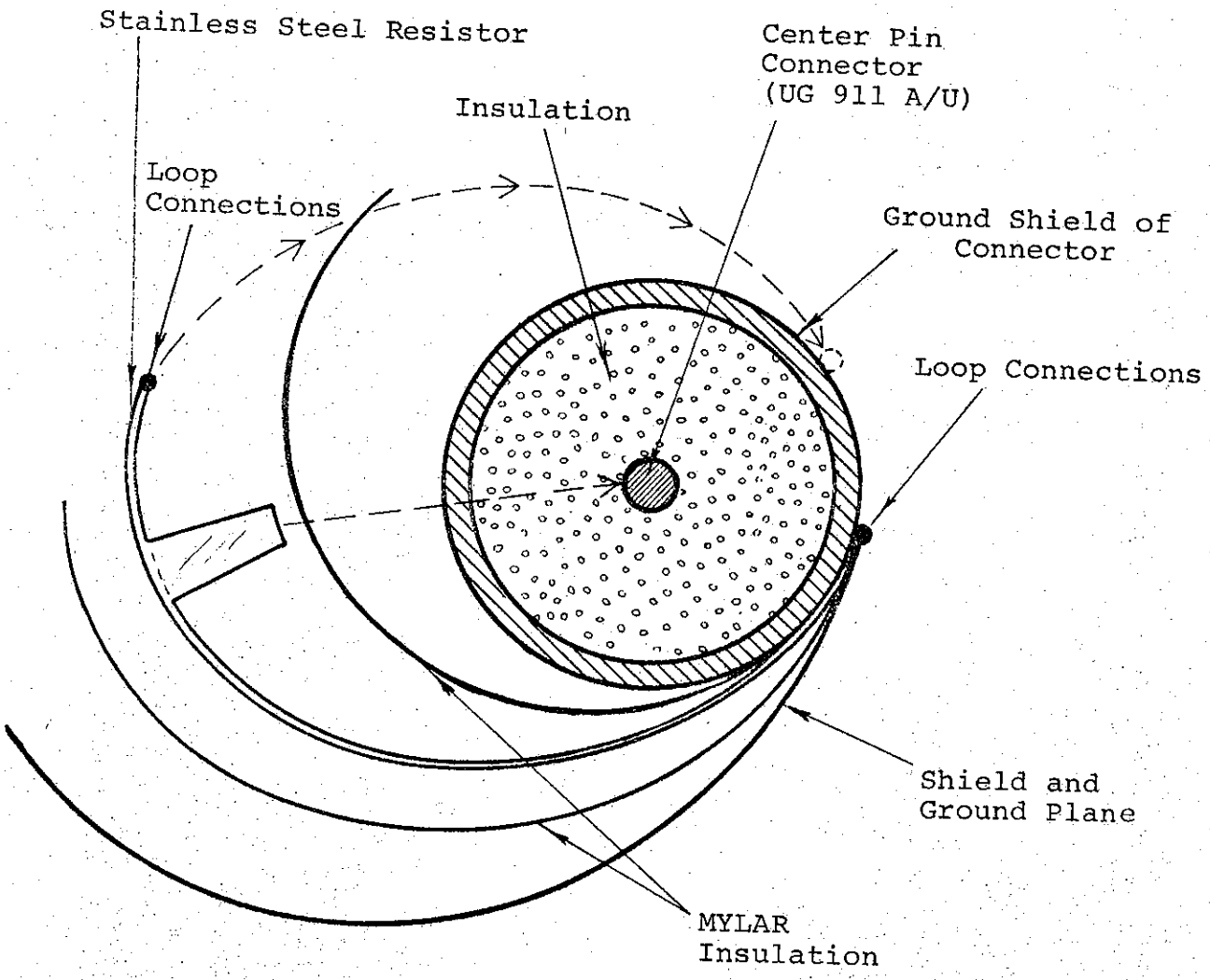

FIGURE 5. TOP VIEW OF RESISTOR

The transient response was measured by recording the output waveform of the probe and comparing it with the waveform on the termination. If the signal is induced magnetically, it should be possible to reverse the signal polarity by rotating the probe 180 deg so that the flux threads the probe in the reverse direction. This test was carried out routinely on all probes.

A check for electric-field pickup was made by orienting the probe axis parallel to the current vector in the coaxial line, so no magnetic flux would thread the loops and the output signal would indicate electrostatic pickup only. The response of one such probe (No. 3) to the driving function is shown in Figure 6, with the probe oriented in the three positions described.

All of the probe parameters can be inferred from the oscilloscope traces in Figure 6. The electrostatic signal is small, as shown by Figure 6c. Also, it is possible to infer the risetime of the device by assuming that its net risetime is given by

$$t_e = \sqrt{t_s^2 + t_o^2}$$

where t_o is the risetime of the probe, t_s is the driving function risetime, and t_e is the output risetime of the source and probe.

From Figure 3, the model e-folding risetime is 0.6 nsec, and the probe output pulse from Figure 6 is 0.8 nsec. Then

$$t_o = \sqrt{t_e^2 - t_s^2}$$

$$\approx 0.5 \text{ nsec}$$

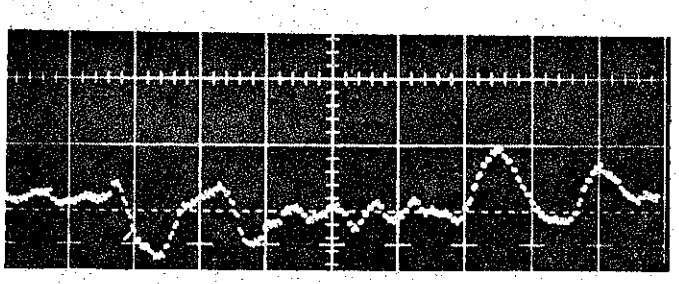

Probe 90 deg

(A)

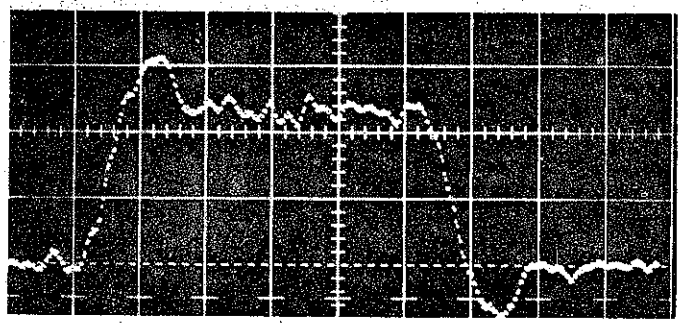

(B)

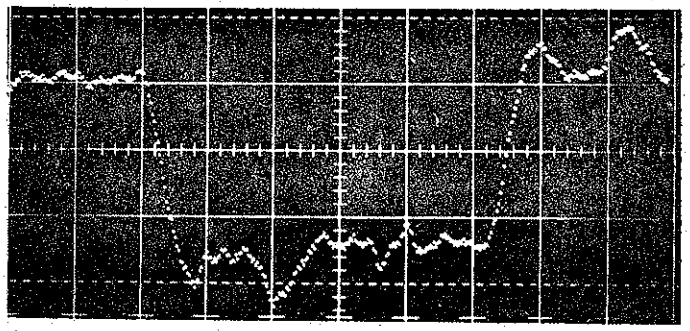

Probe 180 deg

(C)

FIGURE 6. B-PROBE NO. 3 RESPONSE TO DRIVING FUNCTION, 10-A DRIVING CURRENT, B = 1.67 X 10^5 W/m^2 (2 nsec/cm, 20 MV/cm)

The absolute calibration on the probe is also made on the model. For a coaxial system

$$B = \frac{\mu_o i}{2\pi r}$$

where i is the current in the center conductor and r is the radius from the center conductor to the center of the probe. Then

$$B = \frac{2i}{r} \times 10^{-7} \text{ W/m}^2$$

for the B-probe calibrations, i = 10 A, and $\bar{r}$ = 0.12 m; so for the calibration

$$B = 1.67 \times 10^{-5} \text{ W/m}^2$$

the output of probe No. 3 is 44 mV. Then the absolute probe calibration is

$$K = 3.8 \times 10^{-4} \text{ (W/m}^2\text{)/V}$$

d. Applications

The B-probes were applied initially as current monitors in the field-emission diodes of the Pulserad accelerators. Two checks were made on the operation of the probes. The first was to compare a series of shots where the cathode was shorted to the Faraday cup and both the Faraday cup and B-probe were monitored simultaneously.*

*The Faraday cup is discussed in the following subsection.

Figure 7 shows simultaneous waveforms from the Model 1140 Pulserad on a typical short-circuit shot. A similar set of oscilloscope traces is shown in Figure 8 for the Model 730 low-impedance Pulserad. Short-circuit shots were preferred for this correlation application because they ensured that all current passed into the cup and was measured.

In a second application of the B-probe, the net current in the electron-beam chamber was measured as a function of drift-chamber pressure. This is an important parameter relating to the behavior of the beam. For example, when a minimum net magnetic field is present, the beam electrons tend to follow the direction of initial injection into the chamber. At its maximum, the magnetic field tends to form a self pinch that concentrates virtually the entire beam in a few square centimeter.

A plot of peak current versus drift-chamber pressure is shown in Figure 9 for the Model 1140 Pulserad operating at 4 MeV. Similar measurements were taken in the drift tube of the Model 730 Pulserad operating approximately between 200 keV and 400 keV mean energy. A plot of peak net current versus pressure is shown in Figure 10.

The significance of these measurements will not be discussed, since the purpose of the data is to demonstrate the feasibility of using a fluxmeter for measuring net current in a beam-plasma system. Many other programs have made extensive use of this technique and have made extensive measurements of net currents induced by the beam-plasma interaction.

The fluxmeters have been used routinely to establish tube current in the accelerator tubes of the Model 730 and 1140 Pulserads.

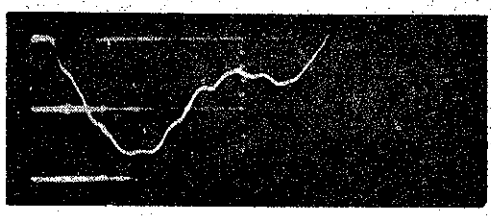

B-Probe

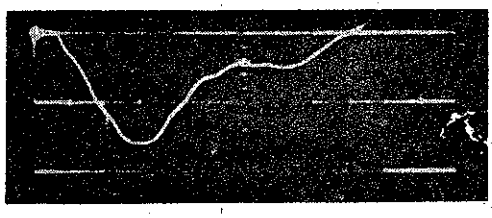

Faraday Cup

FIGURE 7. OSCILLOSCOPE TRACES COMPARING B-PROBE AND FARADAY CUP OUTPUTS ON THE MODEL 1140 PULSERAD, SHOT 2749

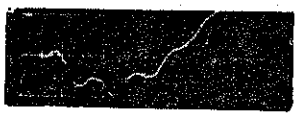

B-Probe

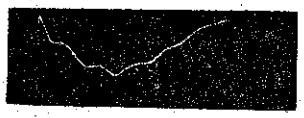

Faraday Cup

FIGURE 8. OSCILLOSCOPE TRACES COMPARING B-PROBE AND FARADAY CUP OUTPUTS ON THE MODEL 730 PULSERAD, SHOT 9135

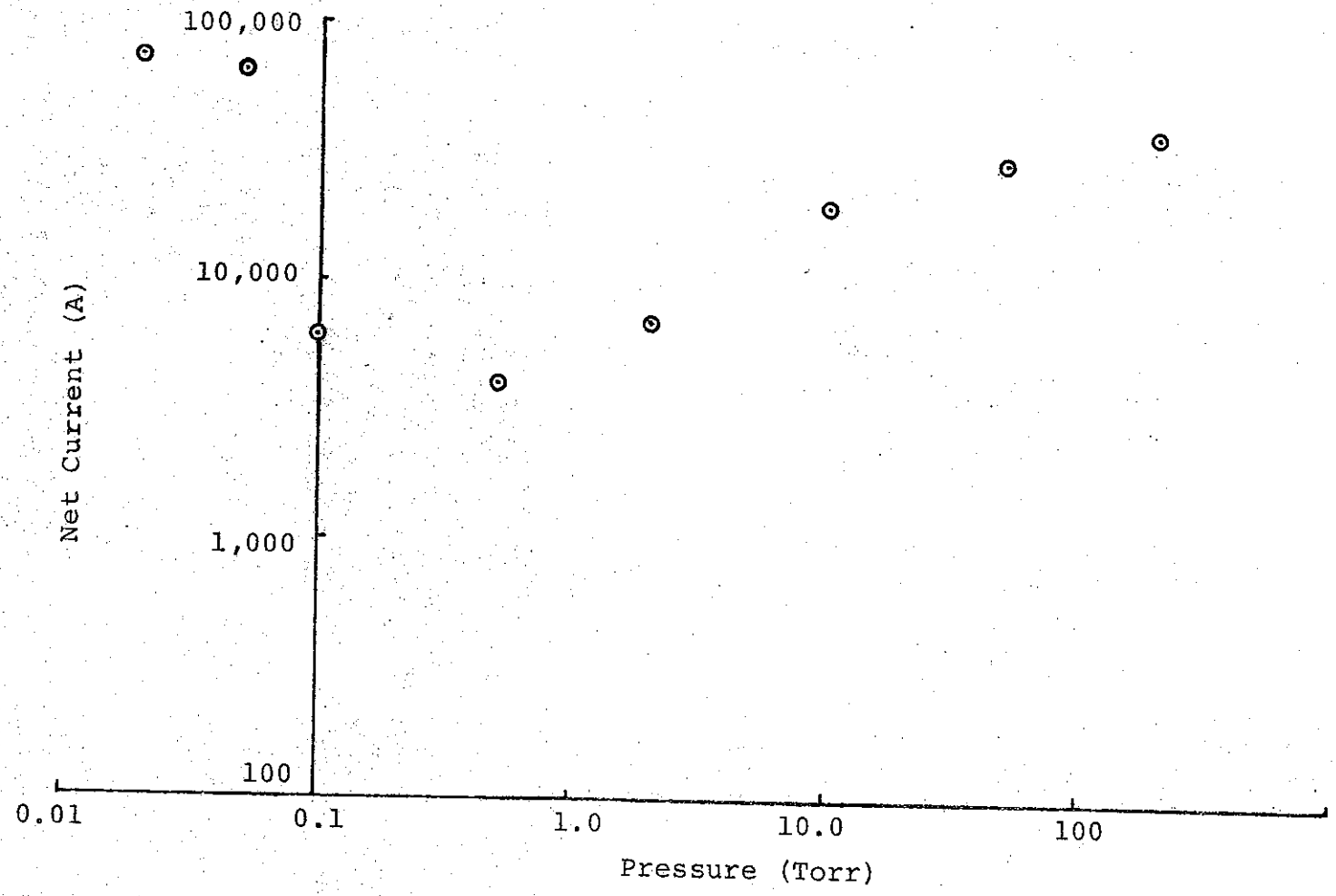

FIGURE 9. NET CURRENT VERSUS PRESSURE FOR 4-MeV 70,000 A MODEL 1140 PULSERAD ELECTRON BEAM

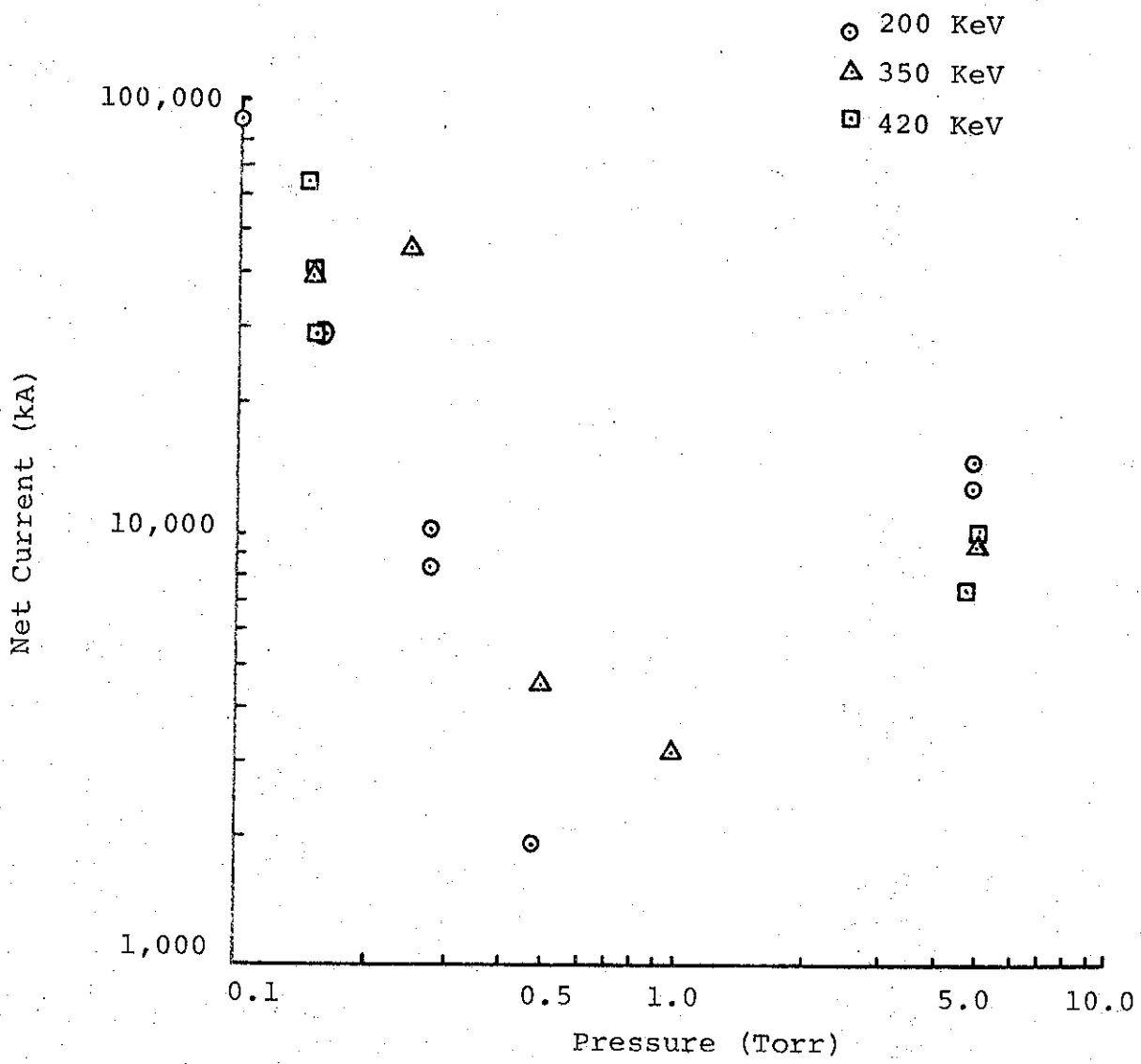

FIGURE 10. NET CURRENT VERSUS PRESSURE FOR SEVERAL LOW ENERGY MODEL 730 PULSERAD ELECTRON BEAMS

7499

They are also used as basic diagnostic devices for measuring net plasma currents in the drift chambers on basic electron-beam programs and have been supplied to measure the magnetic field near inertial-guidance components being tested on the SAMSO Model 1150 Pulserad.

2. Faraday Cup Development

a. Introduction

The Faraday cup (Figure 11) is a charge collector which intercepts a beam, then diverts it through an integral shunting resistor which in turn generates a voltage proportional to the current.

The collector, which acts as the inner conductor of the coaxial system, is a graphite cylinder, 8.7 cm long and 8.7 cm in diam. Graphite was chosen because it is low Z, which minimizes photon production, it is an inefficient generator of secondary electrons, and it is very resistant to spallation.

The resistor is a cylindrical tube of 302-alloy stainless steel foil, mounted coaxially with the collector. It is soft-soldered to a brass plate on one end and to a flange that provides the return path to ground. The flange bolts onto the front face of the accelerator. The 302 stainless steel alloy has a resistivity of 7.2×10^{-5} Ω-cm (Reference 1). For the high-current cup, the resistor was made of 0.0025-cm-thick foil. Connections make the device a 94-terminal network as shown schematically in Figure 11. The resistance of the cup the first time it was built was 5.6 mΩ; when it was rebuilt at various times, the resistance varied from 4.0 to 6.2 mΩ.

PIFR-095

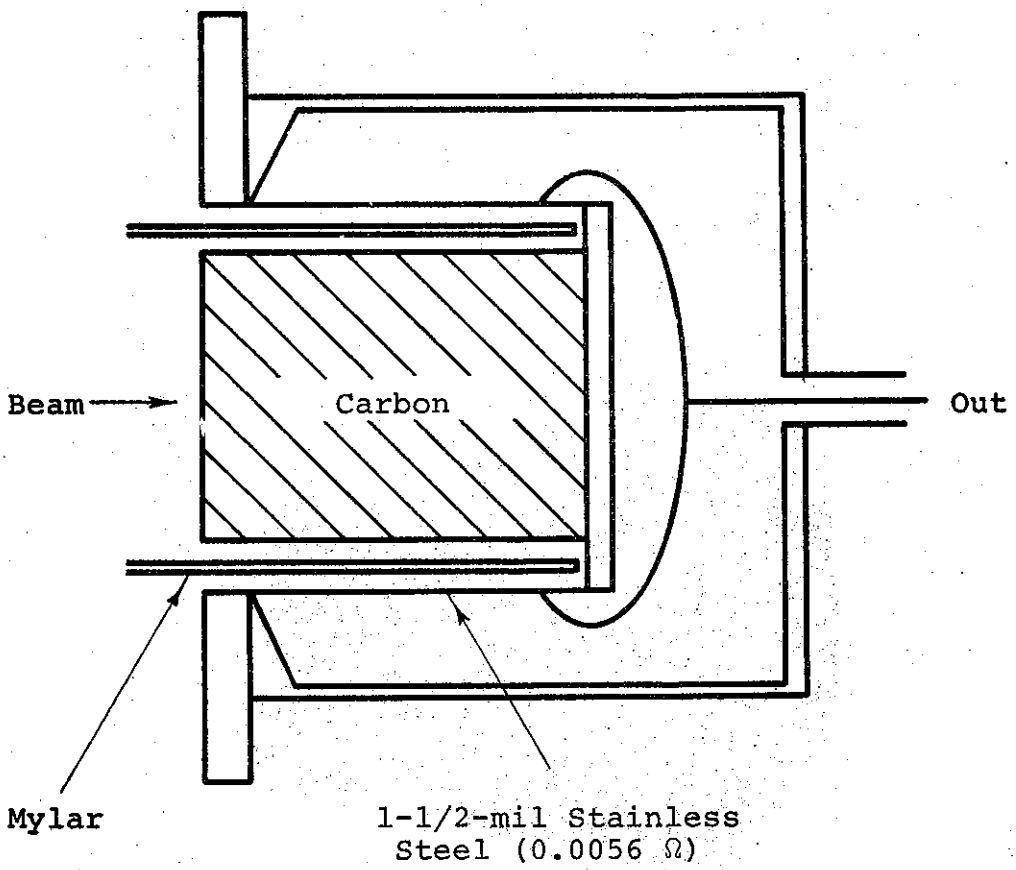

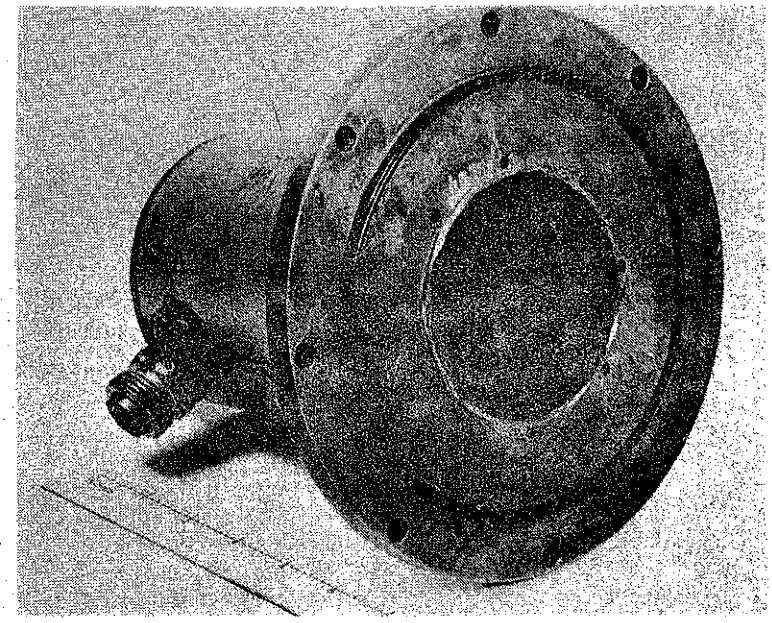

FIGURE 11. FARADAY CUP FOR MEASURING HIGH CURRENT, HIGH ENERGY ELECTRON BEAMS

b. Calibration

The device was dc calibrated first by connecting the device to a battery through a series resistor and measuring the input current while simultaneously measuring the voltage across the output terminals. Next, a calibration with a fast pulse was made using a Tektronix sampling plug-in to monitor the output waveform.

The output risetime of the cup, as measured by this technique, is less than 1 nsec. The pulsed-current measurements and the dc measurements agreed within the accuracy of the meters used.

c. Theory

In principle, the device is quite simple. A resistive voltage drop is measured along the outside of the stainless steel outer conductor. When a current is injected into the collector it will propagate toward the rear and induce an image current on the outer conductor. When the wave reaches the shorted back end in approximately 0.47 nsec, the voltage wave will reverse polarity and reflect back, largely cancelling the inductive voltage component.

This wave tends to damp rather rapidly because the graphite and stainless steel are quite resistive. Since the resistor is sealed electrically, the current must penetrate the outer conductor to provide a measurable voltage drop along the conductor. The fractional current penetrating the surface is

$$\frac{I}{I_o} = \exp\ (-x/\delta)$$

where δ is the skin depth. For the 1.06-GHz transient wave generated in the cup, the fractional current penetration will be

$$\frac{I}{I_o} \simeq \frac{1}{7}$$

The outer conductor thus filters out the transient waveform generated inside the cup.

d. Applications

Two applications of the Faraday cup have been made so far. In the first, it was used as a current monitor in the accelerator tube of the Pulserad accelerators; in the second, it measured the relativistic electron current at a given axial position in the drift chamber.

1. Tube Current Measurement

The Faraday cup was used most often as an absolute current monitor to determine waveforms and levels on the accelerators. On the high-impedance machines, shots were usually taken by shorting the cathode into the cup to ensure that all current passes into the cup.* On the low-impedance machines, calorimetry and material-damage studies revealed that because the beam was confined to an area far smaller than the cup collector, it could be accelerated directly into the cup. Typical short-circuit shots have been shown in Figures 7 and 8 in the section on the B-probe. Several interesting shots resulted when the Model 730 beam was accelerated at the cup (Figure 12). The cathode was shorted to the cup collector, but the shock of the machine switching broke the back connection on the resistor and pushed the collector 1 to 2 mm away from the cathode. The beam energy corresponded to approximately 150 kV. Evidently the circuit was completed by the joint arcing. Because of the four-terminal construction, the only change was a slight drop in peak levels on both the B-probe and Faraday cup. The cup was still reading diode current accurately (see Figure 13 for comparison).

*Shots have since been made using the Faraday cup as the anode on the Model 1140 Pulserad. Currents of $\approx$ 60 kA at 4-MeV mean energy were measured.

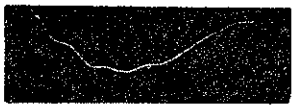

Shot # 9141

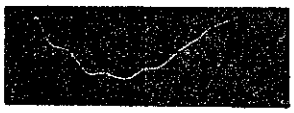

Shot # 9143

FIGURE 12. FARADAY CUP OUTPUT WAVEFORMS ON MODEL 730 PULSERAD, BACK OF CUP DISCONNECTED

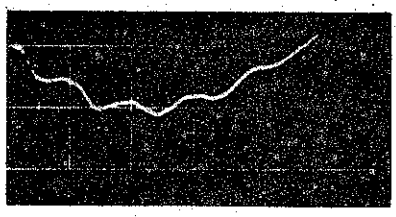

B-Probe

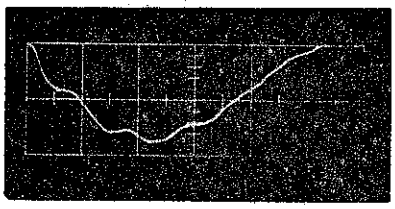

Faraday Cup

FIGURE 13. NORMAL FARADAY CUP FOR SHORT CIRCUIT CONDITION ON MODEL 730 PULSERAD (Current, 0.28 MA)

Under short-circuit conditions, peak currents have been measured up to 0.28 MA with no electrical or mechanical malfunction of the cup.

2. Measurement of Beam Current After Traversing a Field-Free-Region

In a second application, the cup was tested for measuring relativistic beam current after the beam had traversed a relatively field-free-region where the primary beam-space charge and self-induced magnetic fields were neutralized by a plasma. A conductive diaphragm in front of the cup face acts as a vacuum seal and prevents low-energy secondary electrons and ions from entering the collector. The cup was evacuated to a pressure below 10^{-3} Torr to minimize the possibility of ion formation, which would partially neutralize the relativistic beam current. The experiment was tried successfully on the Model 1140 Pulserad with the experimental setup shown in Figure 14.

A typical set of waveforms showing diode current, diode voltage, and relativistic current at the end of the drift chamber are shown in Figure 15. The cup waveform mirrored the diode current waveform; the peak current measured in the cup was approximately 60% of the peak diode-current. Figure 16 is consistent with calorimetric data for a target the size of the Faraday-cup collector.

A similar attempt was made, using the Faraday cup, to measure the relativistic current in the 200-keV, 200-kA beam on the Model 730 Pulserad. Although the original design of the cup proved faulty, probably as a result of space-charge-induced fields in the vacuum region, it provided the insight for a successful design on a later contract. In these devices, it is important to consider the effect of space-charge-induced potentials in the evacuated region in front of the collector.

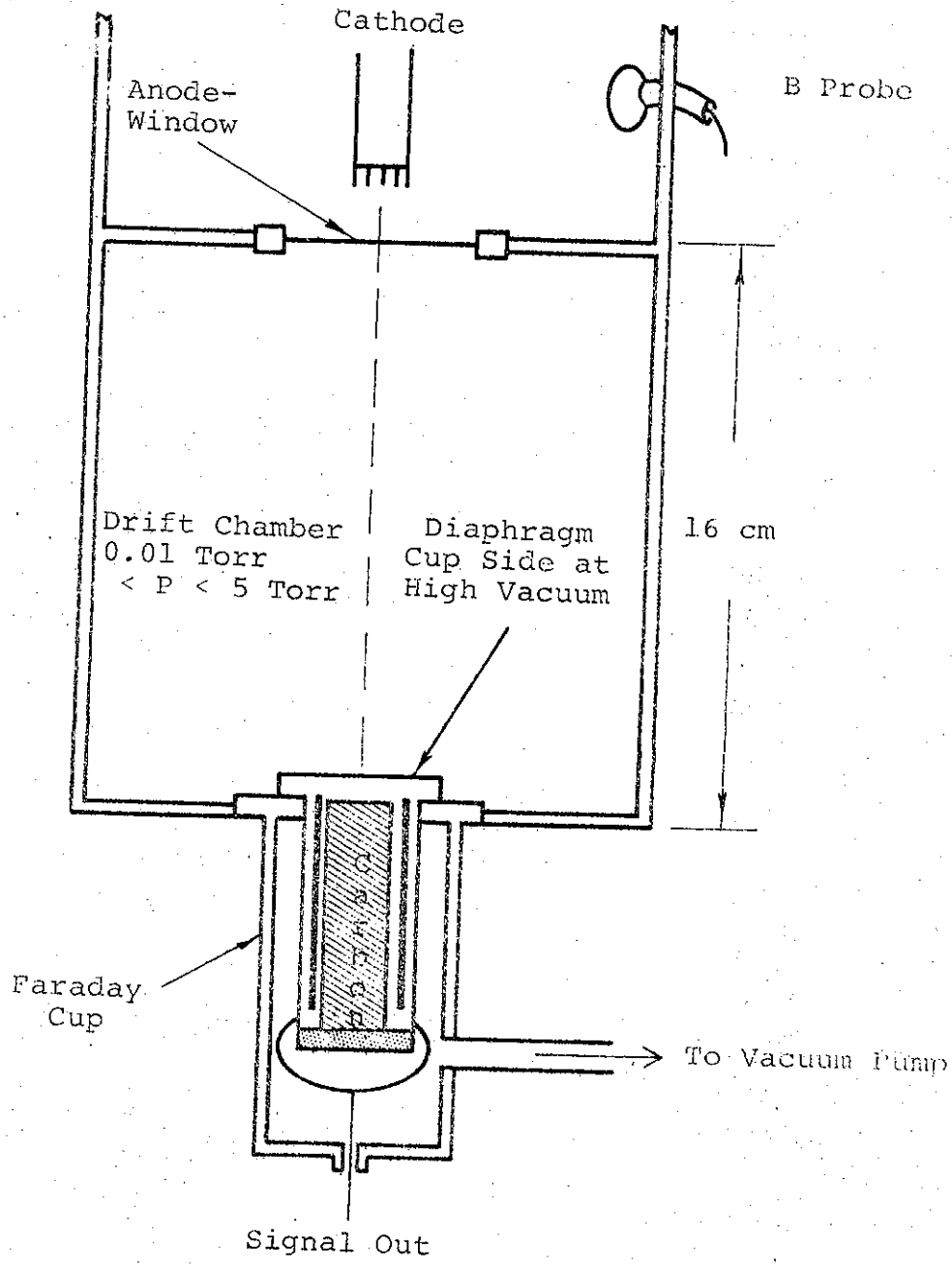

FIGURE 14. EXPERIMENTAL SET-UP FOR MEASURING ELECTRON CURRENT IN DRIFT CHAMBER WITH FARADAY CUP

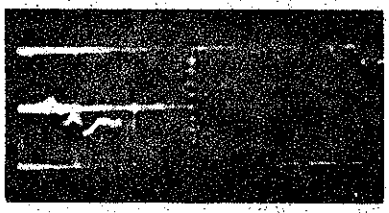

Diode Current

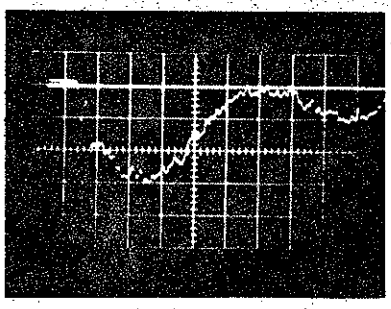

Diode Voltage

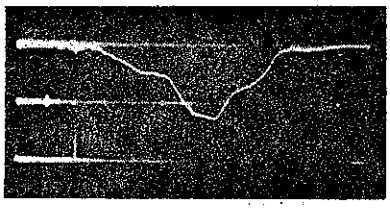

Faraday Cup Output

FIGURE 15. TYPICAL SET OF WAVEFORM FOR DIODE CURRENT, DIODE VOLTAGE, AND PRIMARY BEAM CURRENT AT END OF DRIFT CHAMBER (Z = 48 cm) FOR MODEL 1140 PULSERAD 4-MeV BEAM (20 nsec/cm)

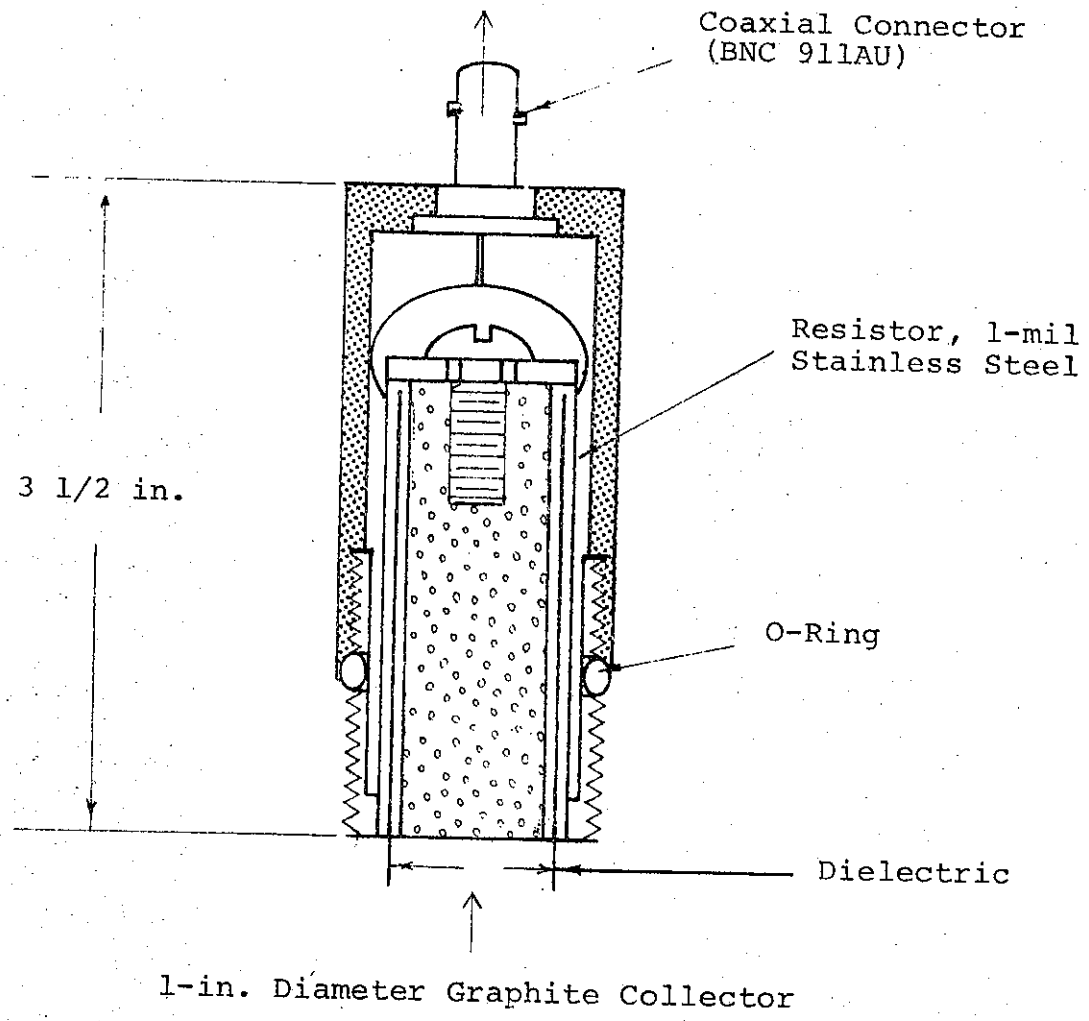

FIGURE 16. CROSS SECTION OF SMALL FARADAY CUP

3. Array of 2.5-cm Faraday Cups

After initial testing had established the design techniques for the large Faraday cup, small Faraday cups were built to measure the current density in the drift chamber as functions of time and space.

A baseplate, which acted as a return path and provided the vacuum seal for the cups, was made with mounting holes for a crossed array of seven horizontal and five vertical cups. The cups were mounted on 3.7-cm centers. The collectors were cylindrical and had diameters of 2.5 cm. Because of this smaller area, the nominal cup resistance was increased to 20 mΩ. The Faraday cups were identical to the larger cup, not only in principle, but also in performance. They were used to intercept the bulk of a drifting beam (Figures 14 and 15). The cups and a cross-sectional view showing their construction are pictured in Figures 16 and 17, while Figure 18 depicts a calibration pulse on the small cups, using the same circuit technique as with the large Faraday cup. The assembled array is shown in Figure 19. Since the cup array was used initially to explain anomalies in the magnetic-spectrometer output, the experiments on the cup will be described in Section III,A,5.

4. High-Voltage Capacitative Probe Development

a. Introduction

The high-voltage detection system is composed essentially of a pair of plates located near the outside wall of the field-emission diode that divides the voltage capacitively. A coaxial cable is connected to the plates. The plates are actually two laminated sheets of aluminum with a 5-mil thick sheet of Mylar between them. A completed voltage monitor and schematic are shown in Figure 20.

b. Theory

The electrostatic field generated by a charge distribution is generally calculable. For coaxial cylinders, the potential is

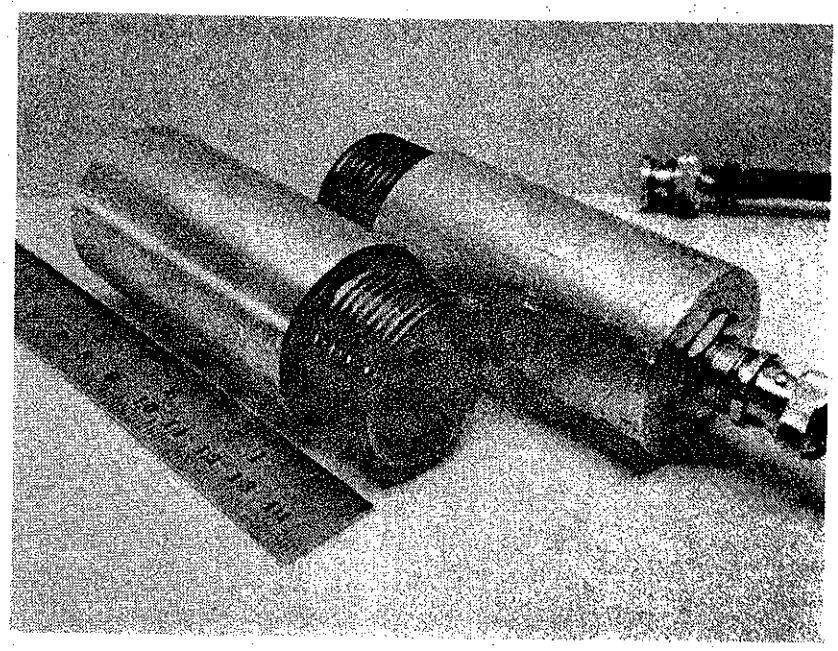

FIGURE 17. SMALL FARADAY CUPS

Upper Cup Output:

2 nsec/cm
50 V/cm

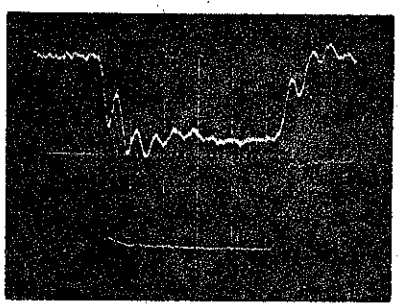

Lower Output Pulse:

2 nsec/cm
2.5 A/cm

FIGURE 18. CALIBRATION TRACE FOR SMALL FARADAY CUPS (Current in = 7 A)

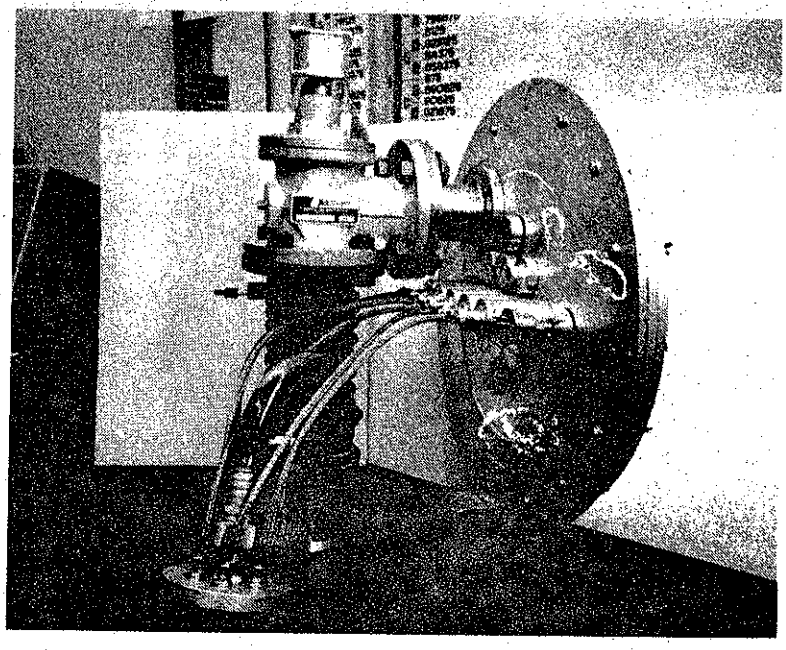

FIGURE 19. ASSEMBLED ARRAY OF SMALL FARADAY CUPS

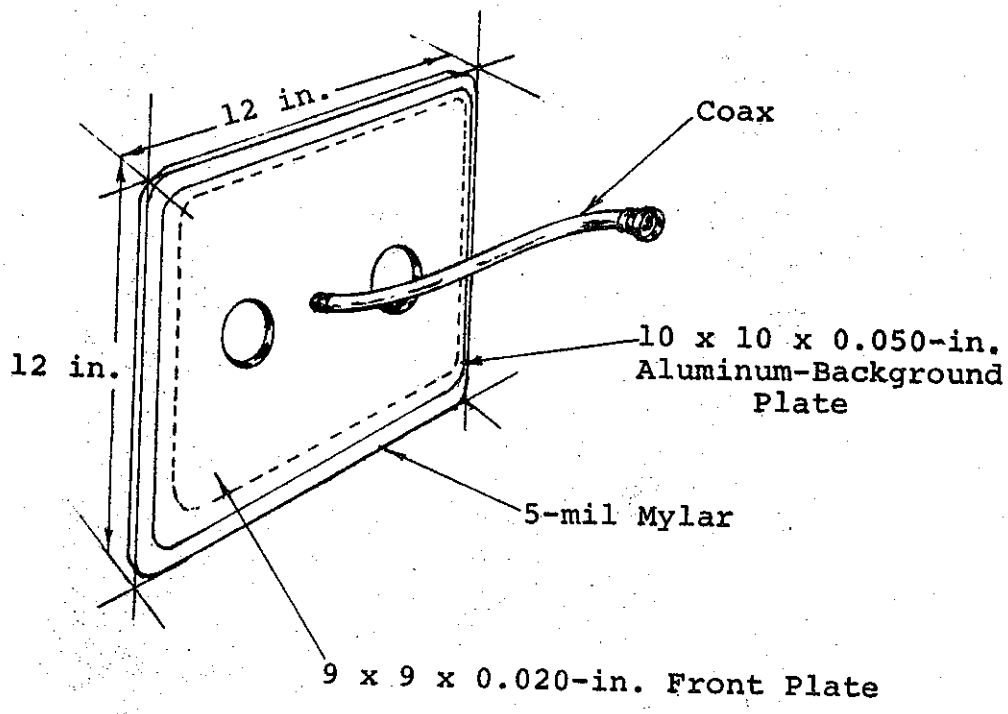

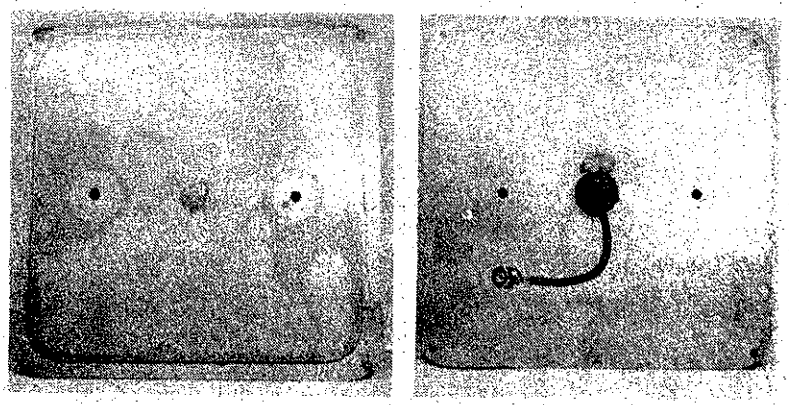

FIGURE 20. HIGH-VOLTAGE CAPACITANCE PROBE

given as

$$V(r) = V_a \frac{\ell n(r/b)}{\ell n(a/b)}$$

where V_a is the potential on the center conductor of radius a, and b is the radius of the outer conductor (assumed to be at ground potential). With a conducting plate in the space, and an arbitrary potential, $V_a(t)$, applied to the inner cylinder, the potential of the space at (b-d) is given as

$$V_d(t) = V_a(t) \frac{\ell n\,[(b-d)/b]}{\ell n(a/b)}$$

where d is the distance between the floating plate of the capacitance probe and the outer ground cylinder. If $d << b$, then

$$V_d(t) = V_a(t) \frac{d/b}{\ell n(a/b)}$$

The potential difference between plates at d and b can be derived from the equation for the equivalent circuit

$$V = V_d(t) - \frac{q}{C}$$

where $V_d(t)$ is the time-dependent potential of the space at d, q is the charge on the plate at d, and C is the capacity of the plate to the outer conductor. However,

$$q = \int_t i\,dt$$

and if the current, i, flows through an ideal resistor:

$$q = \int_t i\,dt = \int_t \frac{V}{R}\,dt$$

then

$$V = V_d(t) - \frac{\int_t V\,dt}{RC}$$

If the period over which V is integrated is much less than RC, then

$$V \approx V_d(t)$$

Then the potential across the plate that we measure is given by

$$V = k_1 V_a(t)$$

If there is a dielectric with a dielectric constant, k, between the plate and the outer conductor,

$$V = \frac{k_1}{k} V_a(t)$$

It should be noted that k_1 is entirely a geometric constant, and for our coaxial geometry

$$k_1 = \frac{\ell n \left[(b-d)/b \right]}{\ell n (a/b)}$$

c. Design Criteria

Choosing and building a voltage monitor for the high-voltage Pulserads requires a combination of tradeoffs. The capacitive device has a number of disadvantages. One is that it does not monitor the potential directly, but is merely a device for measuring electric field, and as such is influenced by changes in geometry. Another disadvantage is its extreme sensitivity to charge pickup from electrons or ions drifting across the space. Apparently very little charge reaches the capacitor during the main beam pulse in the Pulserads. On the other hand, the capacitive device has some advantages too. Since it can be mounted very near the anode, it measures cathode potential well. Besides being relatively

inexpensive and simple to build and install, it avoids the voltage breakdown problems associated with voltage probes in which the full pulser voltage is applied to the device.

d. Calibration

When fields are assumed to have cylindrical symmetry, voltage across the capacitor is given by

$$V = \frac{(d/bk)\ V_a(t)}{\ell n(a/b)}$$

For the small spacings involved (0.125 mm) the spacing cannot be maintained accurately, nor can the dielectric be homogeneous. This was negated by noting that the capacity, C, is given by

$$C = \frac{\varepsilon_o kA}{d}$$

where A is the area of the probe; calibration of the device is given by

$$V = \frac{V_a(t)\ \varepsilon_o\ A}{(\ell n(a/b))b \cdot C}$$

The capacitance of the probe was measured directly with an impedance bridge.

The voltage monitors were assembled by bonding aluminum sheets to a Mylar dielectric. The early probes were plagued by delamination and damage from mishandling. When a mechanically reliable device was finally developed, little time remained in the program

to do any extensive testing. Early data dealt primarily with units that were dimensionally unstable or delaminated. Although the absolute calibration on these units is uncertain at present, measurements are being performed to obtain such data.

The voltage waveform generally agreed with data from the magnetic electron spectrometer. Two shots where voltage and current traces were taken are shown in Figure 21.

5. Electron Beam Analysis with Magnetic Spectrometer

a. Introduction

A magnetic spectrum analyzer (MSA) was constructed to make spectral measurements of the time-dependent energy spectrum of the high-current relativistic electron beam produced by a pulsed field-emission diode source. The development and calibration of this instrument is described in detail in Appendix A.

The objectives of these experiments were to (1) develop a technique for measuring the energy spectrum of the electron beam directly, (2) develop, in conjunction with the MSA measurements, a technique for determining the deposition profile of the electron beam that does not directly influence beam behavior, and (3) examine beam behavior for a number of different anode-cathode configurations.

b. Experimental Arrangement

During the tests on the Model 1140 Pulserad, the MSA was mounted on the machine axis outside the drift chamber, and was isolated from the drift chamber by a 0.003-in. Mylar window. The distance between the anode and the Mylar window was roughly 65 cm.

a. Shot 3437, 200-needle Shielded Cathode, 20 nsec/cm, Arbitrary Voltage

b. Shot 2195, B_4C Cathode, 20 nsec/cm, Arbitrary Voltage

FIGURE 21. TYPICAL RESPONSE OF CAPACITIVE VOLTAGE MONITOR

Diagnostics used in conjunction with the MSA were:

1. Optical photograph in drift chamber
2. Current measurements in anode-cathode region
3. Voltage measurements in anode-cathode region
4. Depth-dose measurements in drift chamber

For the following reasons, not all of these measurements were made on every shot: (1) a shortage of suitable oscilloscopes, (2) a shortage of current and voltage probes (they were damaged occasionally, and were difficult to replace), and (3) a shortage of clear windows for optical photography.

The spectrometer is designed to accept only a small portion of the beam. After passing through a magnetically shielded collimator, the beam enters an inhomogeneous B-field, which acts like a prism to separate the different energy components of the beam. The detection system is an array of 10 carbon blocks. The magnetic-field gradient and the injection angle are such that the focal points are located outside the magnet pole tips, the focal plane is flat, and the energy spread along the focal plane is linear, that is, if channel 10 corresponds to 5 MeV, and channel 1 to 0.5 MeV for one value of the field, when the field is increased so that channel 10 corresponds to 10 MeV, channel 1 will correspond to 1 MeV.

The signal received by the detectors can be displayed on an oscilloscope and can be integrated simultaneously. A Tektronix 519 oscilloscope is generally used to monitor the time-resolved signal, and a Vidar Integrating Digital Voltmeter is used to measure the voltage on the integrating capacitors.

On a normal shot, the current entering the spectrometer is typically 1 to 10 amperes. Generally, the mode of operation was such that 1.0-MeV electrons were seen by channel 2, 2.0-MeV electrons were seen by channel 4, and so on. The actual parameters for this configuration are B_{max} = 900 G, and I_m = 6.3 amperes. According to the geometry of the system, each channel had a width of approximately 0.25 MeV, increasing slightly in the higher-numbered channels.

The initial experiments were performed with a six-channel MSA. The bulk of the tests, however, were made with a 10-channel MSA.

Several different anode-cathode configurations were tested. Cathodes used were: (1) a boron-carbide (B_4C) rod, 2 cm in diam, extending 10 cm beyond the "doughnut" cathode holder; (2) two concentric circles of 18 needles each; and (3) three concentric circles of 36 needles each. For the most part, the anode used was a 10-in. by 0.002-in. titanium foil. On a few shots, a 6-in. by 0.002-in. titanium foil was used in conjunction with a solenoid magnet (Reference 2).

A special 20-mil aluminum depth dose, with a hole through the center, was used on several shots with the B_4C cathode. The portion of the beam passing through the hole in the depth dose entered the MSA. A diffuser consisting of a 50-mil aluminum foil was used on several shots, primarily with tests on the needle cathodes. Table I lists the number of shots taken for each of the geometries tested.

c. Time-Resolved Output Results

To understand the results of the time-resolved MSA output, consider Figure 22. A typical voltage-pulse waveform, monitored

TABLE I

NUMBER OF PULSER SHOTS FOR EACH GEOMETRY TESTED

Experimental Conditions		Number of Shots: 72	32	4	16	8	2	2	3	2	4	4	1	1
Cathodes	B_4C	✓	✓	✓										
	Needles: 18-18				✓	✓	✓	✓	✓	✓				
	Needles: 36-36-36										✓	✓	✓	✓
Anodes	10 in.	✓	✓	✓	✓	✓	✓	✓			✓	✓	✓	✓
	6 in.								✓	✓				
Switch Gaps	4.5 in.	✓	✓	✓	✓	✓			✓	✓	✓	✓		
	5.0 in.						✓	✓					✓	
	5.5 in.													✓
Depth Dose			✓											
Diffuser				✓		✓						✓	✓	✓
Magnetic Injection									✓					

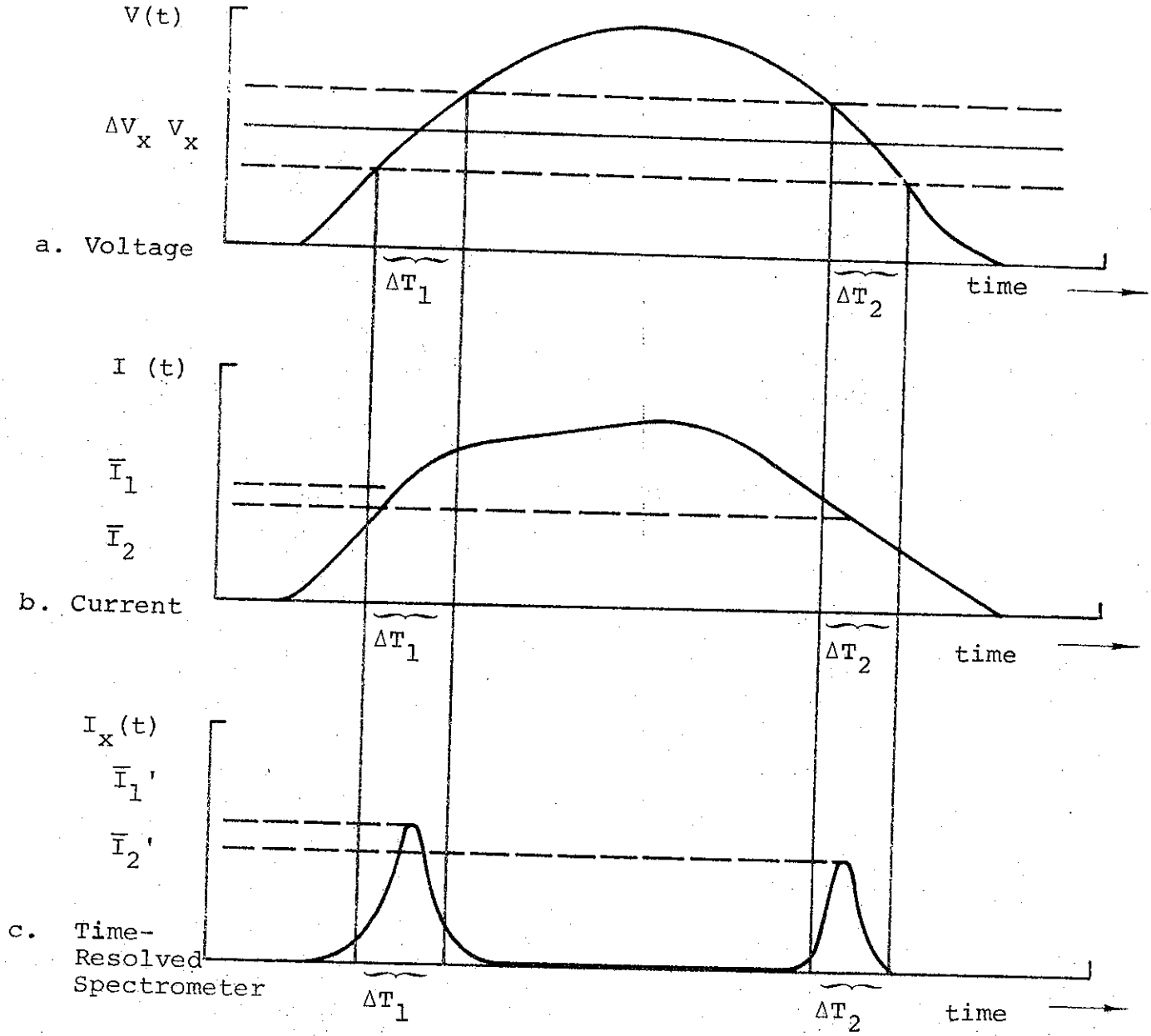

FIGURE 22. TYPICAL WAVEFORMS: a. VOLTAGE, b. CURRENT, AND c. TIME-RESOLVED SPECTROMETER

in the anode-cathode region, is shown in Figure 22a, and a typical current-pulse waveform, also from the anode-cathode region, appears in Figure 22b. Figure 22c shows the time-resolved output of channel x. V_x is the energy seen by channel x, and ΔV_x is the channel width. ΔT_1 and ΔT_2 are the time intervals during which those electrons that can be seen by channel x are being generated. During each of these intervals the average current is I_1 and I_2, respectively. The current seen by channel x is proportional to the area of the beam accepted by the circular collimating window, and depends on the beam cross-section profile. Because the current is increasing during the first pulse seen by channel x and is decreasing during the second pulse, the waveforms of these pulses are skewed toward the center. An example of the results obtained from a typical shot exhibiting this classical response appears in Figure 23.

Departures from the classical response occurred quite frequently. One of the more common results was an asymmetry in the pulses wherein one pulse was considerably smaller than the other, or occasionally, nonexistent. Figure 24 shows the results of a typical shot exhibiting this type of behavior, and is possibly explained by beam wandering. The results obtained from experiments performed with a Faraday-cup array support this hypothesis.

A Faraday cup consists essentially of a graphite block that intercepts a portion of the beam, and a known resistor from the block to ground. By monitoring the voltage across the resistor, one has a direct measurement of the time history of the current (the detectors in the MSA are essentially Faraday cups). The difficulty in measuring large currents is in obtaining accurately calibrated small resistors, and in designing the apparatus with as low an inductance as possible. Since Section III,A,3, has already dealt with the development of this device, we shall not report on the details of its construction and calibration here.

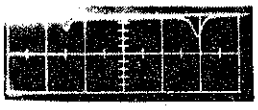

Channel 2

Channel 3

Channel 4

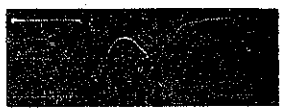

Channel 5

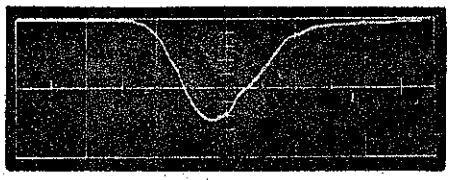

Channel 6

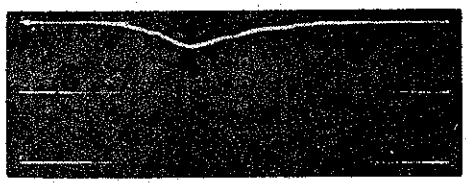

Channel 7

FIGURE 23. CLASSICAL TIME-RESOLVED OUTPUT FROM MSA, SHOT 3131 (Sweep Speed, 20 nsec/cm Vertical Sensitivity, ≈ 20 V/cm)

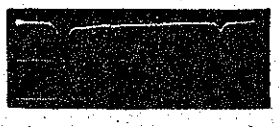

Channel 2
≈ 20 V/cm

Channel 4
≈ 20 V/cm

Channel 5
≈ 50 V/cm

Channel 6
≈ 50 V/cm

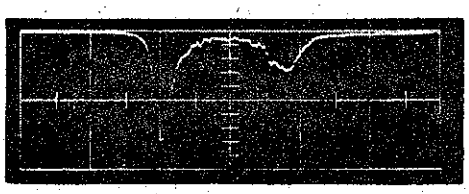

Channel 7
≈ 50 V/cm

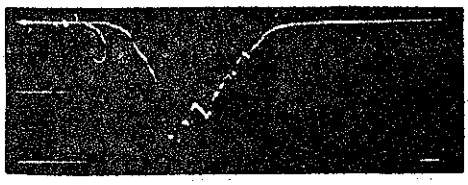

Channel 8
≈ 40 V/cm

Sweep Speed: 20 nsec/cm

FIGURE 24. MSA DATA--TYPICAL SHOT EXHIBITING AN ASYMMETRY IN PULSE HEIGHT, SHOT 3120 (Sweep Speed, 20 nsec/cm)

Figure 25 indicates the orientation of the Faraday cups.

If the beam has a uniform cross section for the duration of the pulse, then all five Faraday cups should have the same qualitative output, perhaps with No. 1 having a larger signal due to a gaussian-type spread in current density. Figure 26 shows the results obtained with a needle cathode and a 50-mil aluminum diffuser. All channels exhibit the same behavior, which is typical of those tests using a diffuser. Figures 27 and 28 show results obtained with the same needle cathode, but without the diffuser. The marked differences between the signals seen by the five channels, provides strong evidence of a variation of the beam cross-section profile with time.

Returning to the MSA results, another departure from the classical response is the appearance of extraneous pulses, extra pulses, or fine structures superimposed on otherwise normal pulses, as shown in Figure 29. The data are insufficient to explain such behavior satisfactorily.

On the basis of beam stability in the drifting mode, a comparison can be made of the relative merits of the three anode-cathode configurations tested. Deciding whether a given shot is successful or not is quite arbitrary. Generally, a shot is classified as a success if it exhibits the classical behavior with asymmetries in pulse height and small extraneous pulses, or both; a shot is unsuccessful if there is no real evidence of the classical behavior, or if there are gross extraneous pulses. Using these criteria, an analysis of the shots taken with the MSA is shown in Table II. Neglecting the series of shots with the 18, 18 needle cathode and 6-in. anode, we see that 53% of the shots on the B_4C cathode, 88%

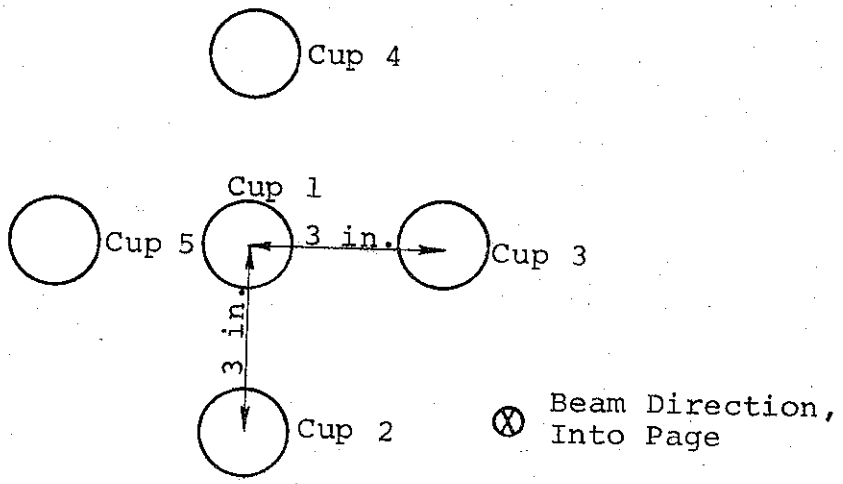

FIGURE 25. SCHEMATIC OF FARADAY CUP ARRAY

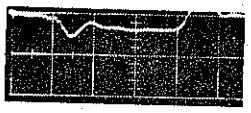

Cup No. 2

Cup No. 1

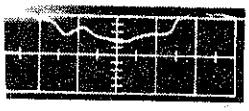

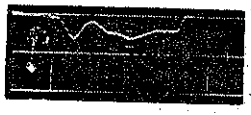

Cup No. 4

Cup No. 3

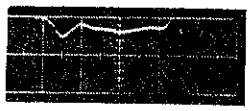

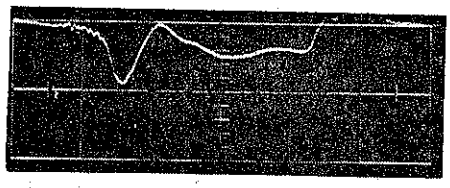

Cup No. 5

Sweep Speed: 20 nsec/cm
Vertical Sensitivity: ∿10 V/cm

FIGURE 26. OUTPUT FROM FARADAY CUP ARRAY INDICATING UNIFORM BEAM CROSS SECTION, SHOT 3096 (Sweep Speed, 20 nsec/cm and Vertical Sensitivity, 10 V/cm)

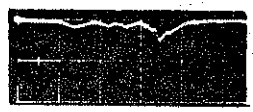

Cup 2

Cup 1

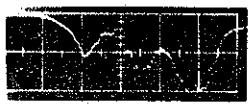

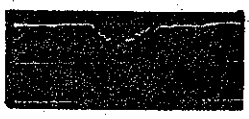

Cup 4

Cup 3

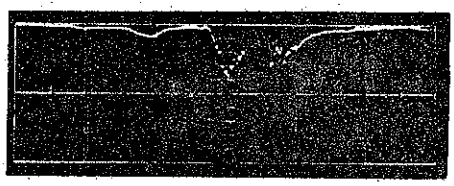

Cup 5

Sweep Speed: 20 nsec/cm
Vertical Sensitivity: ~10 V/cm

FIGURE 27. OUTPUT FROM FARADAY CUP ARRAY INDICATING NONUNIFORM BEAM CROSS SECTION (SHOT 3099)

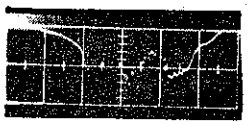

Cup 1

Cup 2

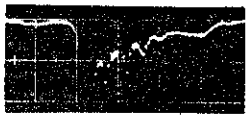

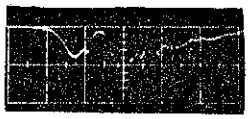

Cup 3

Cup 4

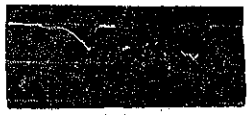

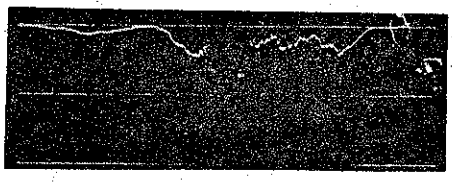

Cup 5

Sweep Speed: 20 nsec/cm
Vertical Sensitivity: ~10 V/cm

FIGURE 28. OUTPUT FROM FARADAY CUP ARRAY INDICATING NONUNIFORM BEAM CROSS SECTION (SHOT 3097)

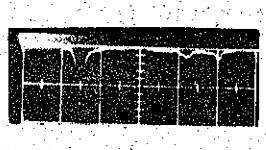

Channel 3
≈ 20 V/cm

Channel 5
≈ 20 V/cm

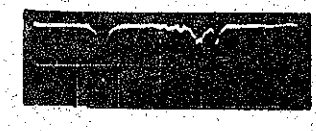

Channel 6
≈ 50 V/cm

Channel 7
≈ 50 V/cm

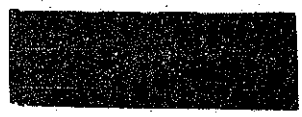

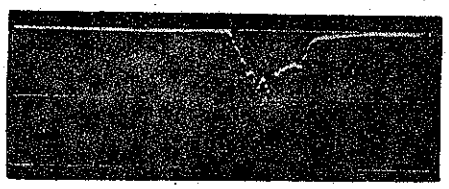

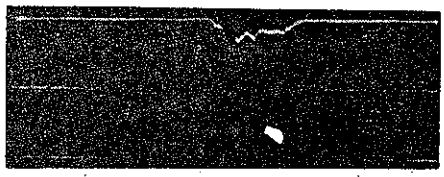

Channel 8
≈ 50 V/cm

Channel 9
≈ 40 V/cm

Sweep Speed: 20 nsec/cm

FIGURE 29. MSA DATA--TYPICAL SHOT EXHIBITING EXTRANEOUS PULSES AND PULSE HEIGHT ASYMMETRIES (SHOT 3123)

TABLE II

RESULTS OF INVESTIGATIONS OF DIFFERENT ANODE-CATHODE CONFIGURATIONS

Cathode	Anode	Diffuser	Switch Gap	Depth Dose Calorimeter	Successful	Partially Successful	Unsuccessful
B_4C @ 15 cm	10 in. x 0.002 in. Ti	None	4.5 in. @ 85 kV	No	6	27	30
B_4C @ 15 cm	10 in. x 0.002 in. Ti	None	4.5 in. @ 85 kV	Yes	9	6	14
B_4C @ 15 cm	10 in. x 0.002 in. Ti	0.050 in. Al	4.5 in. @ 85 kV	No	$\frac{1}{16}$	$\frac{1}{34}$	$\frac{1}{45}$
18-18-0 @ 20 cm	10 in. x 0.002 in. Ti	None	4.5 in. @ 85 kV	No	9	4	2
18-18-0 @ 20 cm	10 in. x 0.002 in. Ti	None	5.0 in. @ 85 kV	No	0	1	1
18-18-0 @ 20 cm	10 in. x 0.002 in. Ti	0.050 in. Al	5.0 in. @ 85 kV	No	2	0	0
18-18-0 @ 20 cm	10 in. x 0.002 in. Ti	0.050 in. Al	4.5 in. @ 85 kV	No	4	3	0

TABLE II (cont.)

RESULTS OF INVESTIGATIONS OF DIFFERENT ANODE-CATHODE CONFIGURATIONS

	Cathode	Anode	Diffuser	Switch Gap	Depth Dose Calorimeter	Successful	Partially Successful	Unsuccessful
Bank:	18-18-0 @ 20 cm	6 in. x 0.002 in. Ti	None	4.5 in. @ 85 kV	No	0	0	3
Bank: 8 kV	18-18-0 @ 20 cm	6 in. x 0.002 in. Ti	None	4.5 in. @ 85 kV	No	1/16	0/8	1/7
	36-36-36 @ 20 cm	10 in. x 0.002 in. Ti	None	4.5 in. @ 85 kV	No	2	2	0
	36-36-36 @ 20 cm	10 in. x 0.002 in. Ti	0.050 in. Al	4.5 in. @ 85 kV	No	4	0	0
	36-36-36 @ 20 cm	10 in. x 0.002 in. Ti	0.050 in. Al	5.0 in. @ 85 kV	No	0	1	0
	36-36-36 @ 20 cm	10 in. x 0.002 in. Ti	0.050 in. Al	5.5 in. @ 85 kV	No	1/7	0/8	0/0

of the shots on the 18, 18 needle cathode, and 100% of the shots on the 36, 36, 36 needle cathode are partially successful.

The calorimetry results did not indicate definite dispersion. The beam was bent, however, and the angle was very close to that predicted. Figures 30 and 31 are side and bottom views of the beam showing the magnet pole tips and the calorimeter. In Figure 30 (Shot 2379), the magnet current is off; in Figure 31 (Shot 2378), the magnet current is on.

A red foil sandwich (Figure 32) was then used to measure the deposition profile along the focal plane of the magnet.

Deposition profiles as a function of x along the calorimeter plane showed a decrease in depth of penetration toward the low-energy end of the calorimeter. Although these results were inconclusive, they were not inconsistent with the possibility that the beam was being dispersed.

In another attempt to check out this possibility, a Faraday cup with a narrow aperture was placed at the site of the calorimeter. If the time dependence of the low-energy portion of the bent beam showed the double-pulse behavior, then it would be fair to assume that the entire beam had been dispersed. The results were disappointing. The double-peak phenomenon was not observed. The pulse shape was roughly consistent with the entire beam-current pulse, indicating that the magnet was probably not sorting out energies. Perhaps the entrance angles are mixed, or the focal properties of the magnet permit mixing of momenta at the site of the Faraday cup.

Side View

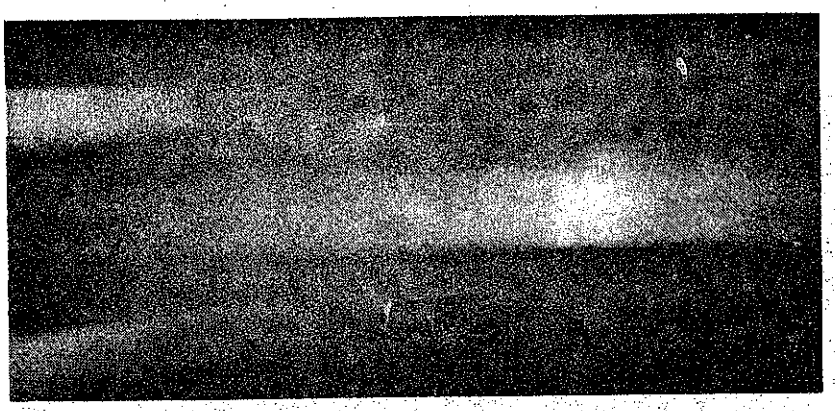

Bottom View

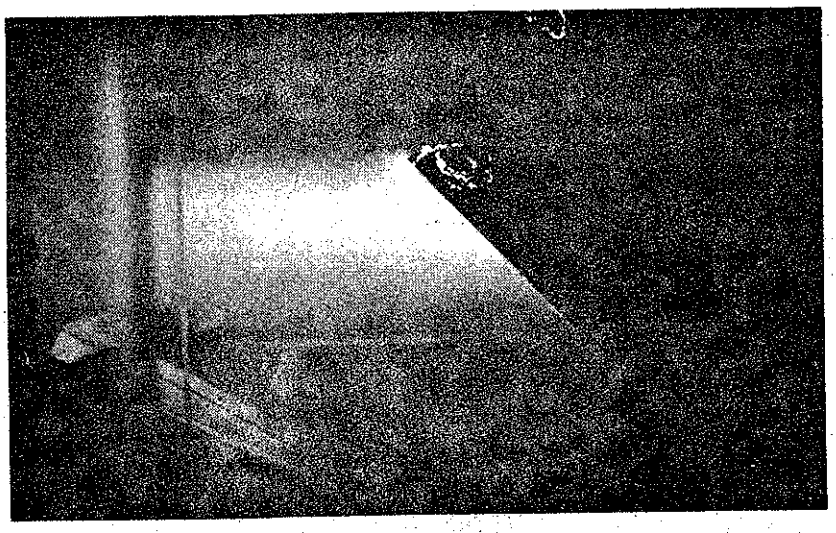

FIGURE 30. MODIFIED QUADRUPOLE EXPERIMENT, MAGNET OFF, 2 Torr, SHOT 2319

Side View

Bottom View

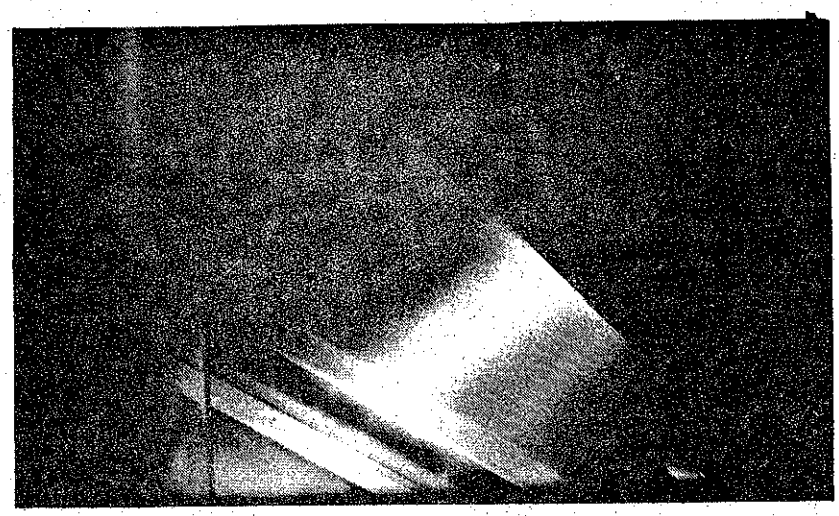

FIGURE 31. MODIFIED QUADRUPOLE EXPERIMENT, MAGNET ON, 2 Torr, SHOT 2378

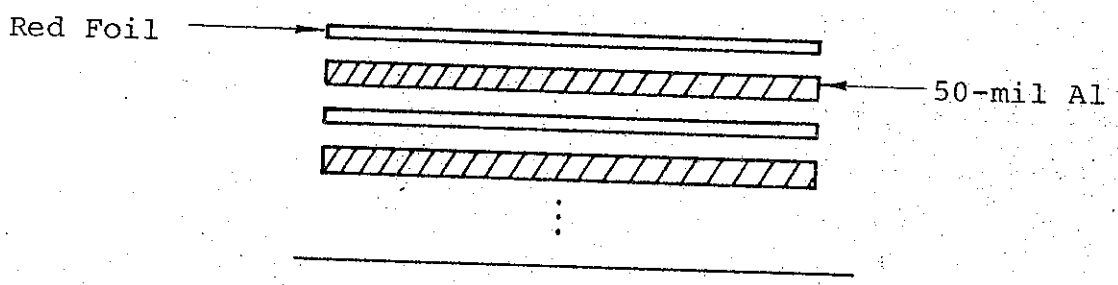

FIGURE 32. RED FOIL DEPTH DOSE CALORIMETER

As an additional item of interest, a pinched beam was shot into the system to see what effect the magnet would have on it. Figure 33 shows the results. The beam seems to have been bent, and also appears to have been smeared out by the magnet. Further experimentation is required to determine if this smearing indicates energy dispersion.

d. Integrated-Output Results from MSA

The integrated output obtained by reading the voltages on the integrating capacitors yields the number of electrons versus electron energy as an integrated intensity spectrum. Given this spectrum, it is possible to calculate a deposition profile in aluminum by means of an available computer code, PIE 2.

The successful demonstration that the MSA was operational, and the observation of the double-peak phenomenon, prompted the studies investigating the behavior of different anode-cathode configurations. However, the long-range objective of this program is to develop a technique for determining the deposition profile of the beam that does not directly interfere with the beam. Specifically, we would hope to use the voltage and current monitors in the anode-cathode region to give us the desired information.

The PIE-2 code has been modified to allow the user to read in corresponding values of current and voltage and obtain a deposition profile in aluminum. Currently this technique is limited by the accuracy in calibration of the voltage monitor, a difficult problem for future work. We then hope to obtain a correlation between the deposition profiles generated by the intensity spectrum and those generated by the current and voltage monitors.

Side View

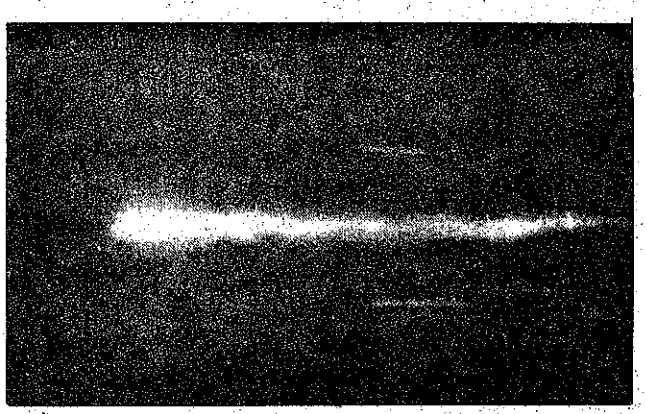

Magnet On

Bottom View

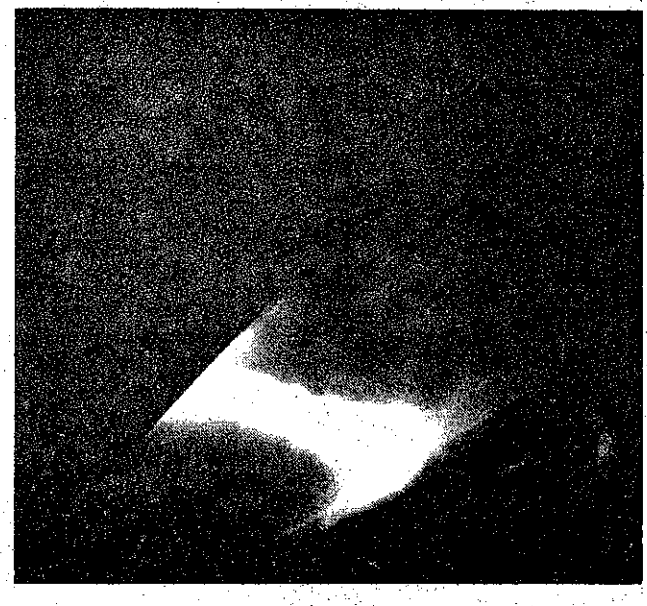

Approx. 20 Kamps
Relativistic Electrons

FIGURE 33. MODIFIED QUADRUPOLE EXPERIMENT WITH PINCHED BEAM, SHOT 2381 (Magnet on, 80 Microns of Pressure, Relativistic Electrons at Approximately 20 kA)

As a result of our experiments with the MSA, much work has been done to develop reliable depth-dose calorimeters. Deposition profiles obtained from the MSA intensity spectra did not agree, even qualitatively, with those obtained from the depth-dose calorimeters then in use. To resolve this discrepancy, we attempted to make some aluminum depth-dose measurements in which the environment was very similar to the MSA environment, using a double aluminum collimator with a 3-mil Mylar window. Pressure around the depth dose was reduced to less than one micron by inserting the depth dose calorimeter in a small vacuum chamber placed within the Model 1140 drift chamber. The results of these experiments agreed at least qualitatively with the PIE-2 results (Figure 34).

Recent work on other contracts has shown that a suitable collimator must be used for aluminum depth-dose measurements. Excellent agreement exists between depth-dose measurements and deposition profiles obtained from current and voltage measurements. However, trial-and-error methods must be used to obtain a calibration of the voltage monitor. Once a good curve fitting is obtained for one shot, profiles may be generated that agree closely with depth-dose measurements on subsequent shots. Figure 35 shows the results for one shot.

f. Conclusions

The MSA has proved to be a valuable experimental tool for analyzing the electron beams generated by the Model 1140 Pulserad machine. The time-resolved output data suggests that it may be possible to produce a double pulse of monoenergetic electrons during a single shot. The time-resolved data, which also provides a measure of beam uniformity and stability, has been extremely useful in evaluating the relative performances of different anode-cathode configurations.

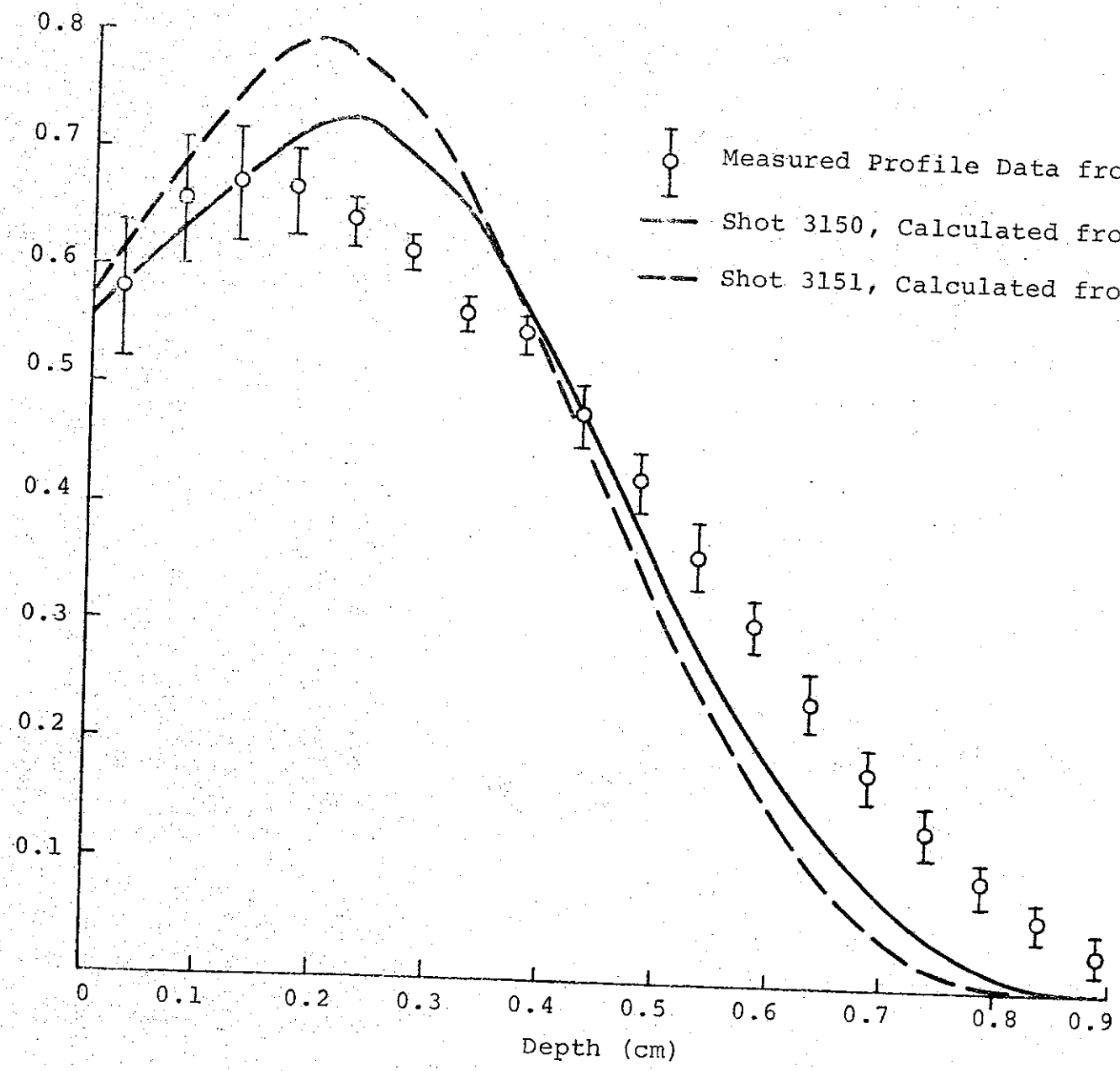

FIGURE 34. ENERGY DEPOSITION IN ALUMINUM--COMPARISON OF MEASURED VERSUS CALCULATED FROM MSA DATA

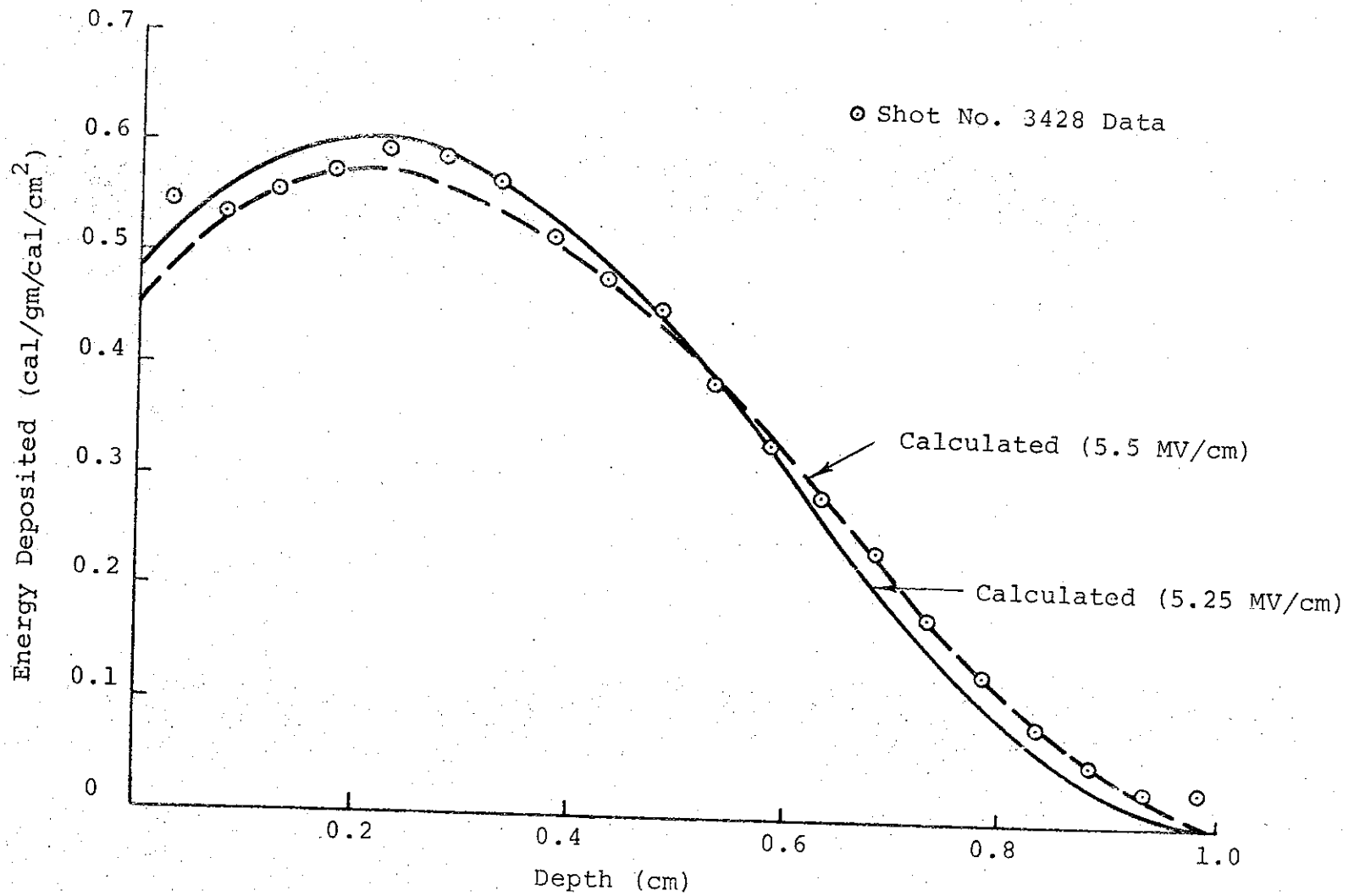

FIGURE 35. DEPOSITION PROFILES FROM CURRENT AND VOLTAGE PROBES VERSUS MEASURED DEPOSITION PROFILE, SHOT 3428

The integrated output yields results that agree substantially with standard depth-dose calorimetry, and with current and voltage measurements. More work must be done in this area, but at this point it appears that we will soon have a reliable method of determining deposition profiles from the voltage and current measurements.

B. BEAM SHAPING WITH FOILS

1. Introduction

Multiple scattering of high energy electrons through a thin target is a process fundamental to the operation of the Physics International electron beam pulsers (Pulserads). Electrons accelerated from the cathode are scattered in penetrating the anode-window, and this scattering represents a significant contribution to the natural width of the resultant electron beam.

Multiple scattering provides a convenient means of broadening a narrow beam of electrons to allow the irradiation of large areas with nearly uniform energy deposition. Irregularities or filamentary structure in the beam are also largely removed through this process. Further, by inserting shaped or composite scattering foils in the path of the beam, it would be possible, in principle, to grossly alter the spatial electron distribution at a target location.

The objectives of the present experiments were two-fold: (1) to determine the extent to which the multiple scattering of high intensity electron beams is predictable by classical multiple scattering laws and (2) to attempt to achieve spatially uniform electron distributions using small, shaped, scattering foils placed between the anode-window and the target. For the first objective, scattering through aluminum and titanium was measured

for both the Model 1140 and 730 Pulserads. For the second objective, the large beam width and wandering of the beam on the Model 1140 Pulserad permitted only qualitative results. The scattered distribution was determined by depositing the beam in graphite calorimeter arrays and using a computer code to calculate and plot the fluence profiles.

To aid in the analysis, a computer code was written that will calculate the theoretical scattering distribution for various foil configurations and for an arbitrary, composite electron spectrum containing up to 10 discrete energies.

2. Theory

One of the most commonly applied theories of multiple scattering and the one with which the present data are compared is due to Moliere. The theory is valid only for small angles, i.e., angles less than about 20 deg and is particularly amenable to analytic calculation. The pertinent equations resulting from this theory as well as a brief summary of the general electron scattering problem follow.

Electrons passing through matter undergo elastic scattering with atoms. In this process the electrons lose energy and are deflected from their original trajectories. Elastic scattering is divided into four classes: (1) single scattering, (2) plural scattering, (3) multiple scattering, and (4) diffusion, defined by the number of collisions an electron is subjected to in penetrating the material. This is determined roughly by the thickness of the material in relation to the parameter $1/\sigma N$ where σ is the cross section and N is the number of atoms per cubic centimeter. Single scattering takes place in materials of thickness $d << 1/\sigma N$

with nearly all the electrons scattered by only one nucleus. Plural scattering occurs for $d \approx 1/\sigma N$ for which there is a large probability that a given deflection is the result of several scattering interactions. Multiple scattering, the primary concern here, occurs for material thicknesses $d > 1/\sigma N$ for which the mean number of collisions is greater than about 20. For multiple scattering the distribution of scattered electrons is described by an approximately gaussian distribution about the centerline with small corrections for single and plural scattering. The classical theory of multiple scattering is well established for scattering angles less than about 20 deg. Complete diffusion of the electrons occurs for material thicknesses $d >> 1/\sigma N$. In this case the mean scattering angle attains a maximum value, $\bar{\theta}_{max} \approx 33$ deg and changes little with increasing material thickness.

The difficulties inherent in understanding of multiple scattering of fast-charged particles have led to a diversity of theories. However, most of them involve approximations, such as thin targets, small scattering angles, and no energy loss, and are thus limited in their domain of validity. The few "exact" theories often cannot be reduced to a form convenient for numerical hand calculations or require so much computation that high speed digital computers are used to evaluate them.

Most theories on multiple scattering are based on the assumption that the scattering is adequately described by ordinary diffusion and this involves solving an integral-differential transport equation with the desired boundary conditions. The Goudsmit-Saunderson theory, for example, gives an expression for the angular distribution valid for any angle using an expansion in Legendre polynomials. The major difficulties with this theory, however, are that it (1) neglects energy loss and (2) is dependent on the actual path

traversed by the electrons rather than on the thickness of the target. Also, extensive computation is required to evaluate the slowly convergent Legendre series.

The Molière theory is basically just the small angle limit of the Goudsmit-Saunderson theory, and pertains to electron energies in the range of 10^4 to 10^7 eV. In this range, the scattering is almost entirely a result of elastic collisions with nuclei, and energy loss is primarily a result of interaction with atomic electrons. Bremsstrahlung losses are practically negligible.

According to the Molière theory, for a monoenergetic, collimated electron beam, the probability that an electron passing through a foil of thickness d is scattered through an angle θ into the solid angle $d\Omega$ is

$$\omega(\theta)d\Omega = \left[2\exp\left(-\frac{\theta}{X_c^2 B}\right) + F_1\left(\frac{\theta}{X_c\sqrt{B}}\right)/B + F_2\left(\frac{\theta}{X_c\sqrt{B}}\right)/B^2 + \cdots\right]\frac{1}{2X_c^2 B}\,d\Omega \qquad (1)$$

where,

$$X_c = \frac{44.8\,Z}{E+E_o/E_o - E_o/E+E_o}\sqrt{\frac{\eta}{A}} \quad \text{(degree)} \qquad (2)$$

This equation is a modified gaussian distribution, and the higher order correction terms F_1 and F_2 account for single and plural scattering which are dominant on the "wings" of the distribution. Z and A are the atomic number and atomic weight of the scattering atoms, respectively, and E and E_o are the kinetic energy and rest energy, respectively, of the incident electrons. η is the areal density in g/cm^2 and is a measure of the thickness of the foil. The width parameter B is a slowly varying function of the number of

collisions, n, where n is given by

$$\text{Log } n = 8.215 + \text{Log}\left[\frac{\eta}{AZ^{2/3}}\,\frac{\gamma^2}{1.13 + 3.76\gamma^2}\right] \qquad (3)$$

In this equation $\gamma = \alpha Z/\beta$ where α is the fine structure constant ($\approx 1/137$) and β is the ratio of electron velocity to the velocity of light. The table below (taken from Reference 3) gives B for various values of Log n. F_1 and F_2 are tabulated in several references (for example, Reference 4).

Log n	B
1	3.36
2	6.29
3	8.93
4	11.49
5	13.99
6	16.46
7	18.90
8	21.32
9	23.71

The mean value of the scattering angle, $\bar{\theta}$, for the above distribution is

$$\bar{\theta} = \frac{\pi}{2} X_c \sqrt{B}\,(1 + 0.982/B - 0.117/B^2 + \cdots) \qquad (4)$$

The angular distribution of scattered electrons is a modified gaussian distribution about the centerline. In the literature, multiple scattering data are often described in terms of either

the above mean scattering angle $\bar{\theta}$ or the angle out to 1/e of the central maximum. Due to the relatively large asymmetry of the beam at large angles in our experiments, however, the scattering was described in terms of the angular deflection out to one standard deviation from the central maximum, i.e., $I(1\sigma) = 0.606\ I_o$. Considering only the first order gaussian term this angle is

$$\hat{\theta} = \frac{1}{\sqrt{2}} X_c \sqrt{B} \quad \text{(degrees)} \tag{5}$$

As a useful rule of thumb this reduces to

$$\hat{\theta} \cong 0.6 \sqrt{\frac{Z\eta}{E}} \quad \text{(radians)} \tag{6}$$

where η is in g/cm^2 and E is in MeV.

A computer code SCATT has been developed during these studies which calculates the scattering distribution using Equations (1) through (3). Up to 10 discrete energies can be included simultaneously and the scattered distribution, through either one or two foils of arbitrary size and distance from the "source" or object point of the electrons, can be calculated. The code was written specifically to calculate the necessary configuration of object-distance, anode-window and intermediate scatterer which would provide an essentially flat intensity distribution over a given target area. The code is further described in Appendix C.

3. Experiments

a. Multiple Scattering

1. Data Handling

The scattering of the Models 730 and 1140 Pulserad electron

beams was measured as a function of scatterer thickness for both aluminum and titanium and is described by plots of the square of the standard deviation and peak intensity versus foil thickness.

The standard deviation σ_s of the intensity distribution resulting from scattering through a scattering foil is, from Equation (5), $\sigma_s = d \tan \hat{\theta}$, where d is the distance between the scattering target and the calorimeter array. However, for small scattering angles ($\tan \theta \approx \theta$),

$$\sigma_s = \frac{d}{57.4} \frac{1}{\sqrt{2}} X_c \sqrt{B} \quad \text{(radians)}$$

Substituting Equation (2) and squaring gives,

$$\sigma_s^2 = \left[\left(\frac{44.8}{57.4} \right)^2 \frac{d^2}{2} \frac{Z^2 \rho B}{\left(E+E_o/E_o - E_o/E+E_o \right)^2 A} \right] t = \alpha t \qquad (7)$$

The relation between the peak intensity I_o and the thickness t of the target is obtained by integrating the intensity distribution over an infinite plane intersecting the beam. Representing the first order term in Equation (1) by $I(r) = I_o \exp(-r^2/2\sigma_t^2)$ where r is the radial distance from the peak of the distribution as measured in the plane, we have

$$W = \int_A I(r)\, da$$

$$W = 2\pi \sigma_t^2 I_o \qquad (8)$$

W is the total incident energy and σ_t is the standard deviation of the intensity distribution as deposited on the calorimeter array. However, since the electron beam incident on the scattering foil is not paraxial, the total standard deviation σ_t includes contributions from the natural beam width from scattering through the anode window, and the geometry of the cathode-anode region as well as from scattering in the scattering foil. For small angles the scattering is independent of the natural width to a good approximation and,

$$\sigma_t^2 = \sigma_o^2 + \sigma_s^2 \tag{9}$$

Substituting into the previous equation gives,

$$W = 2\pi \ (\sigma_o^2 + \alpha t) \ I_o$$

and for a small natural beam width such that $\sigma_s^2 >> \sigma_o^2$ we have

$$\left(\frac{W}{2\pi\alpha}\right) \frac{1}{t} = I_o \tag{10}$$

This equation gives a linear plot of I_o versus 1/t for constant W and α. However, in the experiment W and α were only approximately constant. At least three effects contributed to variation of the total energy W deposited in the calorimeter array: (1) the non-reproducibility of the output of the pulsers, (2) the energy loss in the progressively thicker scattering foils, and (3) edge losses in the calorimeter array (although the solid angle subtended by the array was somewhat larger than the beam solid angle, the ratio was not constant with increasing scattering angle). For a given scattering foil material and experimental configuration α varies very slowly with foil thickness through the parameter B (Table III).

TABLE III

EXPERIMENTAL PARAMETERS AND SUMMARY OF RESULTS
ON MODEL 1140 PULSERAD

Shot No.	Foil (Z)	Thickness (mils)	σ_t (cm)	σ_s^2 (= $\sigma_t^2 - \sigma_o^2$)	I_o (cal/cm^2)	QTOT (cal)
3785	---				120.0	3446
3786	---				134.0	3517
3788	AL(13)	20.0	2.12	1.14	76.0	2896
3789	AL	60.0	2.6	3.40	33.3	1936
3790	AL	120.0	3.15	6.56	16.6	1374
3792	Ti(22)	16.0	2.55	3.16	41.1	2217
3793	Ti	32.0	3.1	6.26	23.4	1777
3794	Ti	48.0	3.2	6.86	17.3	1538
3795	Ti	64.0	3.55	9.26	10.6	1050

Cathode = 600 needle (3.0 in. diam)
Anode-Cathode Dist = 16.0 cm
Anode-Scatt = 5.5 cm
Anode-Calorimeter Dist = 15.0 cm

Mean Energy = 3.8 MeV
Drift Chamber Pressure = 0.5 Torr
Switch Gap = 4.5 in.

One of the ways to determine whether the electron distribution incident on the calorimeter has a gaussian profile is to measure the σ_t and I_o and substitute them into Equation (8) to calculate the total calories, W. The difference between this value and the measured value should be small (i.e., within the limits of error of W as described above) for the gaussian profile approximation to apply. This check was done for some of the data from the Model 1140 Pulserad and is discussed in that section.

Plots were made of Equation (6) for each material and experimental configuration and compared with the experimental data. In the experiment with the Model 1140 Pulserad σ_t could not be resolved from σ_o for foil thicknesses within the range of validity of Equation (6), so the experimental data are shown with a plot of Equation (6) for foil thicknesses within its range of validity.

2. Model 1140 Pulserad Data

The Model 1140 Pulserad was configured in the high impedance mode. A 600-needle cathode identical to the Model 730 cathode was used with an anode-cathode distance of 16 cm. The anode window was 2-mil titanium with a 10 in. diameter. The beam had a small natural width (no collimator was used) and the energy spectrum had a mean value of about 3.8 MeV. The experimental configuration is shown in Figure 36.

The calorimetry consisted of a 7 x 7 graphite array with 1.0- x 1.0-in. blocks 0.5 in. thick. The location of the scattering foil with respect to the calorimeter (a 10-cm separation) was such that the solid angle subtended by the calorimeter was larger than the largest scattering solid angle.

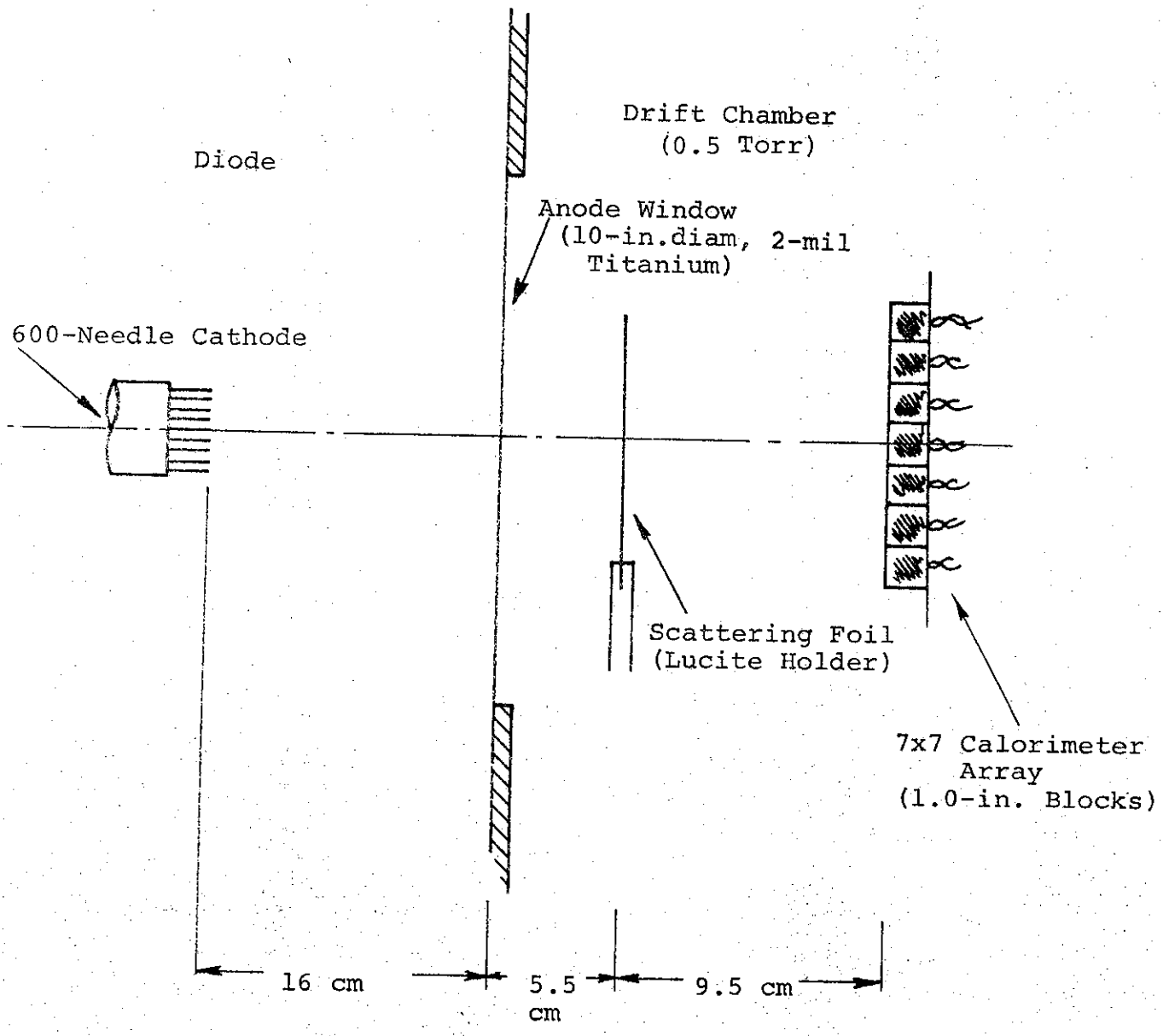

FIGURE 36. SCATTERING FOIL CONFIGURATION, MODEL 1140 PULSERAD

5965

The scattering was measured for both aluminum and titanium. A summary of the experimental parameters and results is given in Table III. A short computer program was written to calculate the fluence distribution on the calorimeter array. It calculates the position of the center of the distribution using moments of force, assuming that all the calories in each block are deposited at its center. The result is a plot on the Cal-Comp plotter of the energy deposited in each block versus its distance from the calculated center of the distribution.* Plots of σ_s^2 versus t and I_o versus 1/t are in Figures 37 through 40. The smooth curve on the plots σ_s^2 versus t represent the theoretical scattering in the range of validity of the Molière theory. Beam scattering profiles for individual shots is presented in Appendix B, Section I.

From Figures 37 through 40 it is seen that the experimental data differ significantly from the theory even for the single measurement (with 20-mil aluminum) within its range of validity. The data indicate a less rapid spread of the distribution with increasing scatterer thickness than the theory predicts; however, the scattering for both materials was accurately described by Equation (6) with a different numerical coefficient. Thus,

$$\hat{\theta} = 0.32 \frac{\sqrt{Z\ \eta}}{E} \quad \text{(radians)}$$

Since all the data were measured with a mean incident beam energy of 3.8 MeV, further measurements are needed to verify this relation at other energies as well as for other beam geometries and scatterers (Z,η). One of the possible reasons accounting for the narrow

*The computer code could not be used to plot the Model 730 data because for many of the shots the peak of the scattered beam was near the edge of the 6 x 6 array, thus invalidating the moment calculation due to the lost calories. Hence, skewness of the distribution as registered by the calorimeter results.

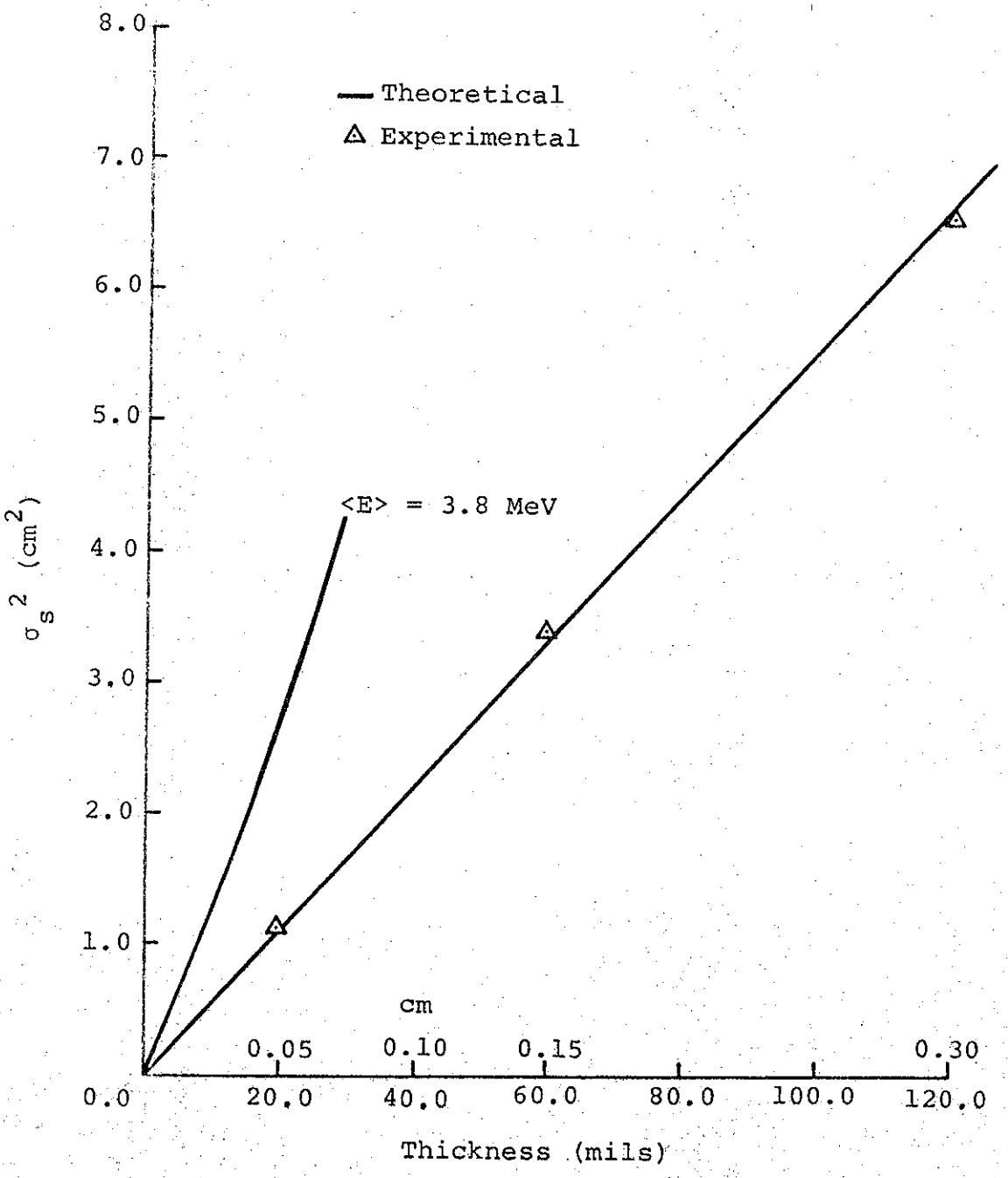

FIGURE 37. SCATTERING IN ALUMINUM, MODEL 1140 PULSERAD (DSWPLT Analysis) σ_s^2 VERSUS t at 9.5 cm

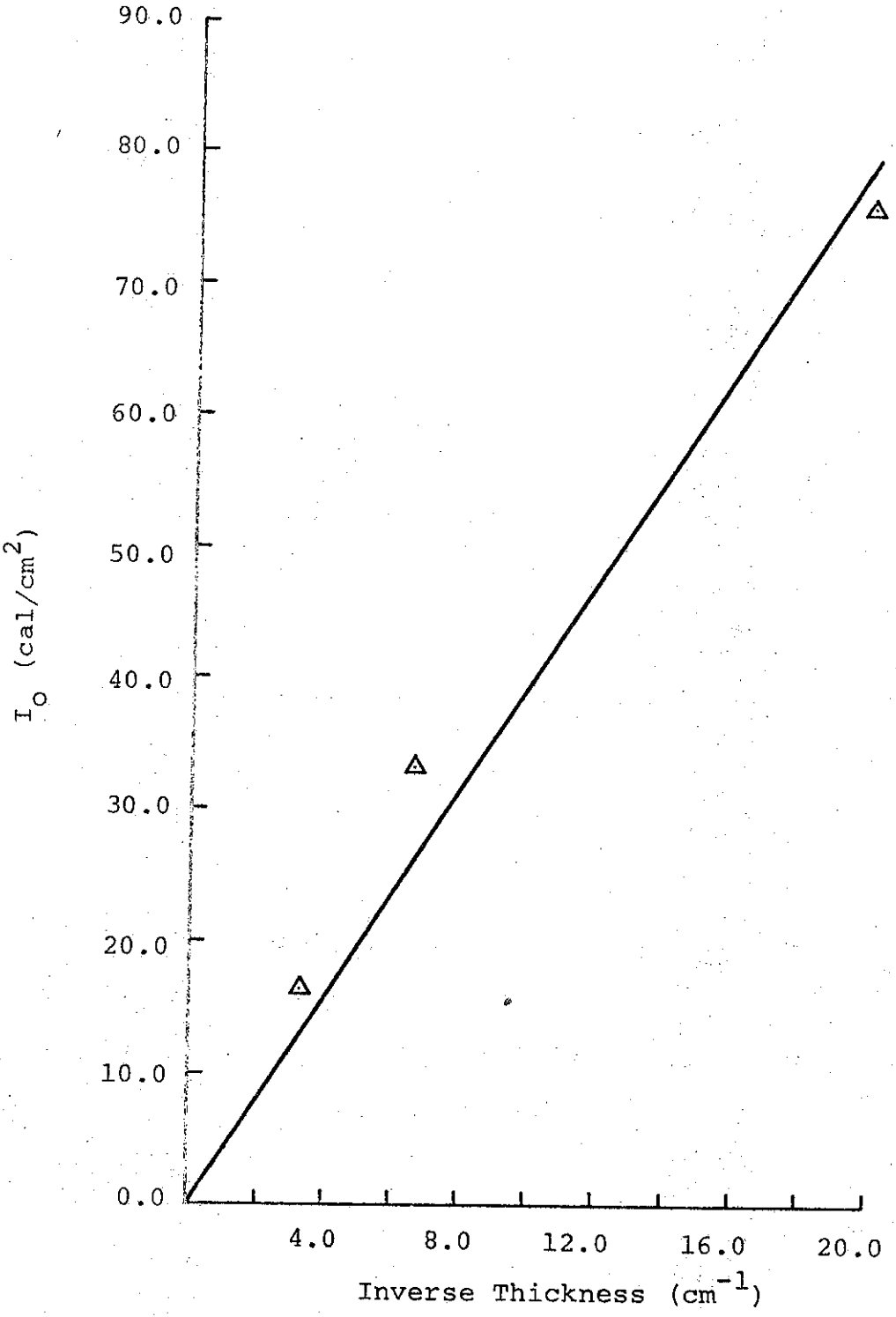

FIGURE 38. SCATTERING IN ALUMINUM, MODEL 1140 PULSERAD (DSWPLT Analysis), I_o VERSUS 1/t at 9.5 cm

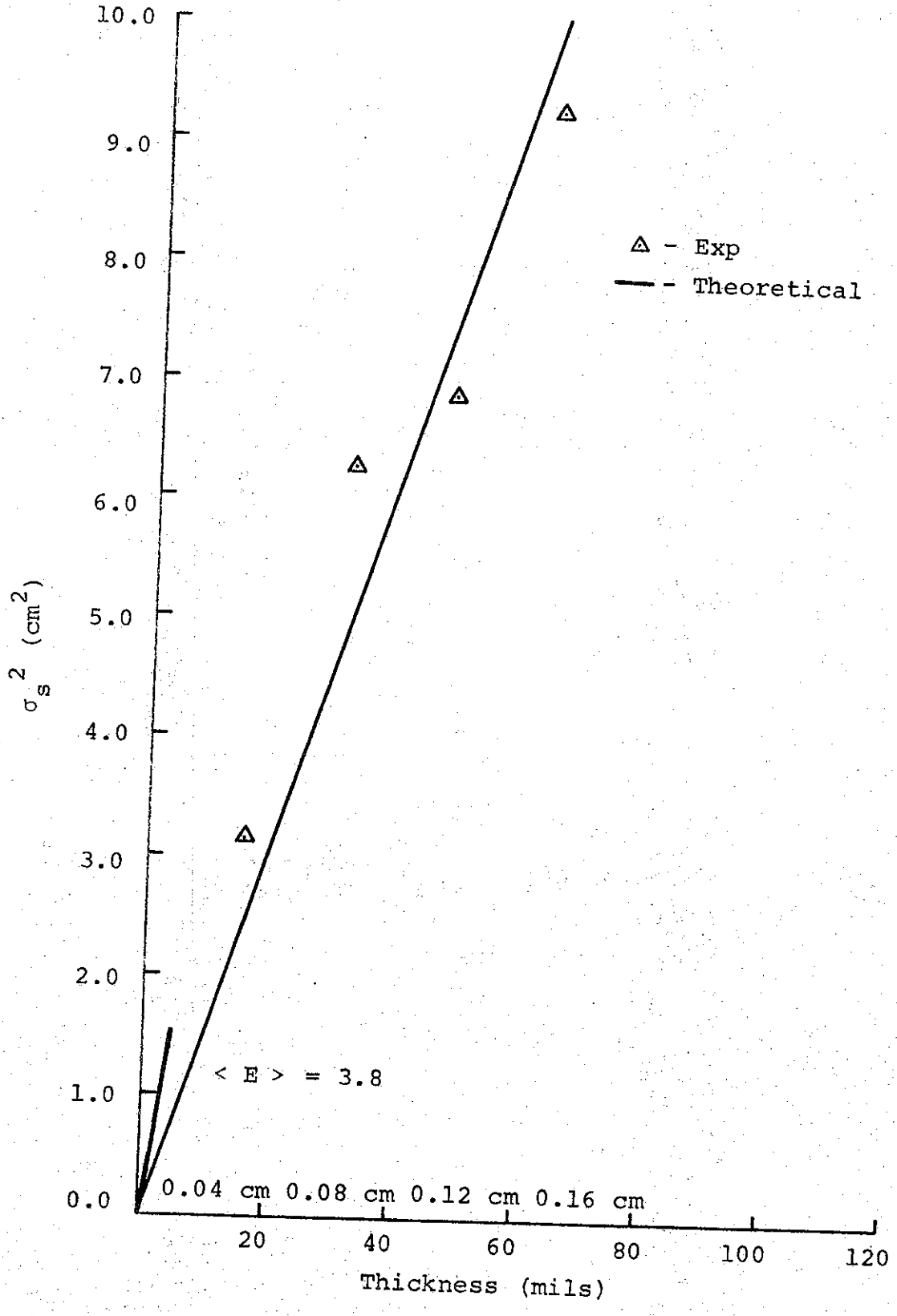

FIGURE 39. SCATTERING IN TITANIUM, MODEL 1140 PULSERAD (DSWPLT), σ_s^2 VERSUS t at 9.5 cm

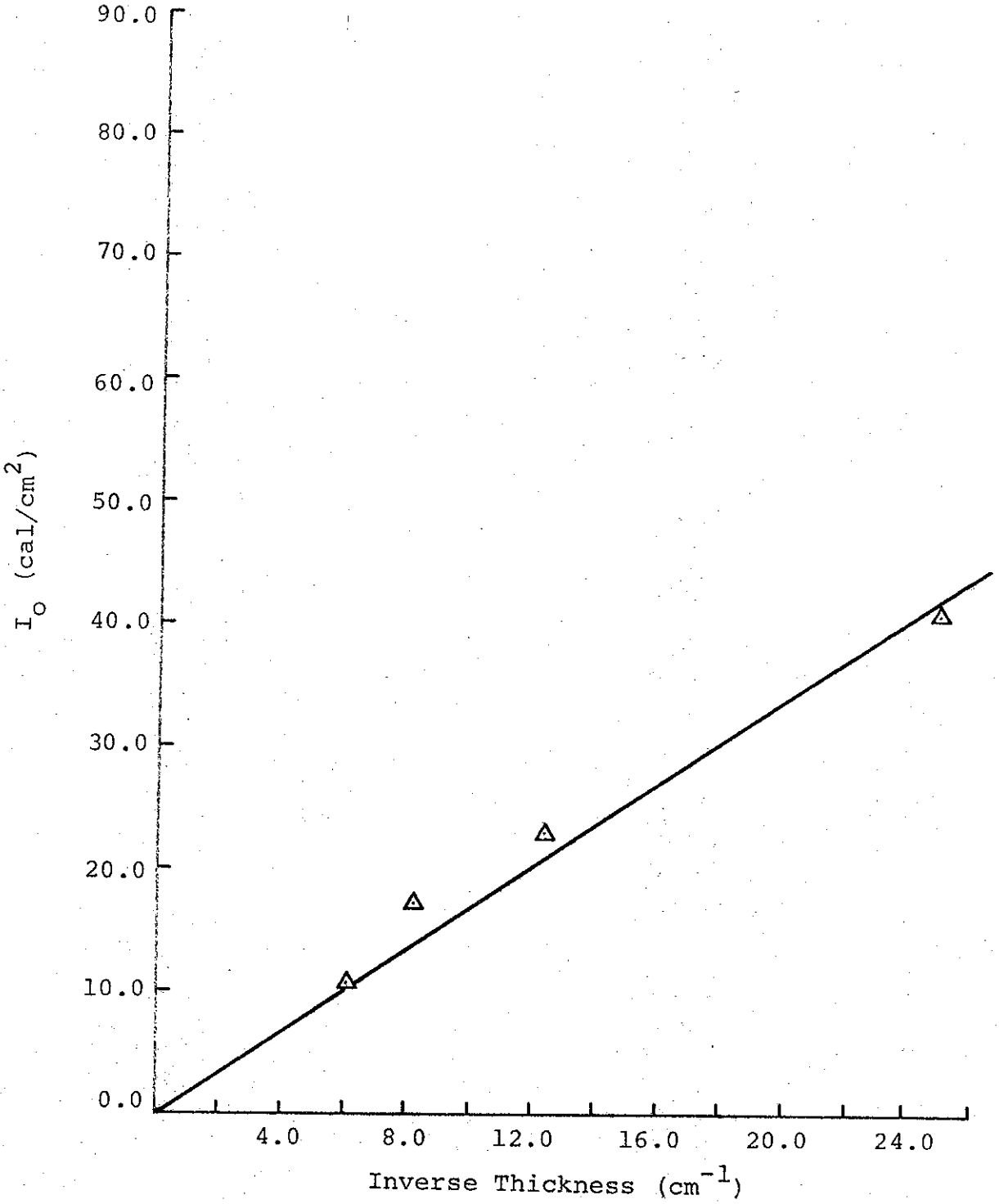

FIGURE 40. SCATTERING IN TITANIUM, MODEL 1140 PULSERAD (DSWPLT Analysis) I_o VERSUS 1/t at 9.5 cm

profile of the present data is magnetic forces resulting from the large current densities. The approximate average current density incident on the scattering foils was calculated from the total calories as,

$$\bar{j} = \frac{\bar{I}}{\pi\sigma_o^2} = \frac{W}{\bar{E}\, t_p\, \pi\sigma_o'^2}$$

where W is the total energy expressed in joules, $\bar{E}$ is the mean energy, t_p is the pulse length and σ_o' is the standard deviation of the incident beam at the position of the foil. The value of σ_o' was calculated from σ_o by spherical divergence with the cathode as the center. From the shots without foils we have,

$$\bar{j} = \frac{1.4 \times 10^4}{3.8 \times 10^6 \times 10^{-7} \times 3.14 \times 1.5}$$

$$\bar{j} = 7.8 \text{ kA/cm}^2$$

The "skin depth" of the magnetic field in aluminum and titanium at the frequency corresponding to a 100-nsec pulse length is only δ = 1.46 mils and δ = 3.08 mils, respectively, so that, at least in the present data, the magnetic fields penetrated a small fraction of the foil thickness. The shift of the data from the theory, however, may be due to some macroscopic effect of the current density. Further experiments are needed to attempt to define this interaction.

Further analysis of the effects of the scattering process on the behavior of the beam, in particular the change in fluence profile as a function of foil thickness, was possible because of the quality and consistency of the data. The beam as transmitted

through the anode window appeared to have a nearly gaussian profile out to approximately one standard deviation from the axis but was increasingly nongaussian for greater radial distances. However, as successively thicker scattering foils were placed in the beam, it became more diffuse (larger σ_t) and the "wings" of the distribution more nearly matched the gaussian profile of the central portion. This behavior is seen from gauss plots of the fluence profiles for the shots with aluminum foils--Figures 41, 42, and 43.* A straight line on a gauss plot indicates a pure gaussian distribution, and the standard deviation is determined from its slope. The amount of energy contained in the nongaussian "wings" of the distribution, however, is a small percentage of the total deposition. This is shown in the table that follows, which lists the total measured calories (QTOT), the theoretical value (W) calculated from Equation (8) and the difference (Δcal) expressed as a percentage for the shots with aluminum foil.

COMPARISON OF THEORETICAL AND EXPERIMENTAL ENERGY DEPOSITION AFTER SCATTERING THROUGH ALUMINUM FOILS (MODEL 1140 PULSERAD)

Shot No.	Foil Thickness (mil)	QTOT (cal)	$W = 2\pi\sigma_t^2 I_o$ (cal)	Δcal/QTOT x 100 (%)
3785	---	3446	2520	27
3789	60	1936	1936	27
3790	120	1374	1030	25

*A gauss plot shows the normalized integral spectrum for a gaussian distribution and is plotted on probability paper. G(x) is plotted versus x where,

$$G(x) = \frac{\int_0^x I(x)\,dx}{\int_0^\infty I(x)\,dx}$$

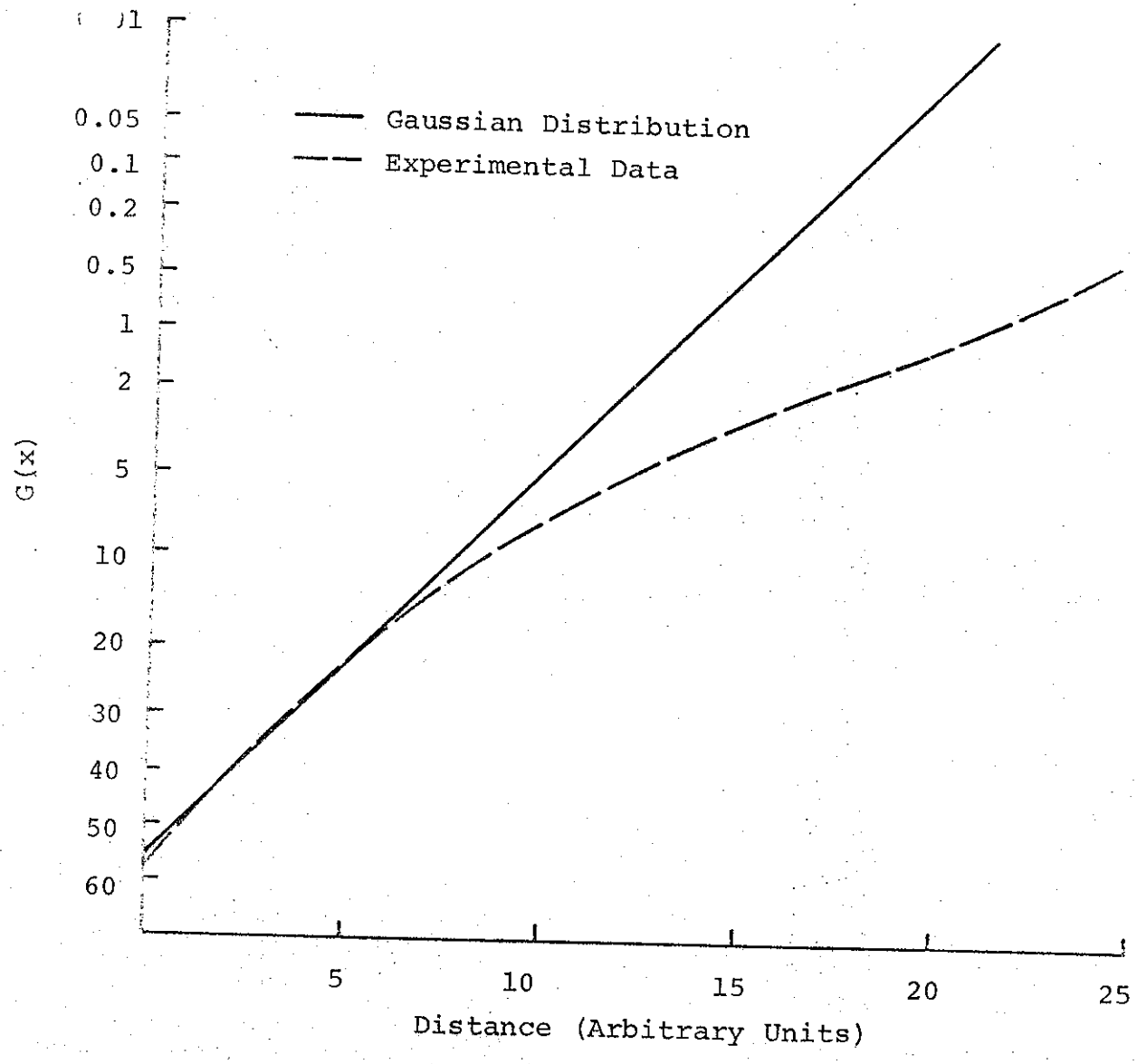

FIGURE 41. GAUSS PLOT OF FLUENCE DISTRIBUTION (NO SCATTERING FOIL), MODEL 1140 PULSERAD, SHOT 3785

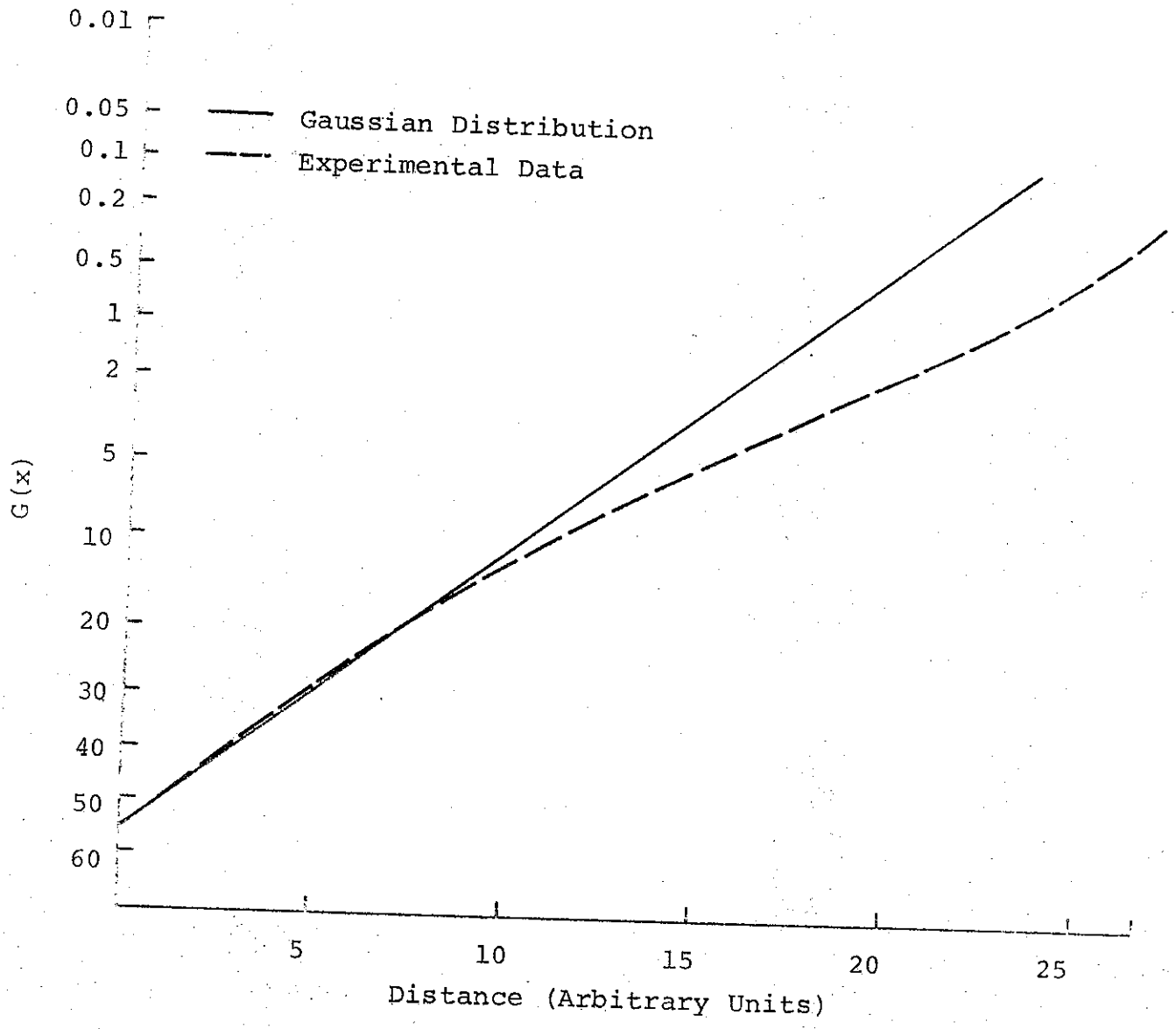

FIGURE 42. GAUSS PLOT OF FLUENCE DISTRIBUTION (60-mil ALUMINUM SCATTERER), MODEL 1140 PULSERAD, SHOT 3789

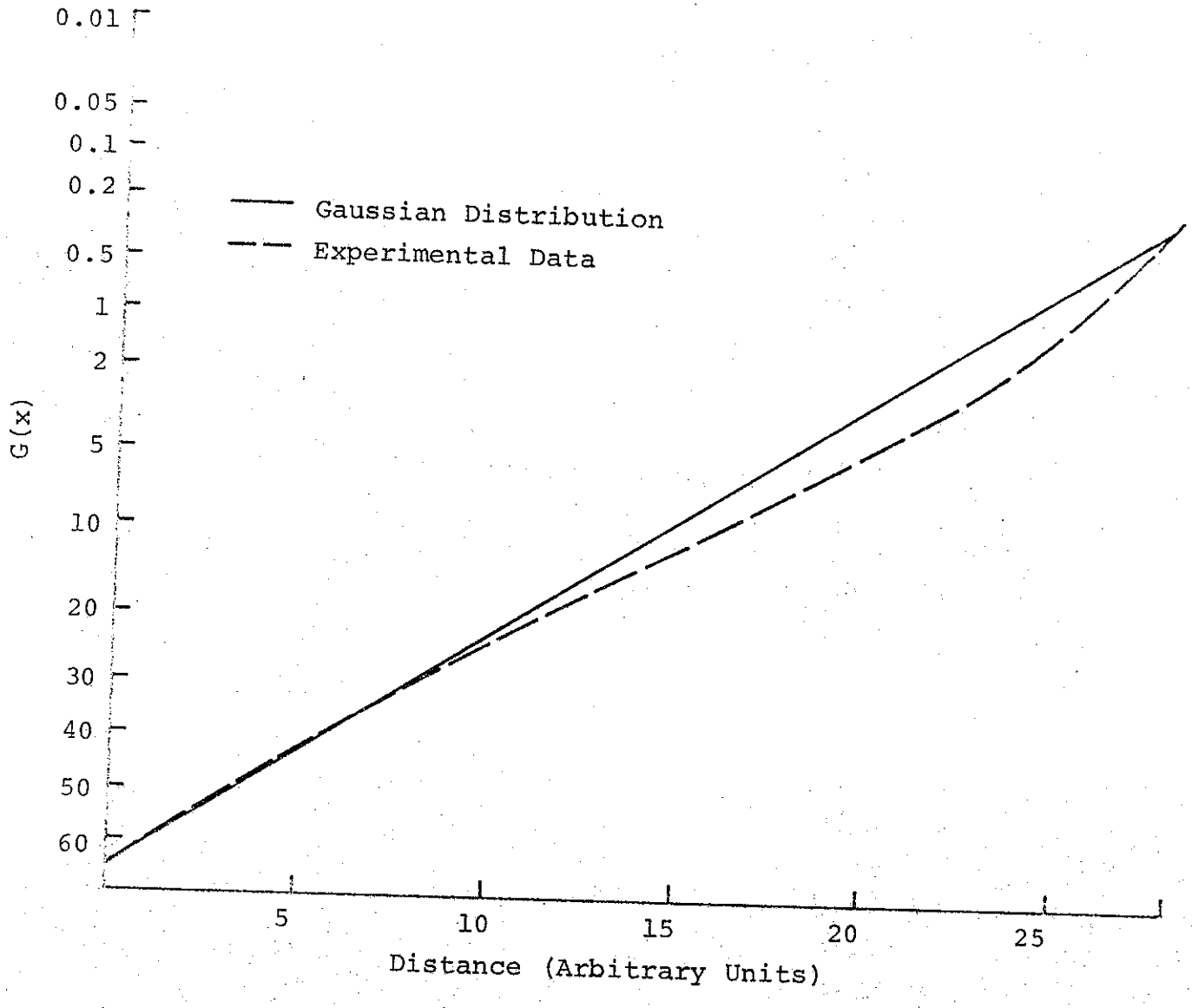

FIGURE 43. GAUSS PLOT OF FLUENCE DISTRIBUTION (120-mil ALUMINUM SCATTERER), MODEL 1140 PULSERAD, SHOT 3790

The approximately 25% discrepancy between the measured and theoretical values for the nearly gaussian profile of Shot 3790 is likely due to the limited spatial resolution of the calorimeter blocks and to the fact that all the blocks were not necessarily measured at their peak. These effects would significantly alter the values of σ_t and I_o. It is hoped that with greater refinement of calorimetry techniques this discrepancy can be reduced still further.

b. Beam Shaping

1. Introduction

The purpose of the beam shaping experiments was to attempt to achieve spatially uniform electron distributions over relatively large target areas by interposing small scattering foils in the path of the beam. Ideally the effect of the foils might be as depicted in Figure 44. The central portion of the electron distribution is scattered by the small foil resulting in an area with fairly uniform energy deposition at the position of the target.

The experiments were conducted using the Model 1140 Pulserad in essentially the same configuration as for the experiments of Section III,B,3,a,2 except that, at that time, the 600-needle cathode had not been developed and an 18,18,0-needle cathode was used instead. One of the major problems with this cathode was beam wander and this set severe limits on the accuracy of the beam shaping experiment. A summary of the experimental parameters is given in Table IV.

The calorimetry consisted of a large 5 x 5 array of 2-in. by 2-in. blocks 0.5-in.-thick with the center block replaced by a

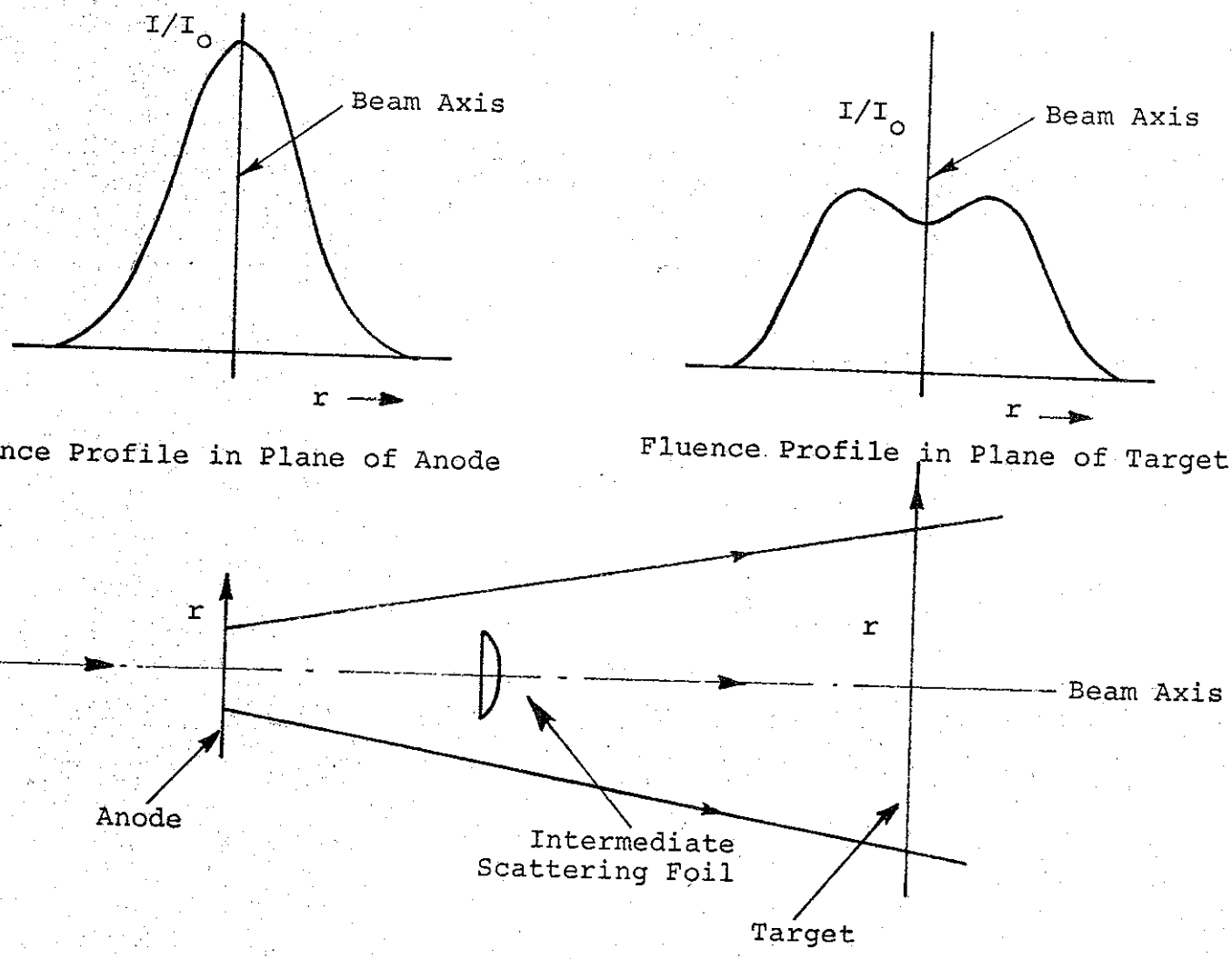

FIGURE 44. SHAPED BEAM PROFILE (Qualitative)

TABLE IV

SUMMARY OF BEAM SHAPING EXPERIMENTAL DATA

Pulse	Anode-to-Cathode Distance (cm)	Anode-to-Calorimeter Distance (cm)	Anode-to-Intermediate Scatterer Distance (cm)	Intermediate Scatterer Thickness (mil)	Intermediate Scatterer Radius (cm)	Relative Fluence (cal/cm^2)		
						1x1-in. Blocks	L-Blocks	2x2-in. Blocks
2806	15	10	5	2	1	0.87	0.53	0.20
2807	15	10	5	2	1	0.93	0.53	0.18
2808	15	10	5	2	1	0.93	0.62	0.13
2809	15	10	5	2	2	1.08	0.53	0.19
2810	15	10	5	2	2	1.11	0.60	0.18
2812	15	10	5	4	2	0.55	0.47	0.24
2813	15	10	5	4	2	1.25	0.54	0.18
2815	15	10	3	2	2	1.28	0.40	0.19

small 5 x 5 array of 0.5-cm by 0.5-cm blocks enclosed by four L-blocks. Measurements were made of the fluence deposited in the blocks as a function of their distance from the axis with no compensation for the shifting of the peak due to beam wander. All the blocks at a given distance from the axis were then averaged to determine the value of the fluence. Three distances were chosen corresponding to the average distance off-axis of the large 2-in. by 2-in. blocks, the average distance off-axis of the L-blocks, and the small 5 x 5 array measured the fluence on axis. The fluence at these three distances is plotted for each scattering foil configuration.

Three configurations were tested using titanium foil (Table IV). The anode-calorimeter and anode-cathode distances were held constant and the anode-scatterer distance, scatterer thickness, and radius were varied. The data are plotted in Figures 45, 46, and 47 and give a qualitative indication of effects.

2. Model 730 Pulserad Data

The Model 730 Pulserad was configured in the low energy mode. The electron beam had a mean electron energy of 1.0 MeV and a natural width at one standard deviation of approximately 0.5 cm. A 600-needle cathode was used with an anode-cathode distance of 1.0 cm. Half-mil aluminized Mylar served as the anode window. The experimental configuration is shown in Figure 45.

The calorimetry consisted of a small 6 by 6 graphite array with 0.5- by 0.5-cm blocks 0.5 in. thick. The distance between the scattering foil and the array was 3.5 cm and was determined such that the solid angle subtended by the array was larger than the largest solid angle of the scattered beam.

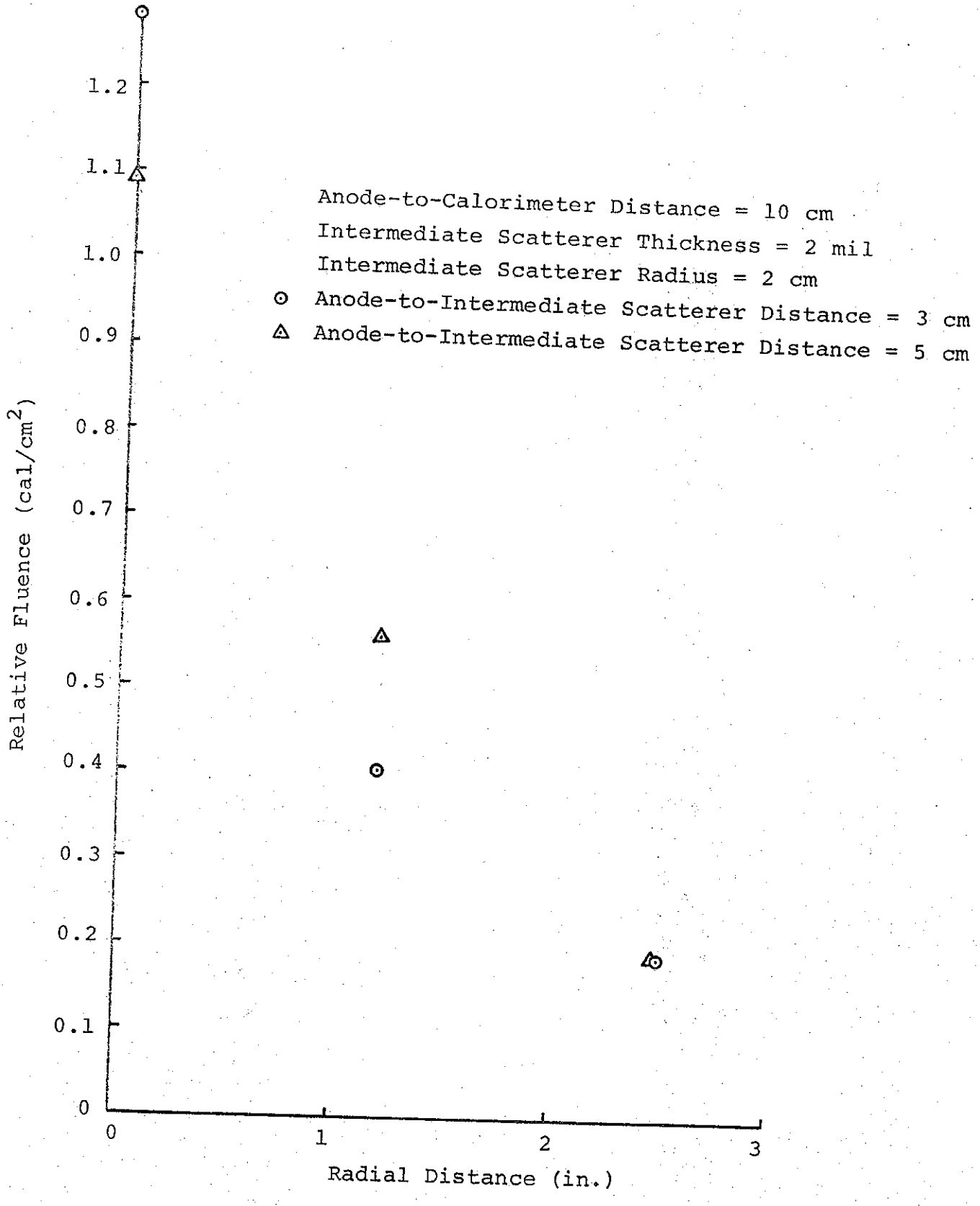

FIGURE 45. INTENSITY VERSUS DISTANCE FROM ANODE TO INTERMEDIATE SCATTERER

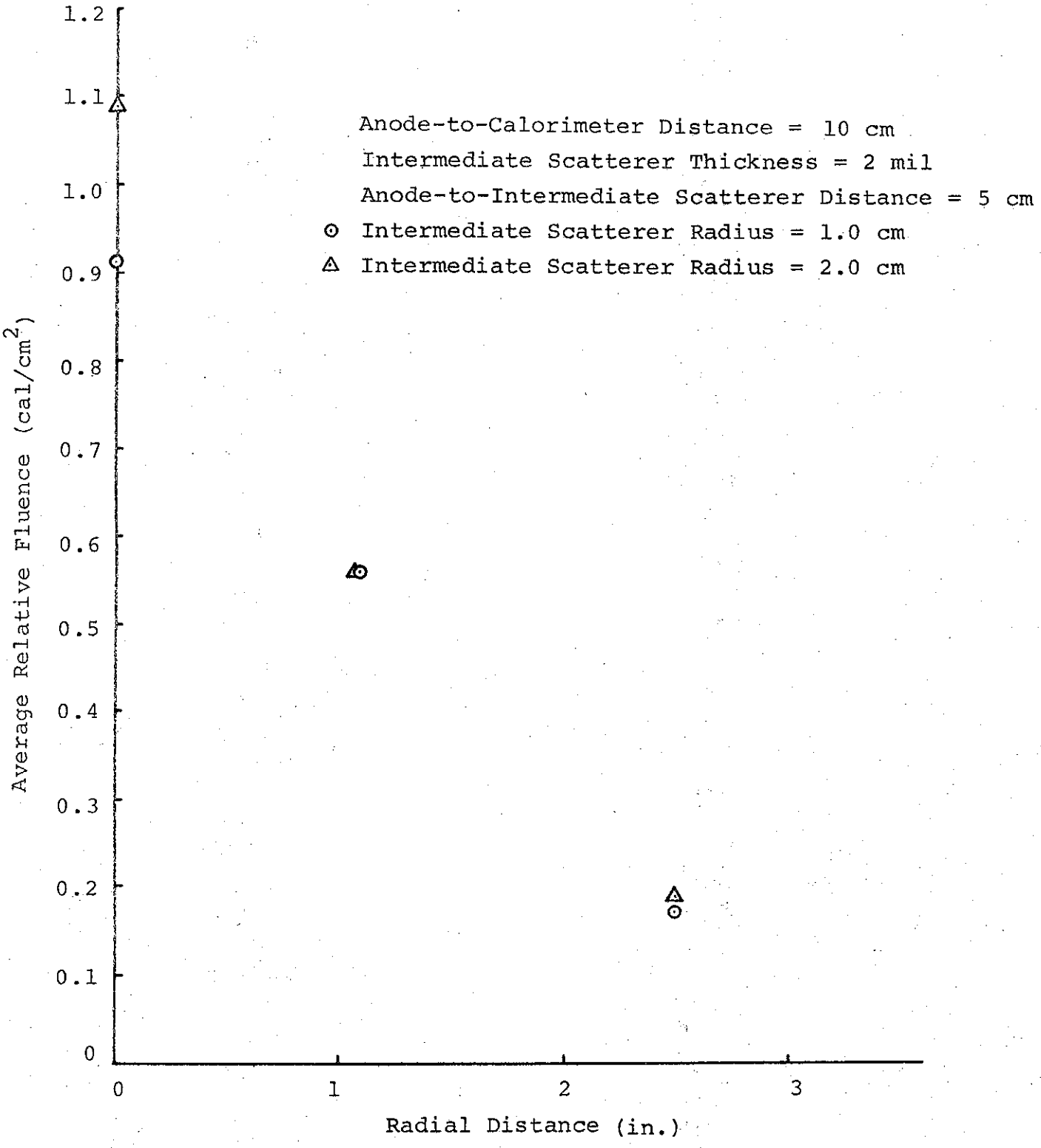

FIGURE 46. INTENSITY VERSUS RADIUS OF INTERMEDIATE SCATTERER

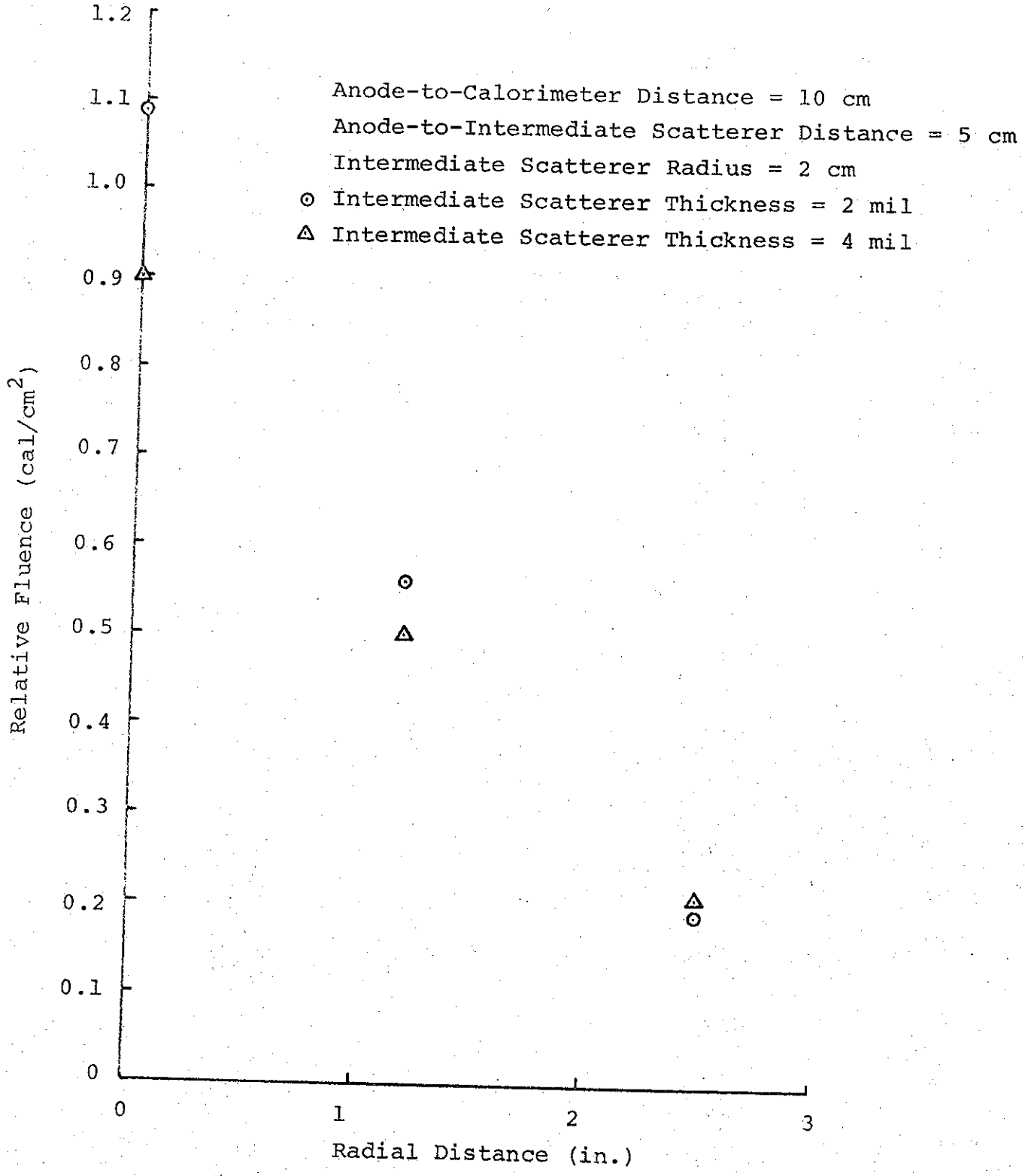

FIGURE 47. INTENSITY VERSUS THICKNESS OF INTERMEDIATE SCATTERER

Scattering was measured in aluminum and titanium foils for two experimental configurations but with the same mean beam energy and natural width for both.

The first configuration is shown schematically in Figure 48. The electron beam was injected through 3/4-in. diameter holes in the brass collimator plates with the scattering foils placed over the second hole. The experimental parameters and a summary of the results appear in Table V.

The second configuration is shown schematically in Figure 49. The copper cone essentially replaced the second collimator plate, and it was hoped that this would increase the fluence reproducibility. The foils were placed over the exit of the cone with the same overall dimensions preserved. The experimental parameter and results are summarized in Table VI.

Plots of σ^2 versus t and I_o versus 1/t for both configurations appear in Figures 50, 51, 52, and 53. Beam profiles appear in Appendix B, Section II. The variation in the data points is in part due to the low resolution of the calorimeter array; however, this does not explain the large divergence of the data for the second configuration from the theory (solid line in Figure 50 and 52). A possible explanation for this is that the current densities in the beam are high enough that the collective magnetic forces of the electron beam affect the motion of individual electrons within the beam. Since scattering is determined by the number of collisions an electron makes in penetrating a material, the collective forces could also act during the scattering process if the "skin depth" of the magnetic fields is an appreciable fraction of the material thickness.

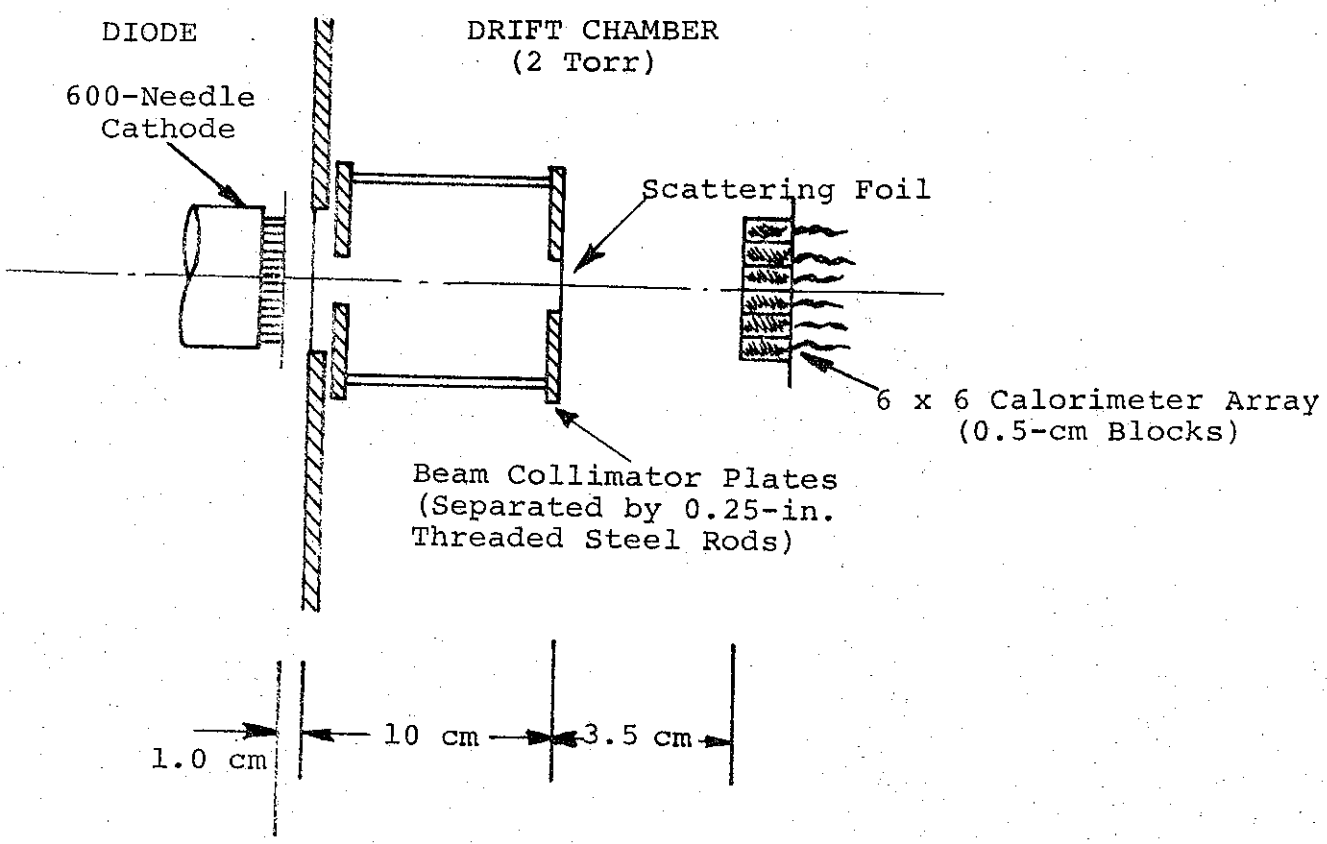

FIGURE 48. SCATTERING FOIL CONFIGURATION I (COLLIMATOR PLATES), MODEL 730 PULSERAD

5965

TABLE V

EXPERIMENTAL PARAMETERS AND SUMMARY OF RESULTS WITH COLLIMATOR, MODEL 730 PULSERAD

Shot No.	Foil	Thickness (mils)	Areal Density (mg/cm^2)	σ_t (cm)	σ_s^2 (= $\sigma_t^2 - \sigma_o^2$)	I_o (cal/cm^2)	QTOT (cal)
9659	---	None	0	$\sigma_o = 0.48$	0	118.0	181
9660	Al	1.8	12.4	0.65	0.25	64.5	161
9661	Al	0.9	6.2	0.57	0.15	71.0	188
9662	Ti	0.5	5.7	0.55	0.13	55.8	141
9663	Ti	1.0	11.4	0.67	0.28	30.0	117
9664	Al	2.7	18.6	0.76	0.41	29.0	118
9665	---	None	0	$\sigma_o = 0.35$	0	85.0	158

Cathode = 600 needles (3.0 in. diam)

Anode-Cathode Distance = 1.0 cm

Anode-Scatterer Distance = 10 cm

Anode-Calorimeter Distance = 13.5 cm

$\overline{\sigma}_o^2 = 0.17\ cm^2$

Mean Energy = 1.0 MeV

Switch Gap = 3.0 in.

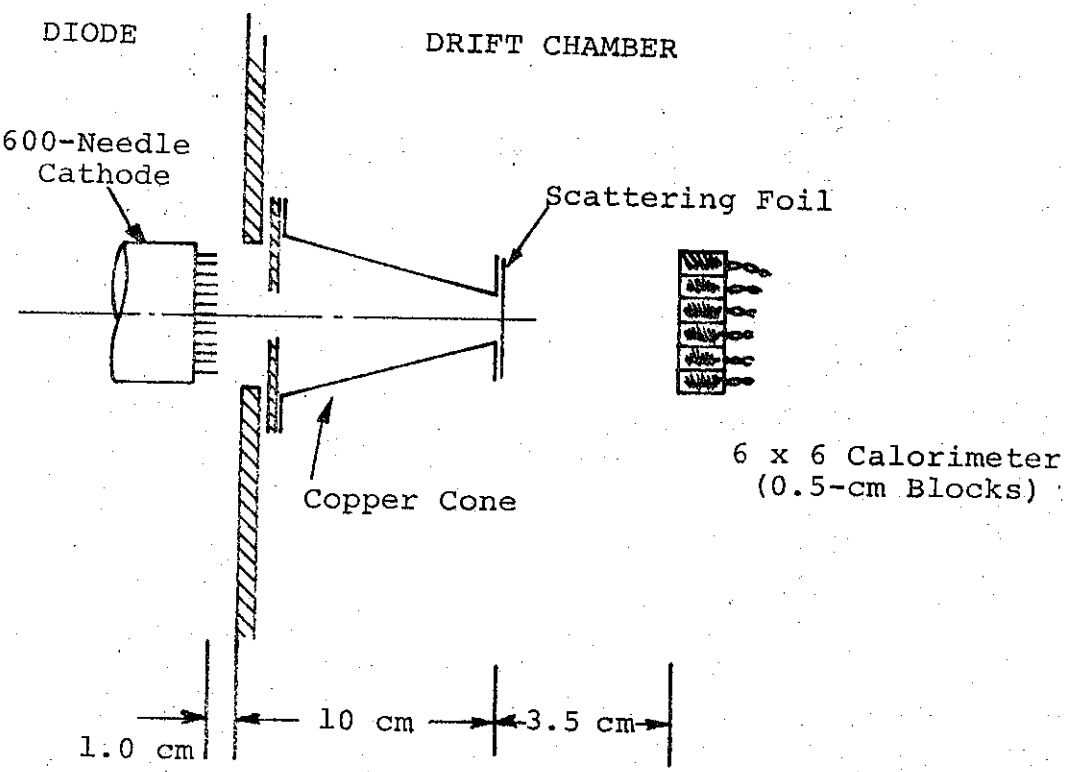

FIGURE 49. SCATTERING FOIL CONFIGURATION II (CONE)
MODEL 730 PULSERAD

TABLE VI

EXPERIMENTAL PARAMETERS AND SUMMARY OF RESULTS WITH CONE ON MODEL 730 PULSERAD

Shot No.	Foil (Z)	Thickness (mils)	Areal Density (mg/cm^2)	σ_t (cm)	σ_s^2 (= $\sigma_t^2 - \sigma_o^2$)	I_o (cal/cm^2)	QTOT (cal)
9686	None	---	0	$\sigma_o = 0.45$	---	91.0	190.5
9687	Ti(22)	1.0	11.4	0.55	0.10	19.5	187.5
9688	Al(13)	1.8	12.4	0.45	---	31.5	208.0
9689	Ti	0.5	5.7	0.39	---	59.0	345.2
9690	Al	2.7	18.6	0.55	0.10	53.5	166.5
9691	Al	0.9	6.2	0.51	0.06	46.5	105.3

Cathode = 600 needles (3.0 in. diam)

Anode-Cathode Distance = 1.0 cm

Anode-Scatterer Distance = 10 cm

Anode-Calorimeter Distance = 13.5 cm

$\bar{\sigma}_o^2 = 0.20\ cm^2$

Mean Energy = 1.0 MeV

Switch Gap = 3.0 in.

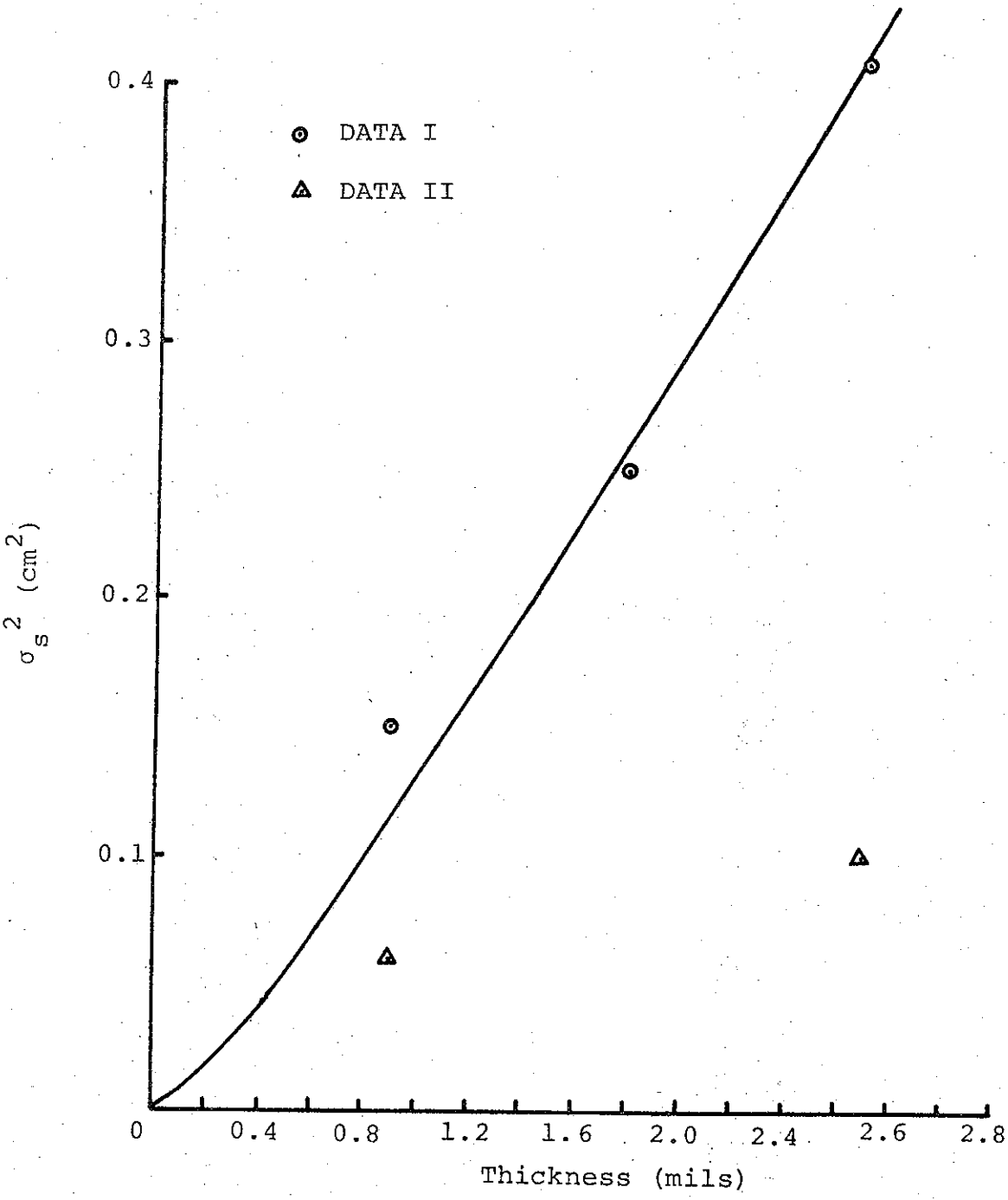

FIGURE 50. σ_s^2 VERSUS t AT 3.5 cm, MODEL 730 PULSERAD, ALUMINUM

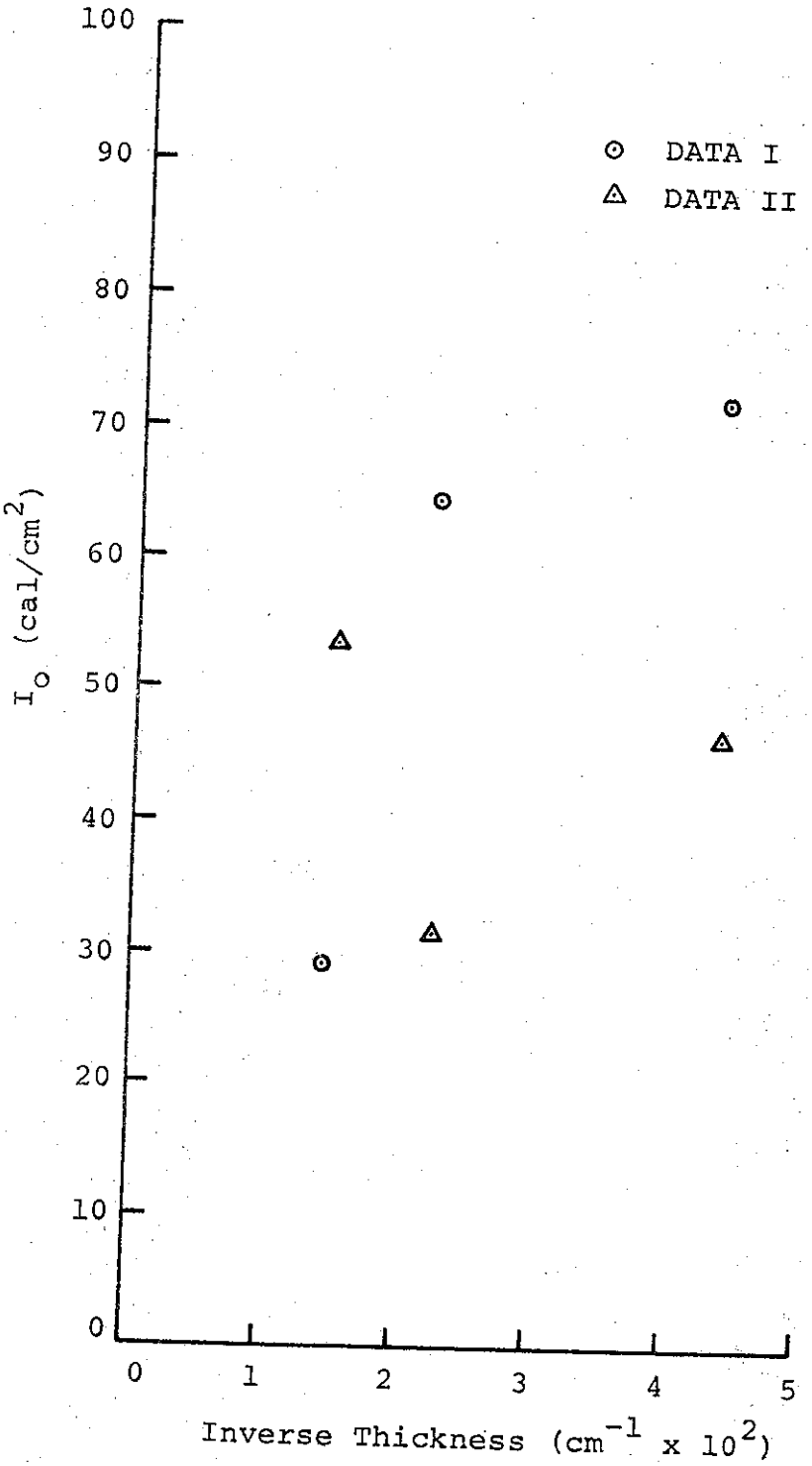

7874

FIGURE 51. I_o VERSUS 1/t AT 3.5 cm, MODEL 730 PULSERAD ALUMINUM.

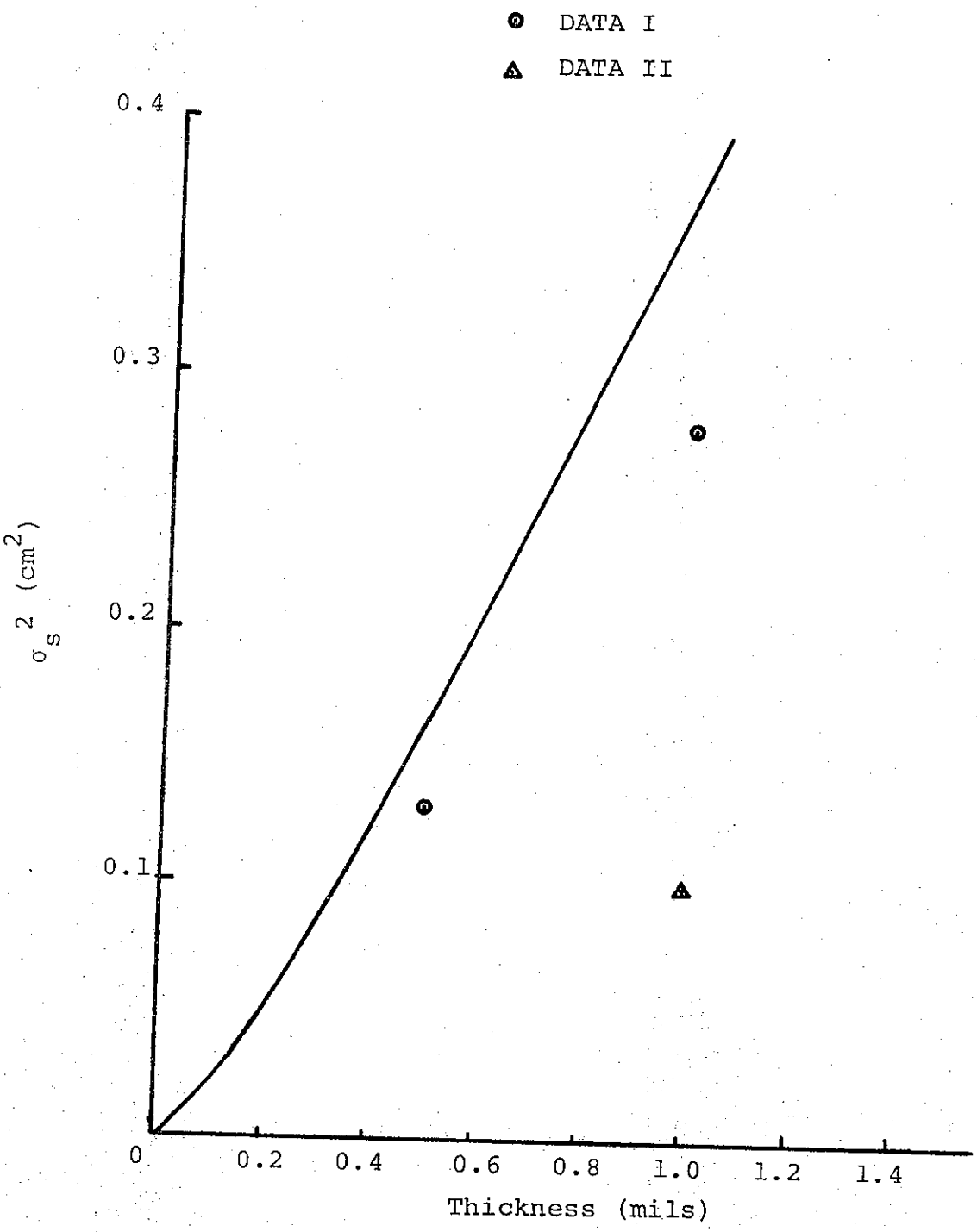

FIGURE 52. σ_s^2 VERSUS t AT 3.5 cm, MODEL 730 PULSERAD, TITANIUM

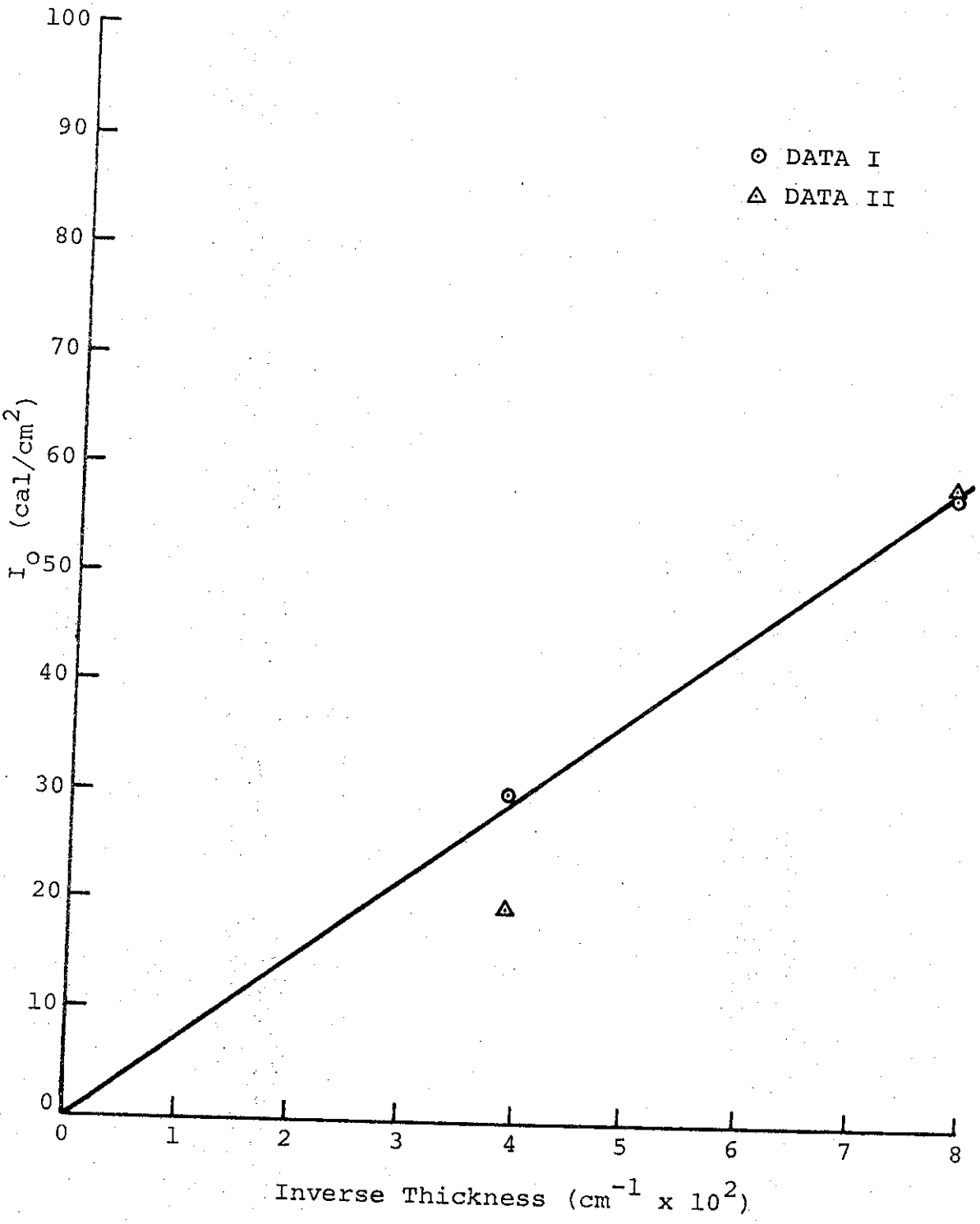

7872

FIGURE 53. I_o VERSUS 1/t AT 3.5 cm, MODEL 730 PULSERAD, TITANIUM

The average current density incident on the foil is calculated from the total calories deposited in the calorimeter by

$$\bar{j} = \frac{\bar{I}}{\pi\sigma_o^{\,2}} = \frac{W}{\bar{E}\ t_p\ \pi\sigma_o'^{\,2}}$$

where W is the total energy expressed in joules, $\bar{E}$ is the mean energy, t_p is the pulse length, and σ_o' is the standard deviation of the beam at the position of the foil. For a total energy of 180 cal, which corresponds to Shot 9659 in configuration I with no foil and for a pulse length t_p of 60 nsec we have,

$$\bar{j} = \frac{760}{10^6 \times 6 \times 10^{-8} \times 3.14 \times 0.2}$$

$$\bar{j} = 20.2\ \text{kA/cm}^2$$

Similarly, for Shot 9686 in configuration II with no foil we have,

$$\bar{j} = \frac{800}{10^6 \times 6 \times 10^{-8} \times 3.14 \times 0.2}$$

$$\bar{j} = 21.2\ \text{kA/cm}^2$$

The "skin-depth" was calculated from the standard equation

$$\delta = \left(\frac{T}{\pi\mu\sigma}\right)^{\frac{1}{2}}\ \text{(meters)}$$

where T is the period, μ is the permeability and σ is the conductivity (mhos/meter). With $T = 2t_p$ and for aluminum where $\sigma = 3.72 \times 10^7$ mhos/meter we have,

$$\delta = \frac{1/2 \times 10^{-7}}{4\pi^2 \times 10^{-7} \times 3.72 \times 10^7}$$

$$\delta = 2.84 \times 10^{-5} \text{ m}$$

$$\delta = 1.12 \text{ mil}$$

The "skin-depth" for titanium where $\sigma = 2.22 \times 10^6$ mhos/m similarly is $\delta = 4.68$ mil. Since the scattering foils ranged in thickness from 0.5 mil to 2.7 mil, significant penetration of the fields would be expected in all cases. The conclusions to be drawn from the present experiments are limited, but the suggested anomalies from classical scattering certainly require further detailed study to explore whether the scattering is constrained by magnetic forces or by an entirely different mechanism.

An attempt was made to use the computer code SCATT to predict the scattering, but the large beam wander and ill-defined source point of the electrons made it impossible to get reasonable comparison of experimental and theoretical results. Accurate calculations will be possible when the beam geometry is better defined.

4. Summary and Conclusions

The multiple scattering of high intensity electron beams from the Model 730 and 1140 Pulserad has been measured. Although there was reasonable agreement with theory for some of the low energy data, other data from the Model 730 Pulserad differed significantly, indicating that other interactions such as magnetic forces due to the large current densities may influence the scattering. The high

energy data from the Model 1140 Pulserad experiments also differed from the theory, but the results were uniform and consistent, i.e., the square of the standard deviation varied approximately linearly with the scatterer thickness. Further experiments are needed to determine if, in fact, collective magnetic forces do influence the scattering process.

Analysis of the Model 1140 data indicated that the electron beam, as transmitted through the anode window, has a roughly gaussian core (out to one standard deviation) and that the fluence in the periphery of the beam is only a few percent above that expected for a normal gaussian profile. With increased scatterer thickness a more nearly gaussian profile was achieved. Approximately 75% of the measured deposited energy could be accounted for by summing the volume under the gaussian deposition profile.

The beam shaping experiments gave only qualitative results due to the problem of beam wander and the large natural width. With improvement of the beam much more accurate results will be possible.

C. BEAM SHAPING WITH MAGNETIC FIELDS

1. Introduction

The pulsed, relativistic electron beam produced by a Pulserad has several important characteristics. Generally speaking, the beam, at present, has a total energy typically less than 5000 calories, a circular cross section, and an angular divergence. The latter two properties can be modified by variation of the gas pressure, but the cross section remains circular. In some of the very recent low-energy (1 MeV), ultra-high-current beams, it is possible to modify the cross section by guiding the beam with conducting walls (Reference 5). In the higher-energy ($\approx$ 3 to 4 MeV) beams however, only

moderate success has been achieved to date. In many experiments, the required irradiation area is noncircular, and the beam cross section, as a result, must be varied until the diameter of the beam corresponds roughly to the largest dimension of the target. As a result, a significant part of the beam is not deposited in the target, and the total energy within the beam is used very inefficiently.

The use of external magnetic fields, although more cumbersome to employ than simply changing the gas pressure or moving a conducting surface, offers a possible approach to improving the efficiency of the beams. In particular, it is well known that a circular beam transported through a quadrupole field will be focused in one dimension and defocused in the perpendicular direction, producing an elliptical cross section. If, in turn, the beam is taken through a second quadrupole that is the mirror image of the first field, the beam can be returned to a circular cross section, and if done properly, could be focused into a smaller cross section.

The first transformed beam is extremely attractive, since presumably the ellipticity of the beam could be chosen to match the dimensions of the target. In doing this, the total energy of the beam would be most efficiently used. The double transformed beam, on the other hand, might allow higher fluences to be obtained than those possible by other means, e.g., the magnetic self-pinching technique by properly choosing the gas pressure.

Presented in this section are the results obtained using a magnetic quadrupole focusing system on the electron beam produced by the Model 1140 Pulserad. The program had three major phases: the initial phase developed a computer code capable of calculating both single- and double-quadrupole optics, to be used to design

and carry out the specific experiments that followed. The second and third phases investigated experimentally whether a predictable, distorted beam could be achieved. The second-phase experiments employed a single quadrupole to achieve an elliptical beam, while the third-phase experiments were carried out with an orthogonal double quadrupole system which theoretically should produce the focused circular beam.

During the course of these investigations, some work was done that utilized a solenoid magnet to improve the injection conditions into the single quadrupole system. A description of the solenoid has been presented elsewhere, but the importance of that work to these experiments should be pointed out (Reference 2 and 6).

The code development is briefly outlined in the following section with more detail appearing in Appendix D. The physical construction and calibration procedures are described in Section III, with the experimental results for the single and double quadrupole system presented in Sections IV and V, respectively. Finally, the conclusions drawn from these experiments along with some recommendations for future experiments are discussed in Section VI.

2. Theory

The physics involved in a magnetic quadrupole optical system has been described in many texts (for example, Reference 7). In addition, discussion of a quadrupole system as applied to a pulsed high-current electron beam has been given by Link (Reference 8). In this report, we shall briefly point out some of the essential features of the problem.

Figure 54 is a schematic of a quadrupole magnet. To first approximation, the magnetic field near the center of the magnet

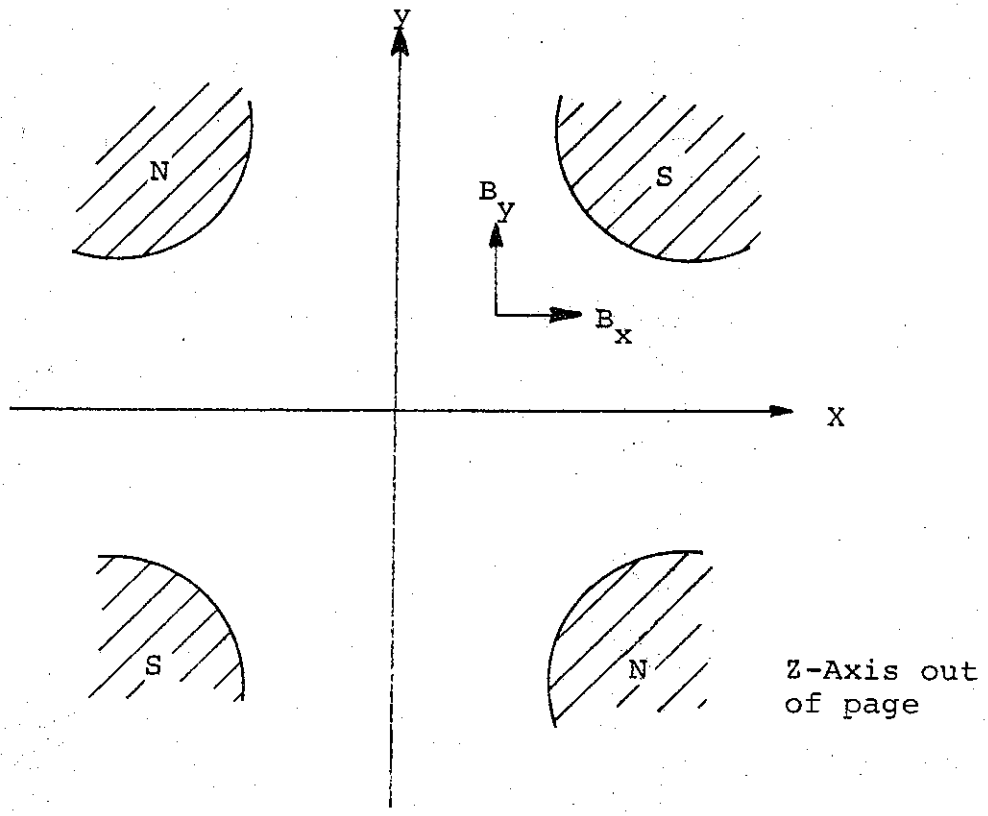

FIGURE 54. SCHEMATIC OF QUADRUPOLE MAGNET

is given by

$$\begin{aligned} B_x &= by \\ B_y &= bx \\ B_z &= 0 \end{aligned} \tag{11}$$

where b is a constant that depends on the current in the windings of the magnet coil, the separation of the pole tips, the pole material and configuration, etc.

If we consider only paraxial rays, we can assume that $v_x = v_y \simeq 0$, $v_z = v$, and we will then have

$$\begin{aligned} F_x &= ev_z B_y \\ F_y &= ev_z B_x \\ F_z &= 0 \end{aligned} \tag{12}$$

or

$$\begin{aligned} F_x &= evbx \\ F_y &= -evby \\ F_z &= 0 \end{aligned} \tag{13}$$

The expressions in Equation (13) indicate that the configuration under consideration will have defocusing in the x-z plane and focusing in the y-z plane.

In the paraxial approximation we have

$$\frac{d}{dt} = v \frac{d}{dz}$$

and

$$\frac{d^2}{dt^2} = v^2 \frac{d^2}{dz^2} \tag{14}$$

From Newton's Second Law, using Equations (13) and (14), the equations of motion for an electron in a magnetic field described by the expressions in Equation (11) become:

$$\frac{d^2x}{dz^2} = \frac{eb}{mv}\,x, \qquad \frac{d^2y}{dz^2} = \frac{eb}{mv}\,y, \tag{15}$$

or

$$\frac{d^2x}{dz^2} = k^2x, \qquad \frac{d^2y}{dz^2} = -k^2y \tag{16}$$

The next question to consider is the variation of the field gradient, b, with axial distance, z. As one moves away from the center of the quadrupole along the z-axis, the field will decrease, eventually falling to zero. However, to a good approximation, the physical quadrupole may be replaced by an idealized quadrupole of constant field gradient, changing discontinuously to zero outside of an effective length, L, the so-called "hard-edge model" (Reference 9).

A good approximation using the hard-edge model (Figure 55) is obtained for L by replacing the B-versus-z curve with a rectangle whose height is equal to B_{max}, and whose area is equal to the area under the B-versus-z curve.

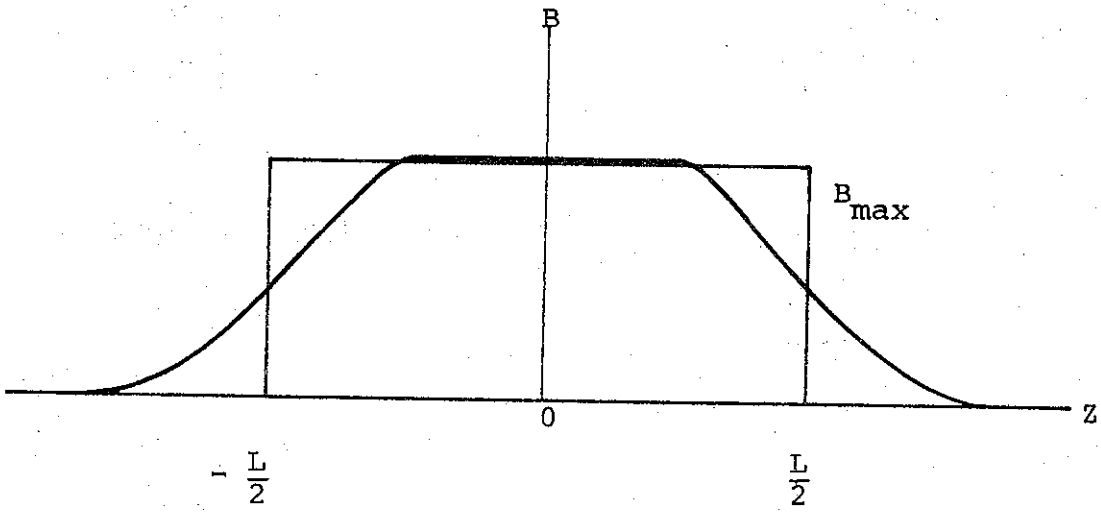

FIGURE 55. HARD-EDGE MODEL OF A QUADRUPOLE MAGNET

The solutions to Equation (16) are straightforward. If we let X_o and X_o' correspond to the coordinate and slope of an electron in the x-z plane at the entrance of the effective field, then at the exit of the field we have

$$X(L) = X_o \cosh(kL) + X_o' \sinh(kL)$$
$$X'(L) = kX_o \sinh(kL) + X_o' \cosh(kL) \tag{17}$$

The corresponding result for the focusing plane is

$$y(L) = y_o \cos(kL) + \frac{y_o'}{k} \sin(kL),$$
$$y(L) = ky_o \sin(kL) + y_o' \cos(kL). \tag{18}$$

A matrix equation can be used to describe the trajectory of an electron in a magnetic focusing system:

$$\begin{pmatrix} x(z) \\ x'(z) \end{pmatrix} = \begin{pmatrix} a & b \\ c & d \end{pmatrix} \begin{pmatrix} x_o \\ x_o' \end{pmatrix} \tag{19}$$

or

$$X(z) = M X_o$$

The quantity M is called the transport matrix for the electron in the x-z plane. We have already derived two transport matrices, one for the focusing plane, M_F, and one for the defocusing plane, M_D, of a quadrupole:

$$M_F(k,L) = \begin{pmatrix} \cos(kL) & (1/k)\sin(kL) \\ -k\sin(kL) & \cos(kL) \end{pmatrix} \tag{20}$$

$$M_D(k,L) = \begin{pmatrix} \cosh(kL) & (1/k)\sinh(kL) \\ k\sinh(kL) & \cosh(kL) \end{pmatrix} \tag{21}$$

To complete the analysis of any magnetic focusing system, a transport matrix for a field free region is needed. It can be easily verified that such a matrix is given by

$$M_{FF}(A) = \begin{pmatrix} 1 & A \\ 0 & 1 \end{pmatrix} \tag{22}$$

where A is the axial distance traveled in the field-free region.

Any quadrupole system can be described by a combination of the three transport matrices. For example, a system composed of a field-free region of length A, a focusing quad of strength k_1 and length L_1, a field-free region of length B, and defocusing quad of strength k_2 and length L_2, plus a field-free region where D as the focus point is given by

$$X(D) = M_{FF}(D)M_D(k_2,L_2)M_{FF}(B)M_F(k_1,L_1)M_{FF}(A)\ X_o,$$

where the normal rules for matrix multiplication apply. In this case the particle starts in the field-free region. The quadrupole code we developed utilizes this approach to the problem. Appendix D describes the use of the code and explains interpretation of the output.

3. Quadrupole Construction and Calibration

Two identical quadrupoles were constructed for this program. The quads, which are electrically powered and are water cooled, were designed to ride on a rail that was suspended from the top of the Model 1140 Pulserad drift chamber. The coil windings, complete with cooling coils, were supplied by Research Magnetic Systems, Inc., while the magnet pole tips, and the magnet housing were constructed by Physics International. Figure 56 is a photograph of an assembled quadrupole.

A plot of the B_y field versus distance from magnet center along the horizontal x axis appears in Figure 57. For a magnet current, I, equal to 10 A, a field gradient, b, equal to 150 G/cm is obtained. Note that the assumption of a constant, b, holds only out to 3 cm from the z axis.

Assuming the magnets do not saturate, an assumption verified in the magnet-current range from 1 to 10 A (see Figures 7 and 8), implies that the field gradient, b, is linearly dependent on the magnet current (Figure 58).

To obtain the effective field length, L, for the quadrupoles a plot of B-field versus distance from magnet center along the z axis was made for different magnet currents and for different radial positions. Figures 59 and 60 illustrate the field variation for 10 A and 3 A, respectively. From both figures we have obtained an effective field length of approximately 11.0 cm.

4. Beam Shaping with Single Quadrupole

Consider a single quadrupole whose pole configuration is shown in Figure 51. This system will focus a beam in the y-z plane and defocus in the x-z plane.

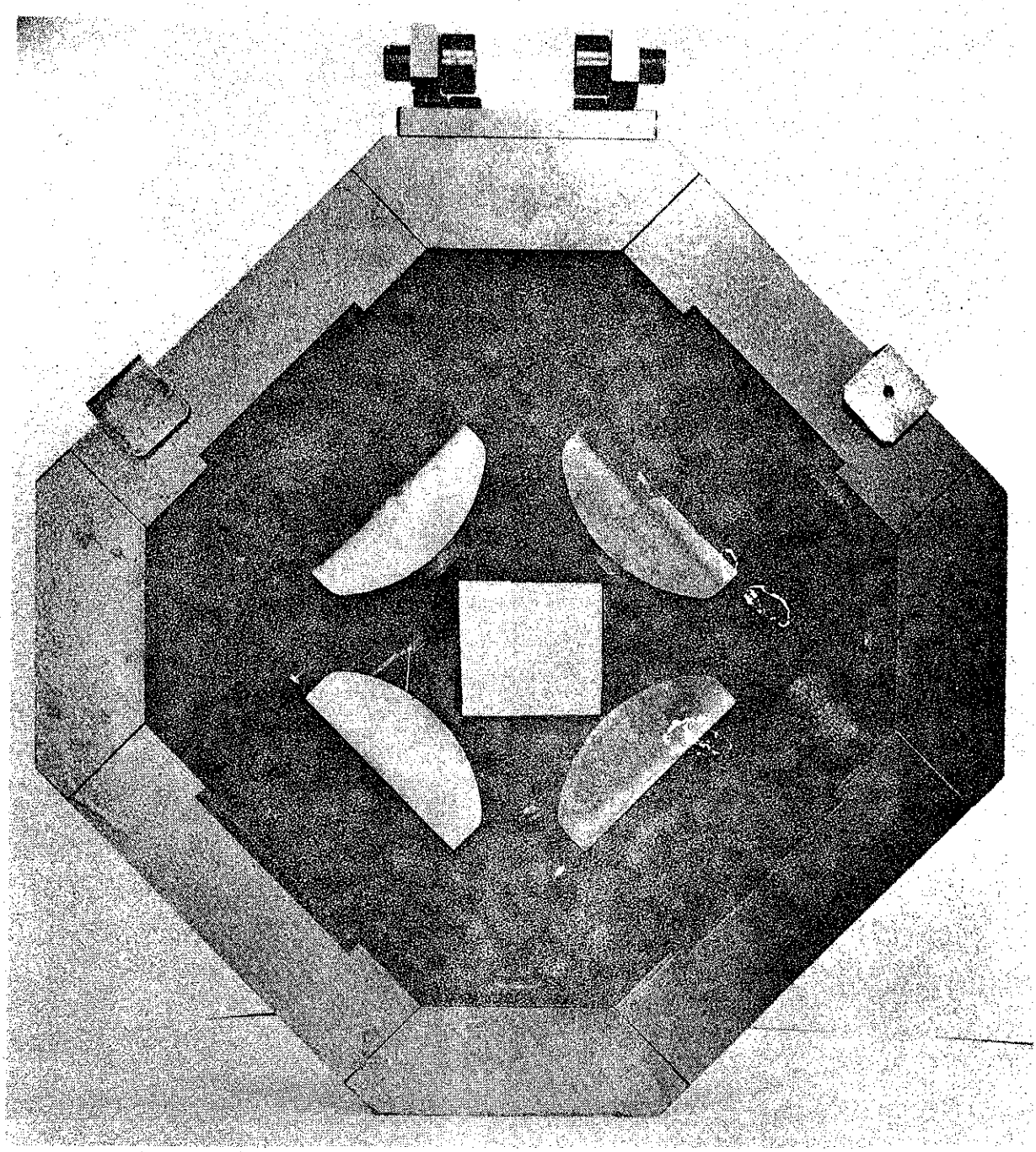

FIGURE 56. ASSEMBLED QUADRUPOLE

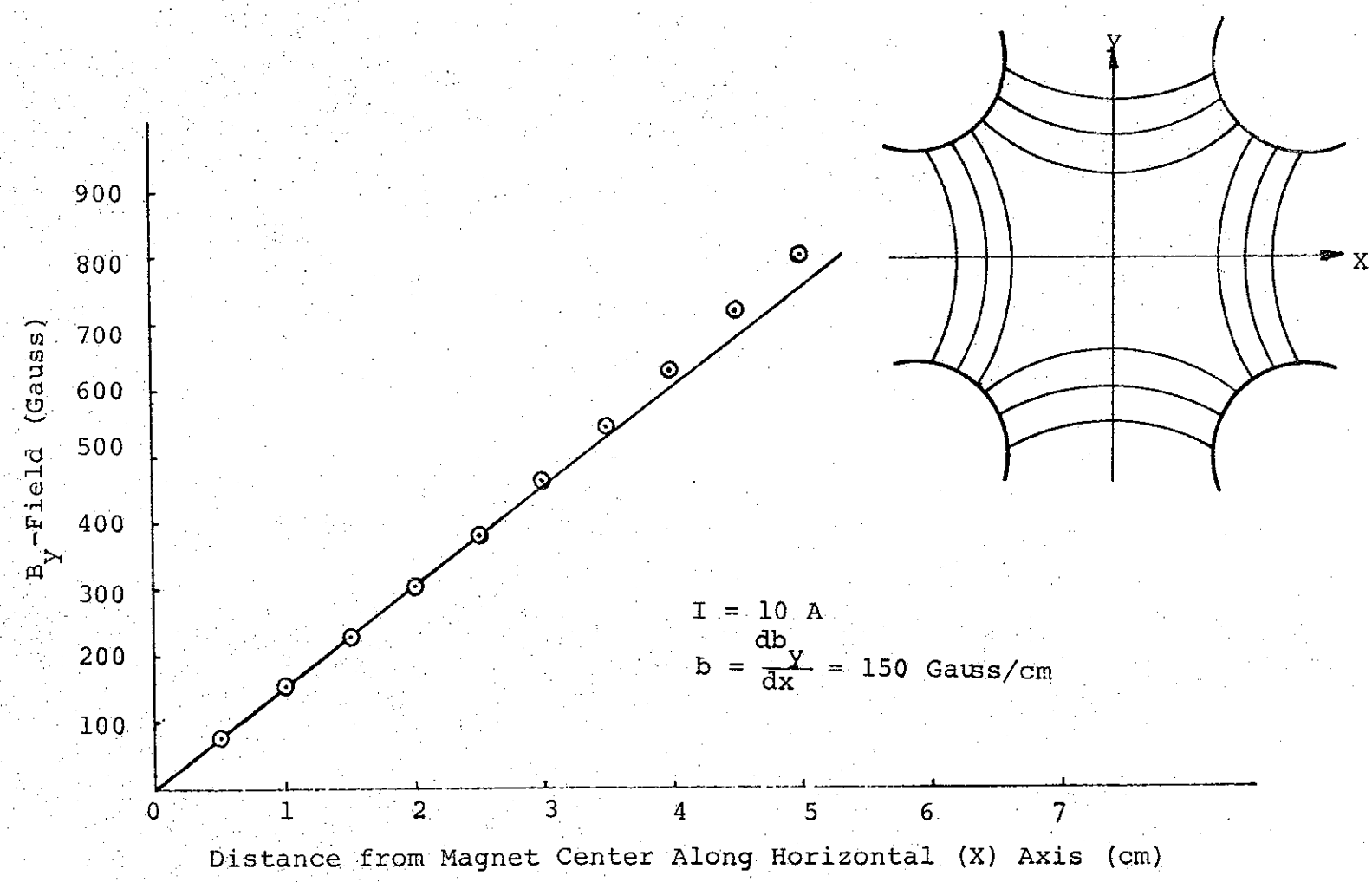

FIGURE 57. QUADRUPOLE FIELD GRADIENT AT 10 A

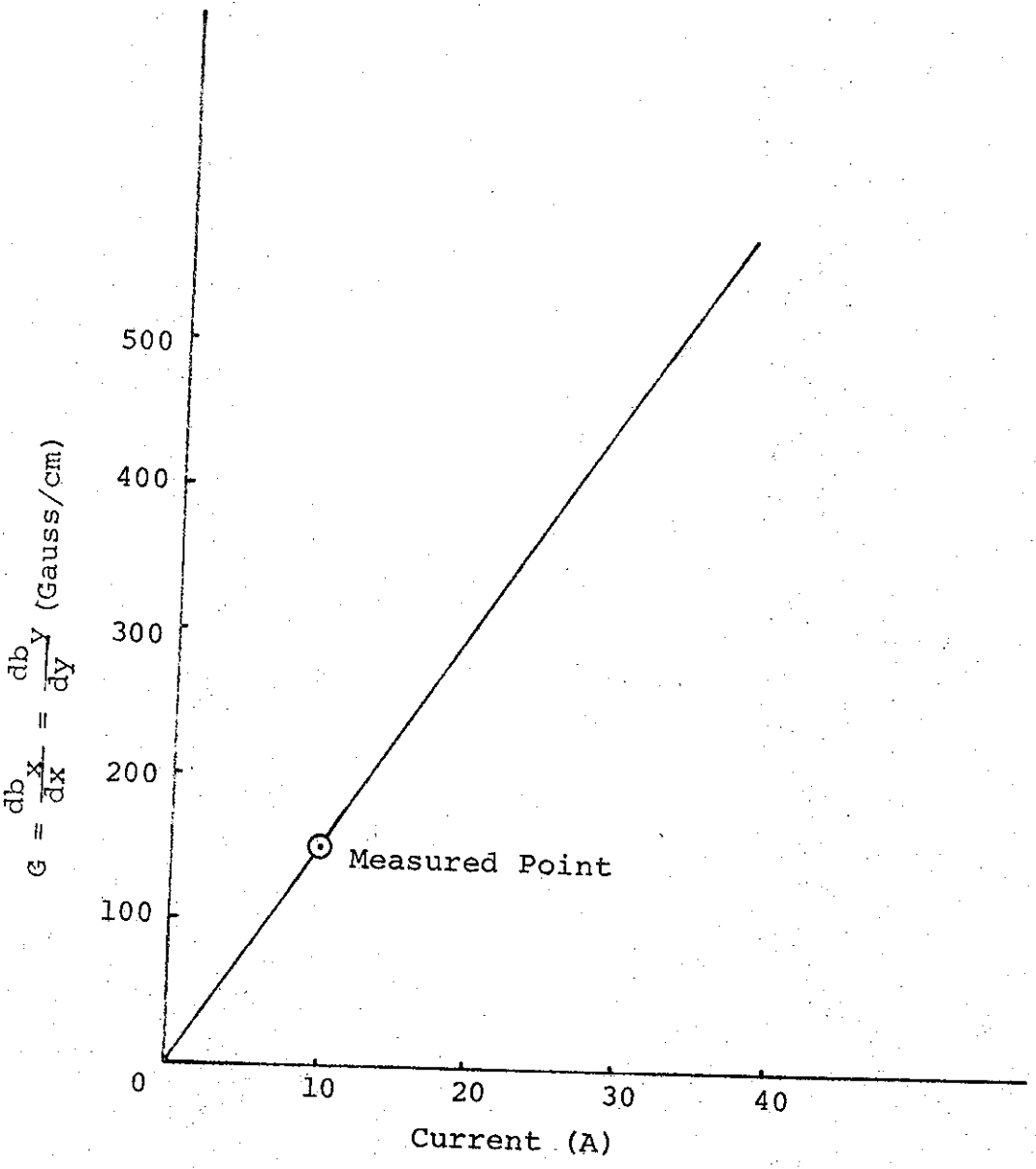

FIGURE 58. PROBABLE FIELD GRADIENT FOR QUADRUPOLES

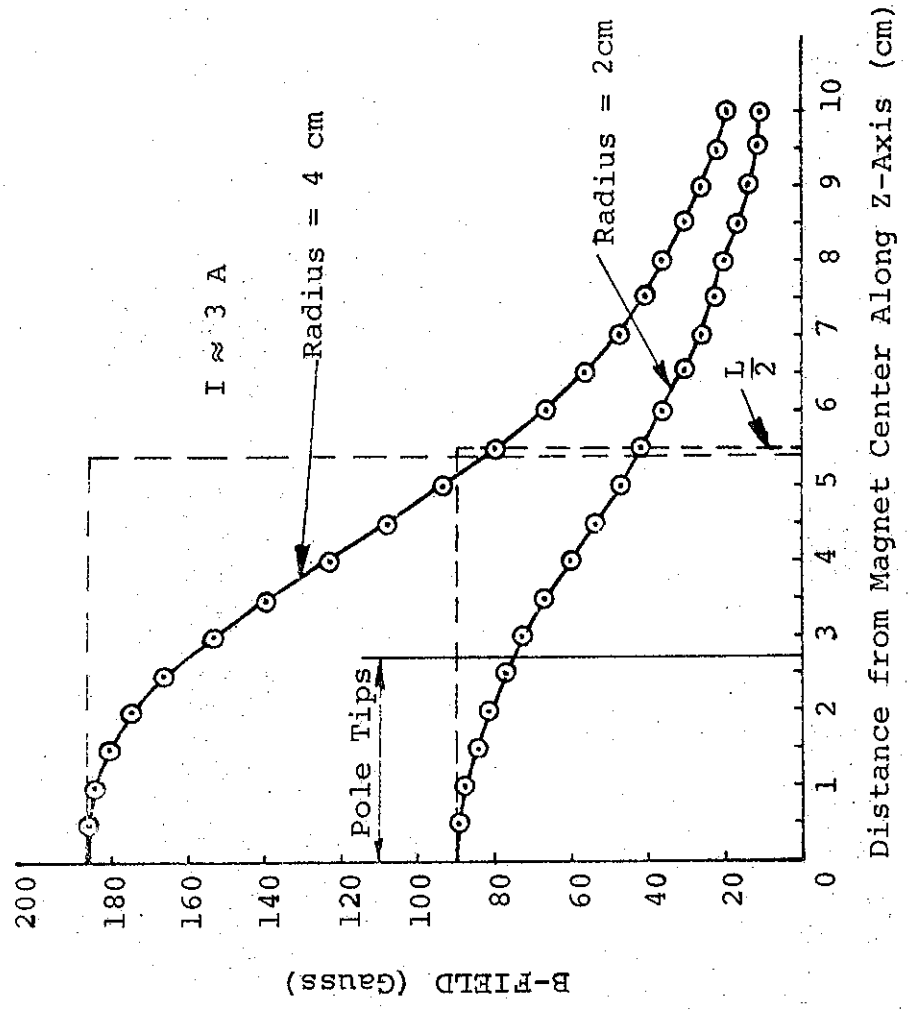

FIGURE 59. DETERMINATION OF THE EFFECTIVE FIELD LENGTH FOR A CURRENT OF 3 A

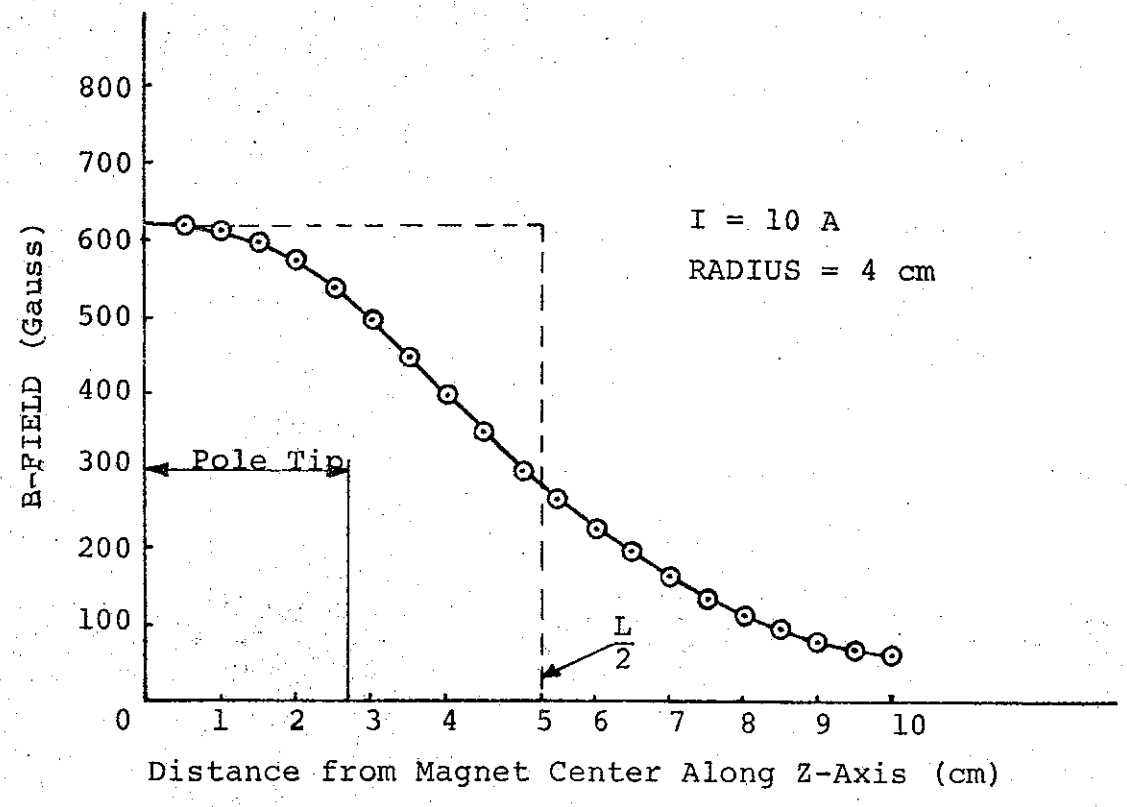

FIGURE 60. DETERMINATION OF THE EFFECTIVE FIELD LENGTH FOR A CURRENT OF 10 A

A ray diagram for a single quadrupole optical system is shown in Figure 61. In the figure, and in the analysis below, f_F is the point at which a ray crosses the z axis in the zx focusing plane measured with respect to the edge of the effective field; f_D is the corresponding point in the zy defocusing plane; and A is the radial distance of an arbitrary ray parallel to the z axis. If a calorimeter is located at z, where $o < z < f_F$, we have

$$\frac{x}{z-f_D} = \frac{A}{-f_D} ,$$

$$\frac{y}{f_F-z} = \frac{A}{f_F}$$

Thus we have an ellipse whose eccentricity ε (= x/y) is given by

$$\varepsilon = \frac{1 - z/f_D}{1 - z/f_F} \qquad \text{Case 1:} \quad f_D < 0,\ 0 < z < f_F$$

Similar analysis yields the following results:

$$\varepsilon = \frac{1 - z/f_D}{z/f_F - 1} \qquad \text{Case 2:} \quad f_D < 0,\ 0 < f_F < z$$

$$\varepsilon = \frac{z/f_D - 1}{z/f_F - 1} \qquad \text{Case 3:} \quad f_D < 0,\ f_F < 0,\ z > 0$$

The preceding equations simply predict how a parallel beam of monoenergetic electrons with a circular cross section can be transformed into a beam with a line cross section at the point $z = f_F$.

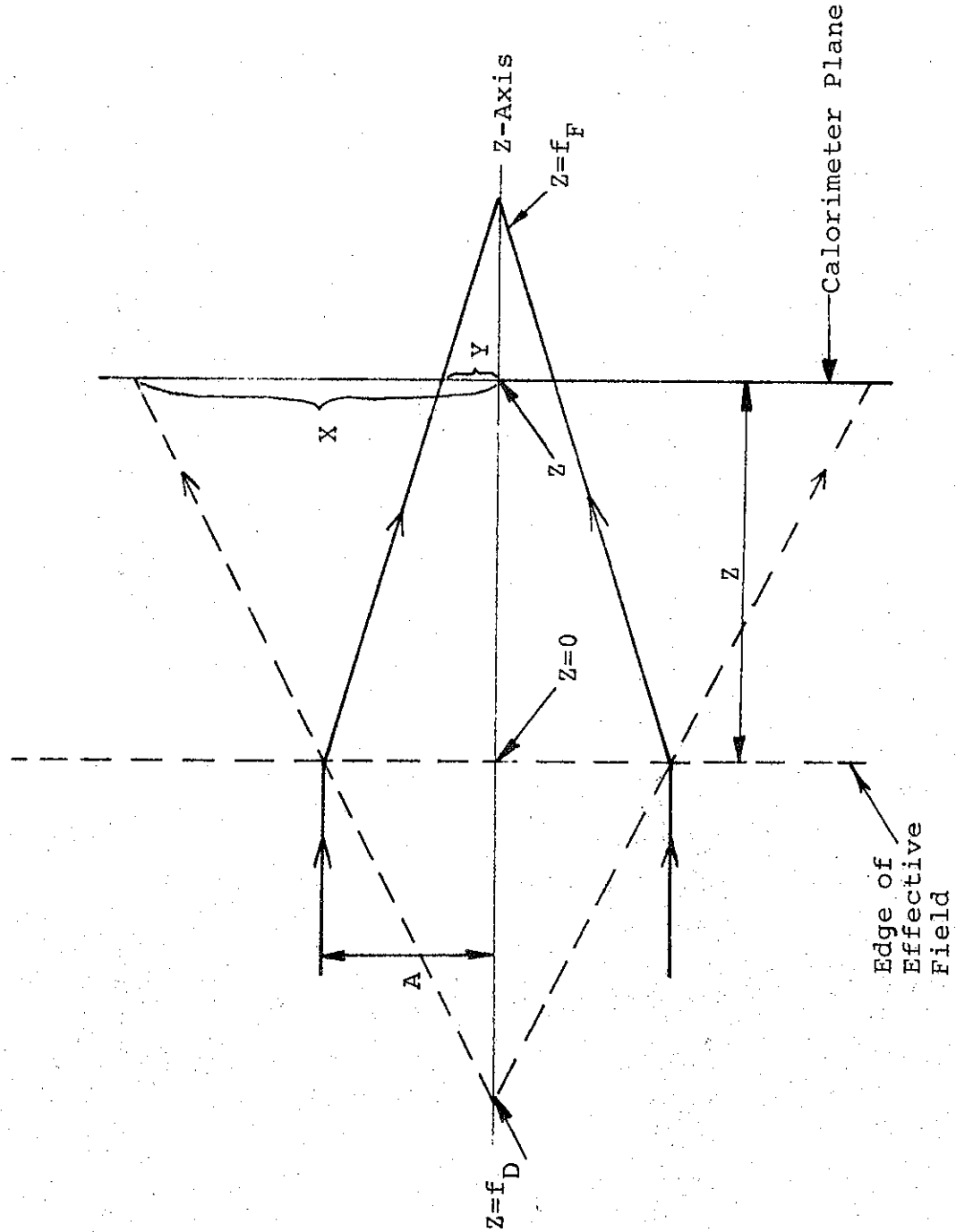

FIGURE 61. SINGLE QUADRUPOLE OPTICS

The beam from the Model 1140 Pulserad, however, is generally neither monoenergetic nor paraxial. We are therefore faced with the problems of "chromatic" aberration, that is, electrons of different energies coming to a focus at different points on the z axis, and uncertainties in the effective object distance and the resultant lack of a definite focal point. The problem of reproducibly injecting the beam into the quadrupole on axis should also be mentioned. Because of these difficulties, an initial estimate of an 8:1 ratio of major to minor axes was made. Such a ratio would still be attractive for many practical tests. In a brief preliminary study, a ratio of 2.5:1 was obtained on the Model 730 Pulserad, using a crudely constructed quadrupole with permanent magnets (Reference 10).

A schematic of the geometry used for these experiments appears in Figure 62. A needle cathode was used that consisted of two concentric circles with 18 needles in each circle. The anode was a titanium foil, 0.002 in. thick. A pulsed solenoid (Reference 2 presents further details on this solenoid) was used on each shot to improve the injection reproducibility of the beam. The beam was detected with a conventional 5 x 5 calorimeter array composed of graphite blocks, 2 in. x 2 in. x 1/2 in.

To experimentally determine the eccentricity of the beam at the calorimeter plane, we considered only the five calorimeter blocks on a horizontal line through the center of the calorimeter, and the five blocks on a vertical line through the center. The total calories deposited in each block provides an energy distribution for the beam on the horizontal and vertical cuts. We denote by x_i the position of the blocks on the horizontal cut, with x_i taking on the values -4, -2, 0, 2, and 4. Similarly, y_i denotes

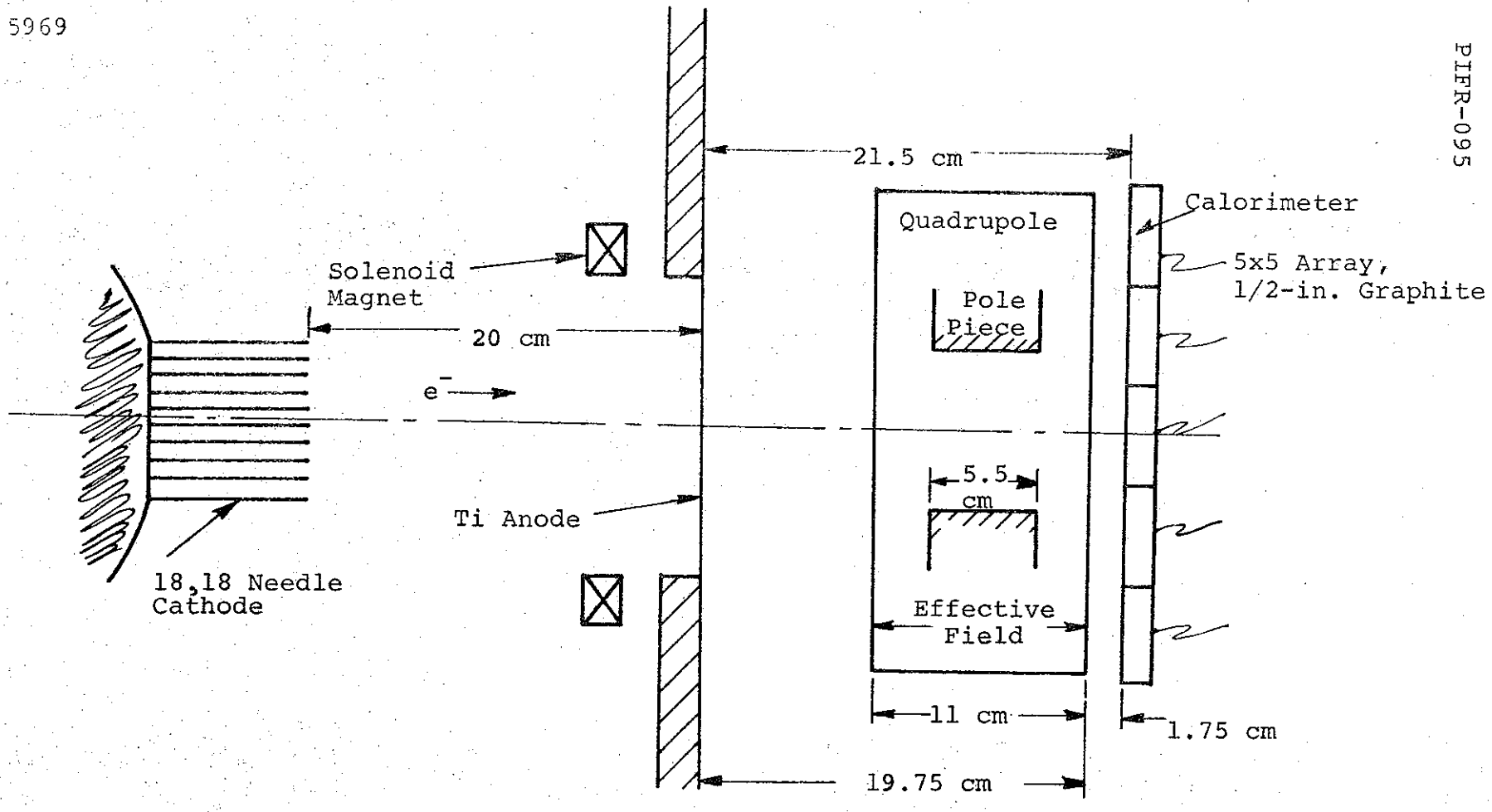

FIGURE 62. SCHEMATIC OF EXPERIMENTAL GEOMETRY USED FOR BEAM-SHAPING EXPERIMENT

the position of the blocks on the vertical cut. If $f(x_i)$ and $f(y_i)$ are the calories deposited in blocks x_i and y_i, then the mean of each distribution is given by

$$\bar{x} = \frac{1}{\alpha} \sum_{i=i}^{5} x_1 \, f(x_i)$$

and

$$\bar{y} = \frac{1}{\beta} \sum_{i=i}^{5} y_i \, f(y_i)$$

where

$$\alpha = \sum_{i=i}^{5} f(x_i)$$

and

$$\beta = \sum_{i=i}^{5} f(y_i)$$

The dispersion, σ^{2*}, for each distribution is given by

$$\sigma_x^2 = \frac{1}{\alpha} \sum_{i=i}^{5} (x_i - \bar{x})^2 \, f(x_i)$$

or by

$$\sigma_x^2 = \bar{x}^2 - \bar{x}^2$$

with a similar expression for σ_y^2. We now define the eccentricity of the distribution, ε, as

$$\varepsilon = \frac{\sigma_y}{\sigma_x} \quad \text{if} \quad \sigma_x > \sigma_y$$

*For a gaussian distribution, $I = I_o \exp(-x^2/2\sigma^2)$, $x = \pm \sigma$ is the point for which $I = 0.606 \, I_o$.

or as

$$\varepsilon = \frac{\sigma_x}{\sigma_y} \quad \text{if} \quad \sigma_y > \sigma_x$$

The results of the experiment are summarized in Table VII. It appears that the initial prediction of $\varepsilon = 8$ was nearly realized by the experiment. Because the energy deposited in the calorimeter generally fell or nearly fell to zero on the wings of the vertical cut, but did not do so on the horizontal cut, the tabulated values should be regarded as lower limits.

Calculations of the eccentricity as a function of field gradient have been made for a calorimeter distance, z, of 1.75 cm, assuming a beam energy, E, of 3.75 MeV and an object distance, ϕ, of 20 cm.

The results of this experiment are plotted in Figure 63 along with the results of the experiment at z = 1.75 cm. It would appear that the two results are not inconsistent. Figure 64 contains plots of the same quantities for the experiment at z = 5.25 cm. In this case, with E = 3.75 MeV, and an object distance of ϕ = 5.0 cm, the results show a fair fit of theory to experiment. Increasing the energy and/or decreasing the object distance will raise the calculated curve and improve the agreement.

Exactly why two different object distances are required to describe the two experiments is unclear. The experimental situation, as previously mentioned, is quite different from a monoenergetic beam with a well defined object distance. It may well be that a certain combination of effective beam energy and effective object distance exists that is capable of describing these experiments,

TABLE VII

RESULTS OF BEAM SHAPING EXPERIMENT*

Shot No.	Quadrupole Field Gradient (G/cm)	I (A)	Beam Eccentricity (ε)
3328	0	0	1.03
3329	0	0	1.13
3330	150	10	2.02
3331	150	10	1.94
3332	225	15	2.65
3333	225	15	2.55
3334	300	20	6.45
3335	300	20	5.65
3348**	450	30	2.39
3349**	450	30	2.65

*Solenoid capacitor-bank charging voltage was 8.0 kV on all shots

**Effective field-calorimeter separation was 5.25 cm, as opposed to 1.75 cm on other shots

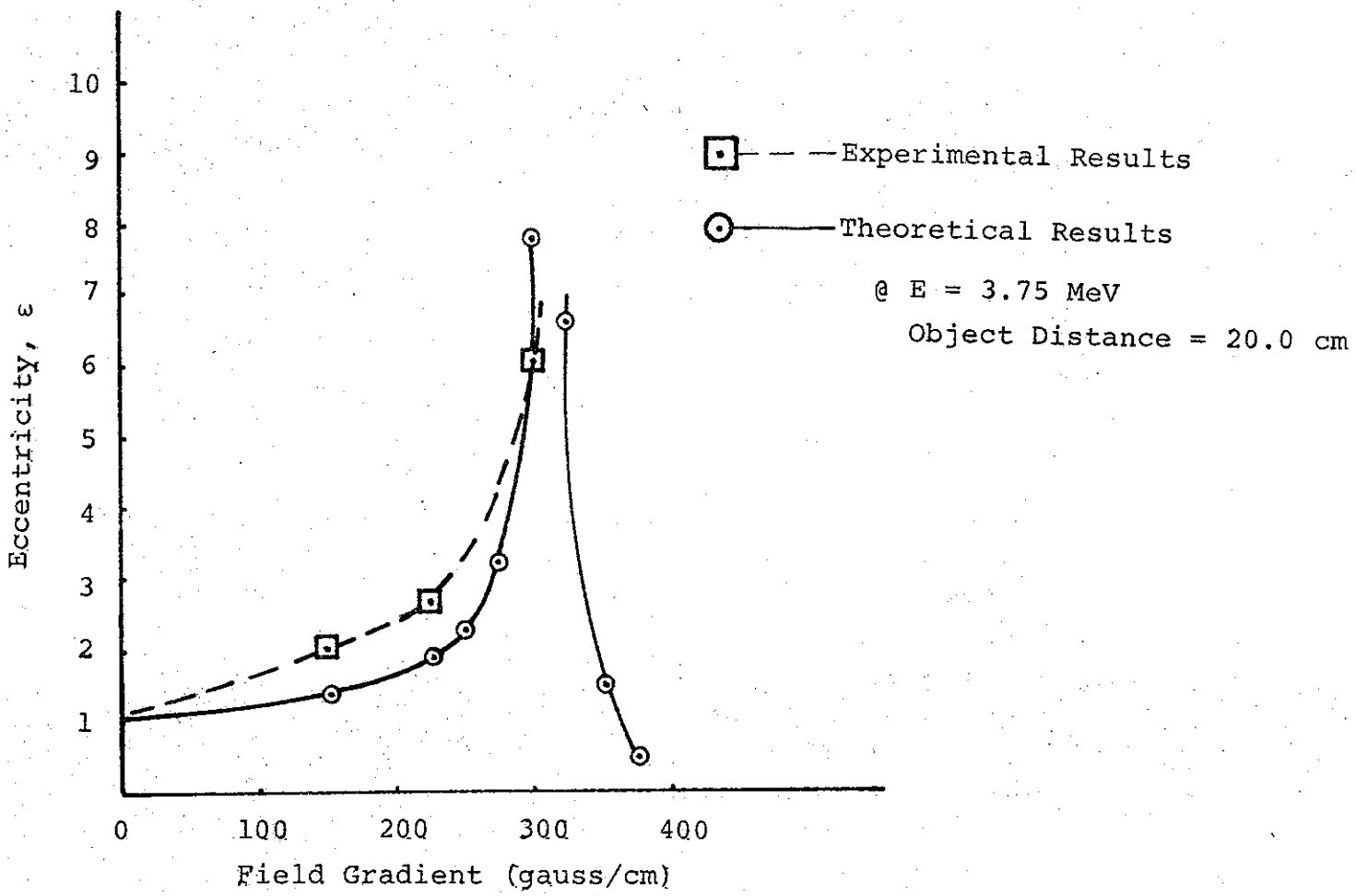

FIGURE 63. BEAM ECCENTRICITY AT CALORIMETER VERSUS QUADRUPOLE FIELD GRADIENT FOR Z = 1.75 cm

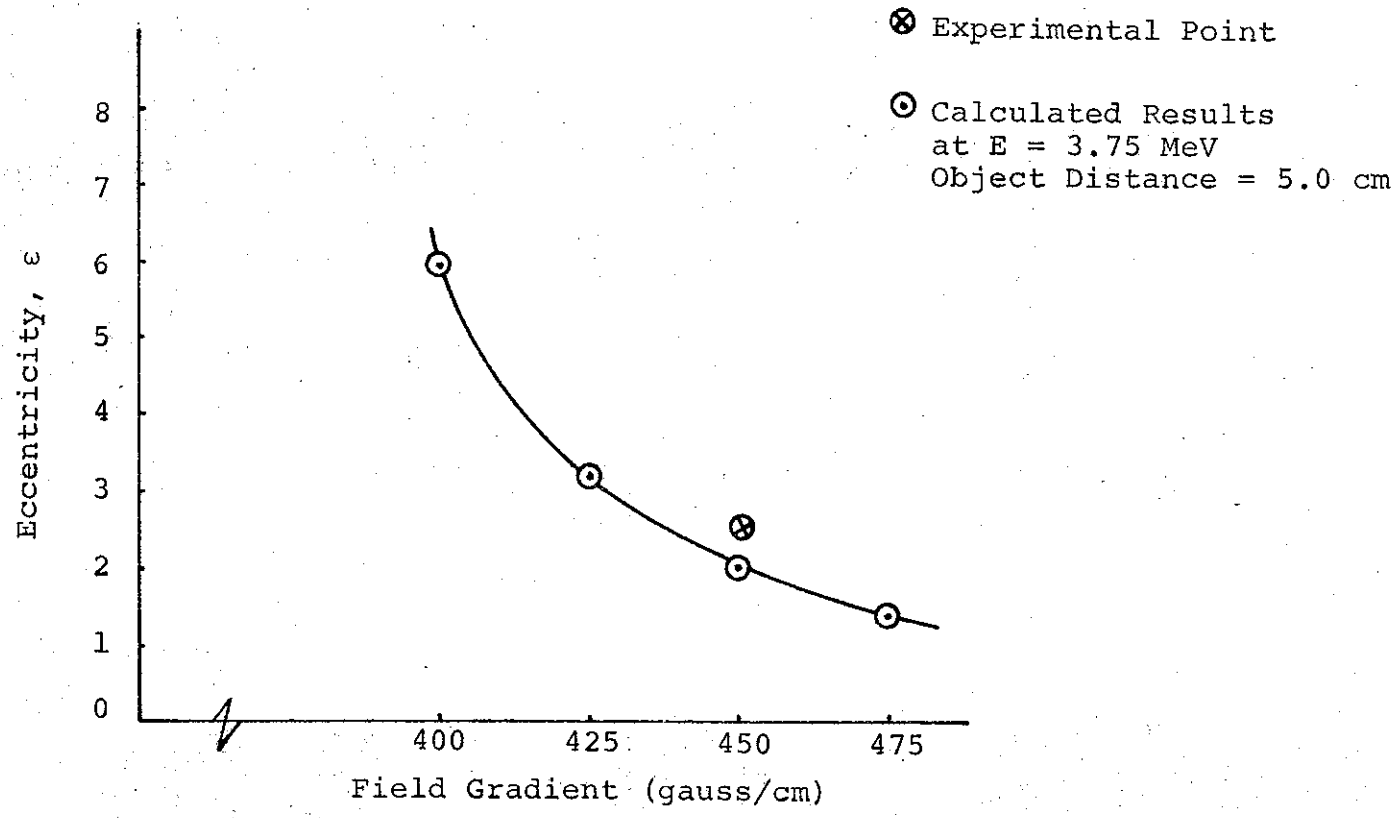

FIGURE 64. BEAM ECCENTRICITY AT CALORIMETER VERSUS QUADRUPOLE FIELD GRADIENT FOR Z = 5.25 cm

but it would require a trial-and-error method to find such a combination. The practical value of such a search is limited, and for that reason has not been pursued.

5. Beam Focusing with Double Quad

The double quadrupole, or "doublet", is the simplest configuration that will give focusing in both the x and y components. The quads have opposite polarity, so that if the effect on the trajectories in the x-z plane is to focus and then defocus, the effect in the y-z plane would be to defocus and then focus.

A ray diagram for a double-quadrupole optical system appears in Figure 65. For this system, the coordinates are referenced to the edge of the effective field of the second quadrupole and the values of x and y are the deflections resulting from defocusing and focusing, respectively, in the first quad. f_{Df} is the point at which a ray in the focusing plane of the second quad crosses the z axis, and f_{fD} is the corresponding point in the defocusing plane. Thus, for the configuration of Figure 65, in which $0 < z' < f_{Df}$ we have

$$\frac{x}{f_{Df}} = \frac{x'}{f_{Df} - z'}$$

$$\frac{y}{f_{fD}} \quad \frac{y'}{f_{fD} - z'}$$

If the values of x and y from Equations (12) and (13) of Section IV (corresponding to $0 < z < f_f$ when z is the location of the effective edge of the second quad field [$z' = 0$]) substituted, and the results are used to calculate the eccentricity of the focused beam in the plane of the calorimeter array,

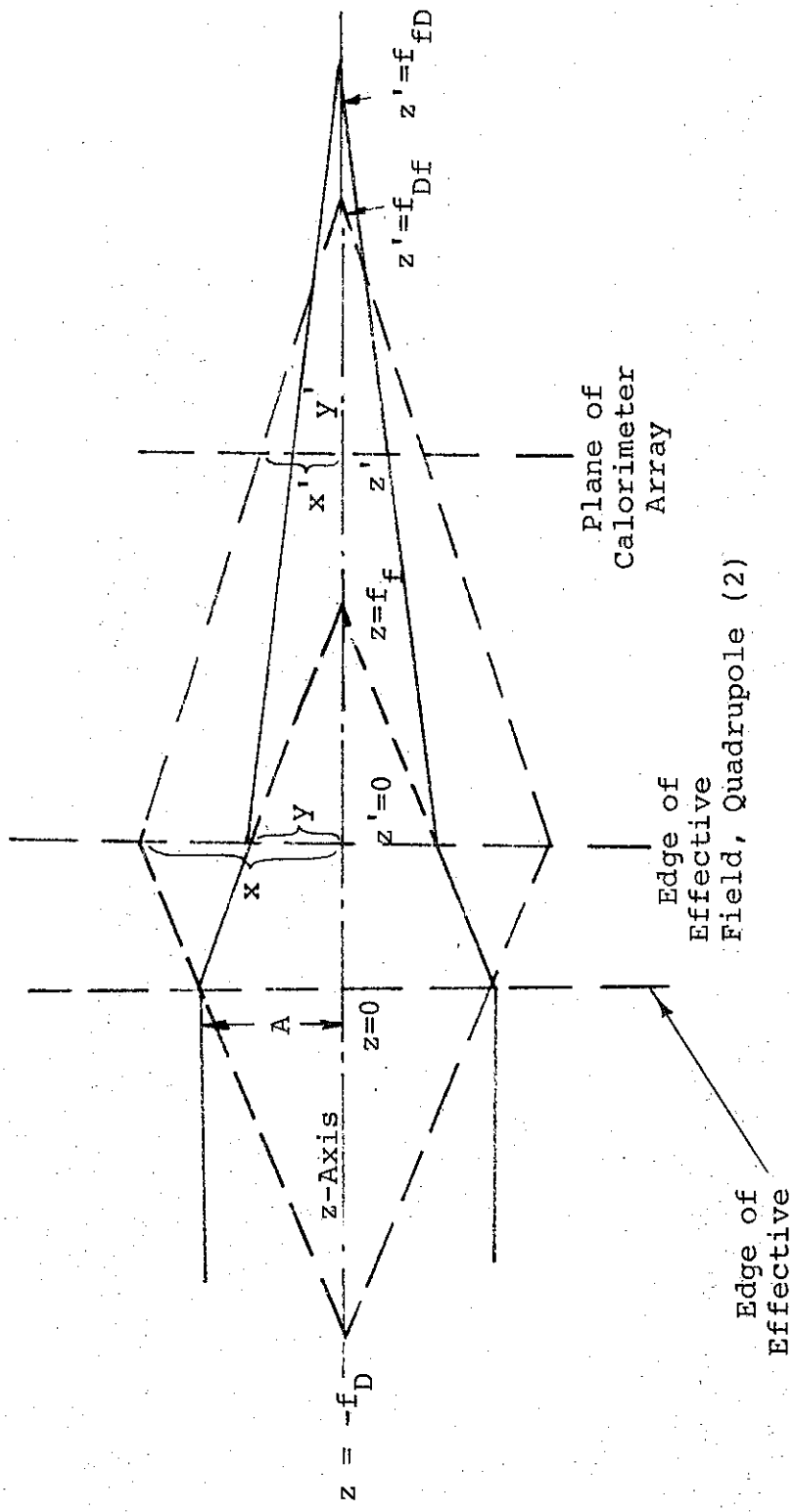

FIGURE 65. DOUBLE QUADRUPOLE OPTICS

then

$$\varepsilon = \frac{x'}{y'} = \frac{(1 - z/f_D)(1 - z'/f_{Df})}{(1 - z/f_f)(1 - z'/f_{fD})}$$

Note that the quantities in this equation must be measured with respect to the appropriate coordinate system. The conditions necessary to achieve a circular beam cross section are obtained by $\varepsilon = 1$,

$$\frac{(1 - z/f_D)}{(1 - z/f_f)} = \frac{(1 - z'/f_{fD})}{(1 - z'/f_{Df})}$$

Analogous calculations for different configurations of the two quadrupoles will give other conditions under which a circular beam cross section might be achieved. Since only small deflections in the quadrupole field are involved, a condition that can be imposed on the variables in the above equation to achieve a focus is $f_{fD} = f_{Df}$. The separation of the effective fields, z, for a given electron energy, determines the magnet current for the required focus. The area of the circular beam cross section is determined by the position of the target with respect to the focus.

In the experiments using the double-quad system, the field gradients in the quads were not in the optimum ratio to achieve a focus consistent with other experimental parameters, so confirmation of the maximum focusing properties was not possible. The highly uniform elliptical beam cross section and high eccentricity achieved with the single quad indicates that with the proper conditions in the second quad, a focus could be achieved.

In evaluating this technique as a means of achieving beam focusing, several difficulties should be mentioned. First, the

technique is extremely sensitive to beam conditions. Any variation in effective object distance, mean energy, or radial beam wander degrades the focusing quality quite rapidly. Table VIII shows the results of a code calculation (for the set of magnet geometry conditions where most of the unsuccessful experiments were performed) concerning how rapidly the beam parameters can influence the optimum focusing plane.

Secondly, the practical implementation of the technique is quite complex. The quality of beam focusing is sensitive to misalignments between beam axis and quadrupole axis, and thus requires that very careful alignment procedures be followed. In contrast, experiments recently completed using a conducting pipe to guide a pinched circular beam have shown promising results. Table IX is a tabulation of the total calories, peak fluence, and beam radius (FWHM) obtained for a series of typical shots using this technique.* It should be noted that the interaction of the beam with the walls is not strong enough in a so-called drifting mode to obtain an elliptical beam, so the single quadrupole focusing is still the only technique at present that provides an elongated beam.

6. Conclusions

The attempts to shape the electron beam from the Model 1140 Pulserad with a quadrupole magnet have been partially successful. With a single quadrupole and pulsed solenoid magnets, we have demonstrated an ability to control the eccentricity of the beam, at least up to a factor of $\varepsilon \approx 8$, by varying the quadrupole field gradient. A highly uniform elliptical beam cross section was achieved. Accurate measurements for high eccentricities were limited only by the lack of resolution of the calorimetry as a

*This technique was explored by Dr. P. Spence as part of a PI-funded beam program.

TABLE VIII

VARIATION OF FOCUSING PLANE
AS A FUNCTION OF BEAM AND QUADRUPOLE PARAMETERS
(Separation between quadrupoles = 2.5 cm,
effective length of field = 11.0 cm.)

Field Gradient:	QUAD 1 QUAD 2	150 225	225 225	G/cm 175 350
Energy (MeV)	Object Dist. (cm)			
3.2	5	-8.48 6.00	-12.77 6.79	-6.44 = f_{fD} (cm) 1.44 = f_{Df} (cm)
	10	-10.02 5.74	-5.13 6.62	-7.35 = f_{fD} (cm) 1.33 = f_{Df} (cm)
	20	-0.12 5.50	-6.47 6.47	-4.54 = f_{fD} (cm) 1.24 = f_{Df} (cm)
3.5	5	-8.78 6.91	-11.48 7.81	-6.66 = f_{fD} (cm) 1.91 = f_{Df} (cm)
	10	-10.08 6.59	-4.03 7.59	-7.36 = f_{fD} (cm) 1.79 = f_{Df} (cm)
	20	16.76 6.29	-6.40 7.39	-3.30 = f_{fD} (cm) 1.68 = f_{Df} (cm)
3.8	5	-9.17 -7.86	-11.11 8.87	-6.88 = f_{fD} (cm) 2.39 = f_{Df} (cm)
	10	-10.24 7.47	-1.66 8.60	-7.48 = f_{fD} (cm) 2.25 = f_{Df} (cm)
	20	-47.40 7.11	-6.25 8.35	+2.34 = f_{fD} (cm) 2.12 = f_{Df} (cm)

Experimental Configuration

Optimum Configuration

TABLE IX

BEAM FOCUSING USING A CONDUCTING CONE TECHNIQUE

Cone No. 1 Parameters	Cone Length = 39 in. 4-in. entrance aperture 1-3/4-in. exit aperture
Cone No. 2 Parameters	Cone Length = 47 in. 4-in. entrance aperture 3/4-in. exit aperture

Shot No.	Drift Chamber Pressure (Torr)	Cone No.	Total Energy (cal)	Peak Fluence (cal/cm^2)
4407	200	1	294	66
4408	150	1	1193	401
4409	200	1	232	45
4410	100	1	978	275
4432	150	1	552	151
4424	150	2	206	98
4425	150	2	191	89
4426	100	2	469	179
4427	100	2	250	85

result of steep fluence gradients and by the fact that the major axis of the ellipse extended beyond the edges of the array. No simple model of the beam could be used as input to the computer code to predict the effect of the quadrupoles for all experimental configurations, but for a given configuration the calculation agreed reasonably well with the experiment.

Experiments with the double-quadrupole system were unsuccessful due to a poor choice of field gradients and experimental geometry, but the results with the single quadrupole indicate that the linear transformation through a second quad should result in a highly focused beam. Other work, however, has indicated that highly focused beams may be achieved by injecting the beam through a solenoid magnet mounted in the anode-cathode region, so the major use of the quadrupole system may be in transporting and shaping the beam.

REFERENCES

1. Stainless Steel Handbook, Allegheny Ludlum Steel Corp., Pittsburgh, Pennsylvania (1959), p. 2.

2. D. Wood, "Pulsed Solenoid Magnet on 1140 Pulserad, "PIIR-37-68, International Company, San Leandro, California, (1968).

3. W. Scott, "The Theory of Small-Angle Multiple Scattering of Fast Charged Particles," Rev. Mod Phys. 35, 231 (1963).

4. Alpha-, Beta-, and Gamma-Ray Spectroscopy, (Seigbann, North Holland Publishing Co. (1965) Vol. I.

5. G. Yonas and P. Spence, "Experimental Investigation of High ν/γ Electron Beam Transport," PIFR-106, Physics International Company, San Leandro, California, (1968).

6. D. Wood, "Electron Beam Reproducibility Study," PIIR-11-68, Physics International Company, San Leandro, California (1968).

7. E. Segre, Nuclei and Particles (W. A. Benjamin, Inc., New York 1965) p. 145-48.

8. W. T. Link, "Shaping Electron Beams with Quadrupole Magnets," PIIR-26-67, Physics International Company, San Leandro, California (1967).

9. K. G. Steffen, High Energy Beam Optics, (Interscience, New York, 1965), p. 11.

10. L. Hatch, "Beam Shaping Measurements on the 730 Pulser Facility," PIIR-30-67, Physics International Company, San Leandro, California.

APPENDIX A

CONSTRUCTION AND CALIBRATION DETAILS FOR THE MAGNETIC SPECTRUM ANALYZER (MSA)

SECTION I

INTRODUCTION

This appendix summarizes the development of a magnetic spectrum analyzer (MSA), designed for operation on various electron beam generators (pulsers) produced and operated by Physics International. The MSA was conceived as a device that would measure directly the spectral characteristics of the electron beams generated by the pulsers. Successful operation of the MSA in conjunction with depth-dose measurements and with current and voltage measurements, could lead to a technique for determining the electron beam deposition profile on each shot that does not perturb the beam.

SECTION II

APPARATUS

The essential elements of the MSA are the magnet itself, a vacuum chamber and collimating system, and a detector array.

A. THE MAGNET

The magnet is powered by a Harrison Laboratories Model 6516A dc power supply. Operation is generally restricted to a linear portion of the curve that plots maximum magnetic field in the magnet as a function of current in the magnet coils (B_{max} versus I_m). This linear portion is typically between 2.0 and 7.0 A, corresponding to 290 and 990 G, respectively. Figure A-1 is a plot of B_{max} versus I_m for this region.

A schematic top-view of the magnet pole tips and a photograph of the entire magnet are shown in Figure A-2. The pole tips are soft iron and have a 1-in. separation.

B. THE VACUUM CHAMBER

A portion of the vacuum chamber fits between the magnet pole tips. The collimating region and the region containing the detectors are also part of the vacuum chamber. The collimator is shielded magnetically using concentric cylinders of mu-metal foils. A schematic and a photograph of the collimator are shown in Figure A-3. The mu-metal foils and the adjustable rectangular slit are clearly shown in the photograph.

The electron beam is collimated using (1) a circular aperture that is 1.9 cm in diameter and (2) an adjustable rectangular slit, 0.5 cm by 0.5 cm maximum width. The slits are separated by 11.0 cm.

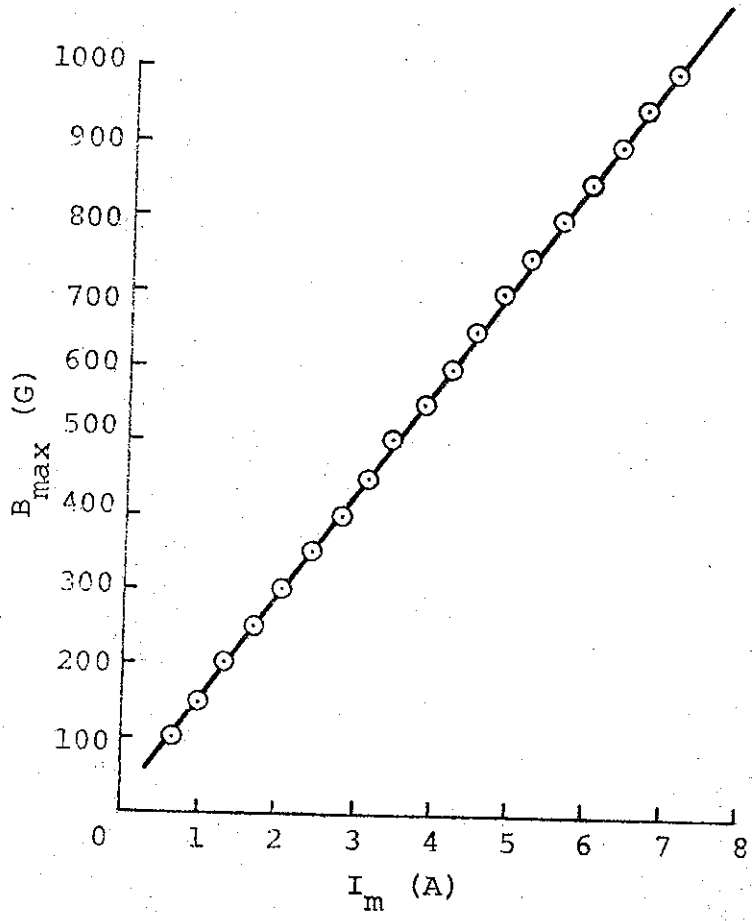

FIGURE A-1. MAXIMUM MAGNETIC FIELD IN MAGNET (B_{max}) VERSUS CURRENT IN MAGNET COILS (I_m) FOR THE MSA

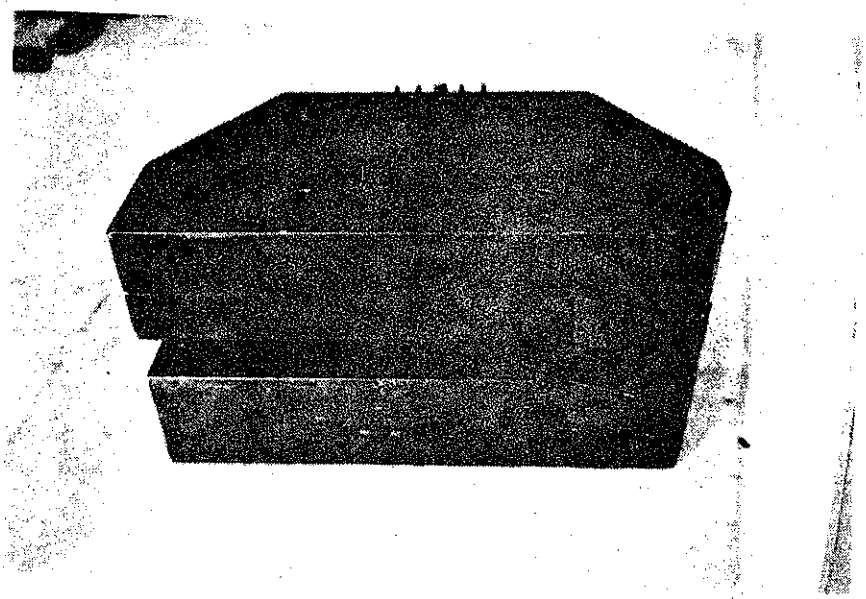

(a) MSA Magnet

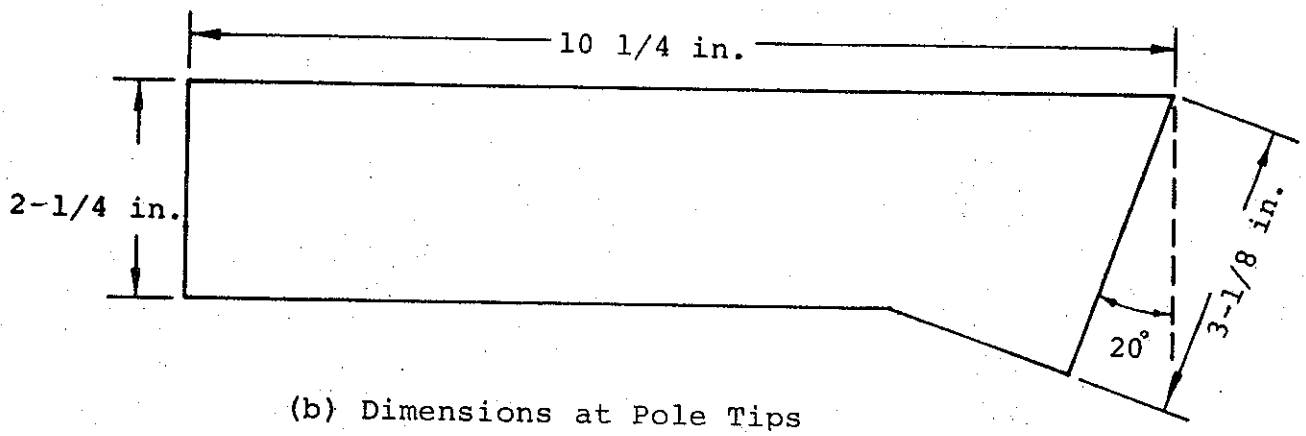

(b) Dimensions at Pole Tips

FIGURE A-2. PHOTO AND DIMENSIONS OF MSA MAGNET

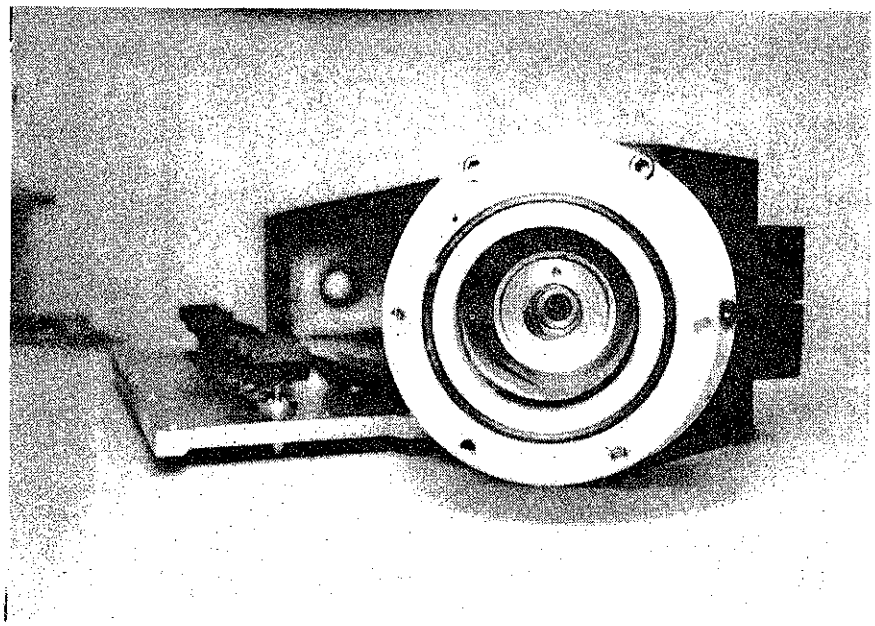

(a) View of collimator showing μ-metal foils and adjustable collimating slit.

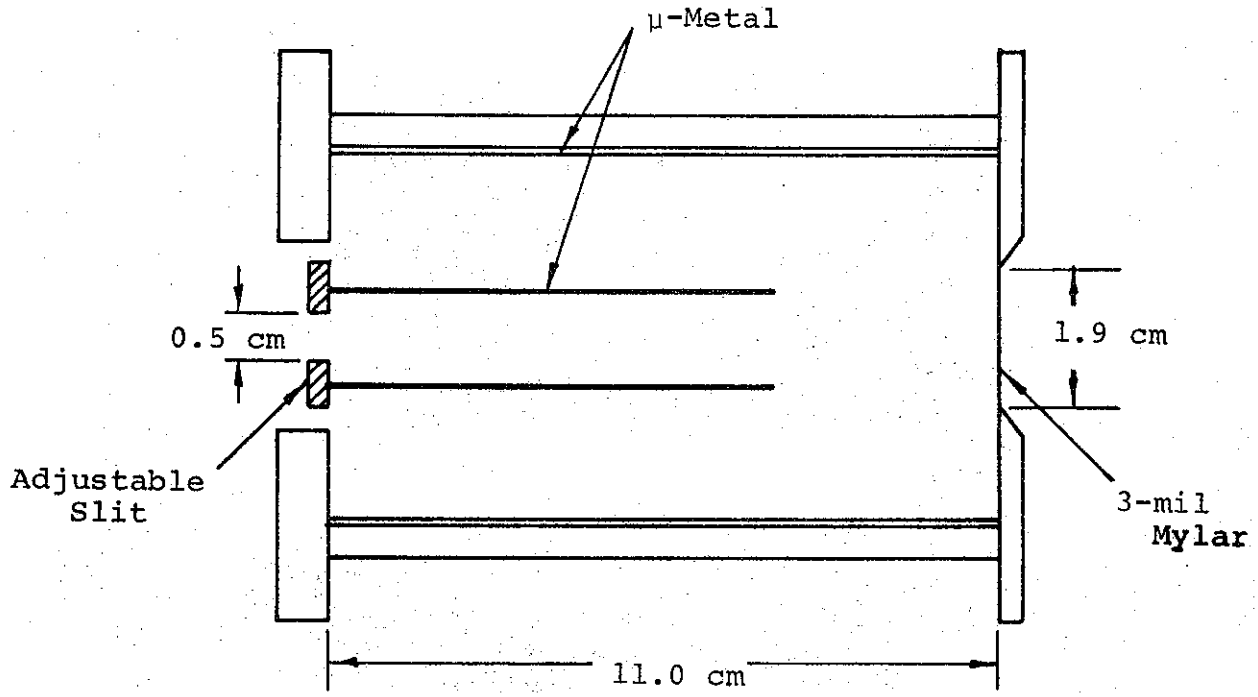

(b) Schematic of collimator

FIGURE A-3. MSA COLLIMATOR

In addition, a pair of scrapers are located beyond the rectangular slit. The electron beam enters the system through a 0.003-in. Mylar window at the circular aperture.

C. THE DETECTORS

The different energetic components of the beam are separated by the magnet and are then detected by a series of ten Faraday cups. The signals received by each detector are channeled to separate integrating networks from which both I(T) and q* can be recorded. A schematic of the integrating network for each channel and a photograph of the graphite array are shown in Figures A-4 and A-5, respectively.

The time-resolved signals are generally recorded on Tektronix Model 519 oscilloscopes, because of the extremely fast risetimes of the signals. The integrated outputs are recorded by a VIDAR Integrating Digital Voltmeter, which has a 20 channels per second printer output.

To demonstrate the compatibility of the two types of measurements, consider the results obtained from Shot 3131 on the Physics International Company Model 1140 Pulserad. Figure A-6 shows the oscilloscope trace obtained from Channel 6. Using a polar planimeter, the area under the curve on Channel 6 was found to be

$$A_6 = 1.94 \text{ cm}^2$$

---

*$q = \int I(T)dt$ over the duration of the pulse.

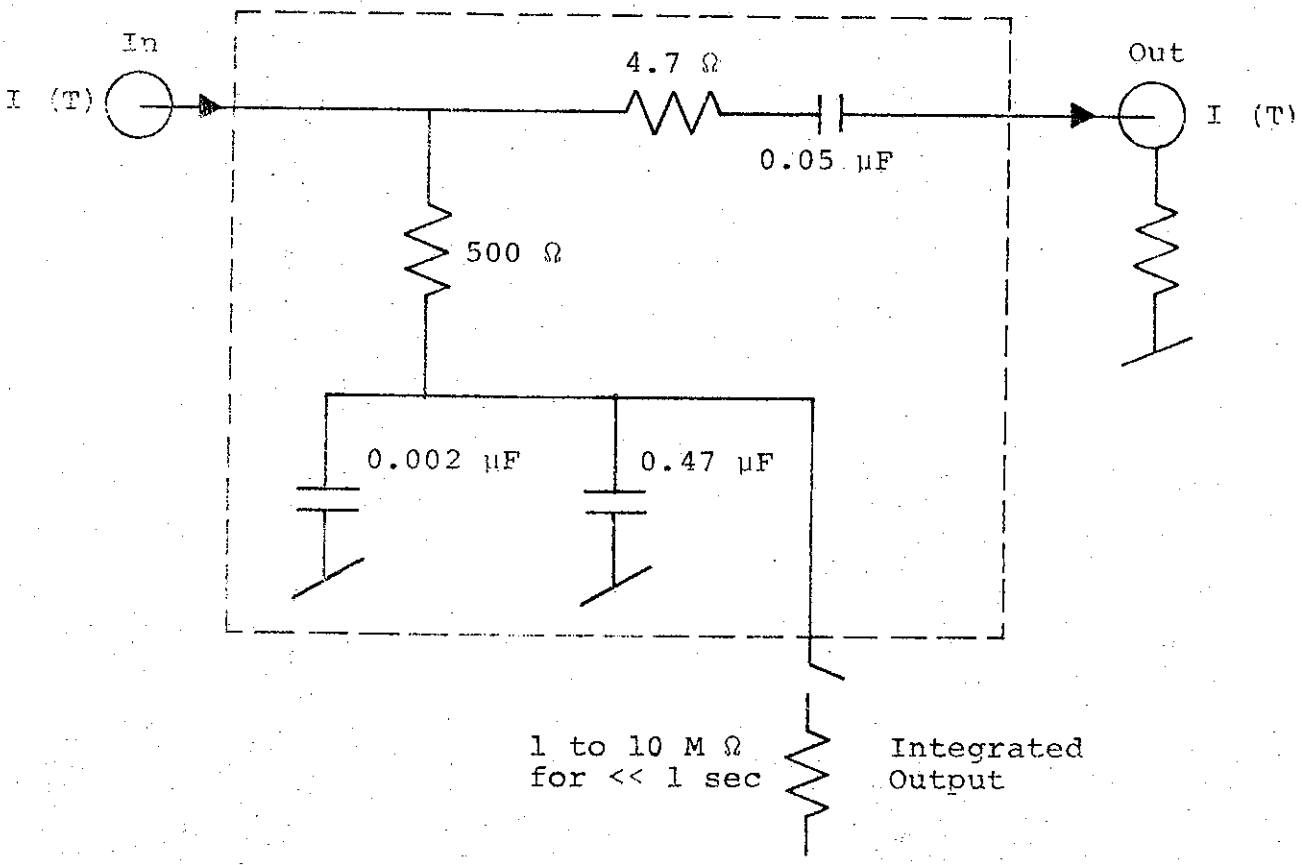

FIGURE A-4. MSA DETECTOR INTEGRATOR NETWORKS

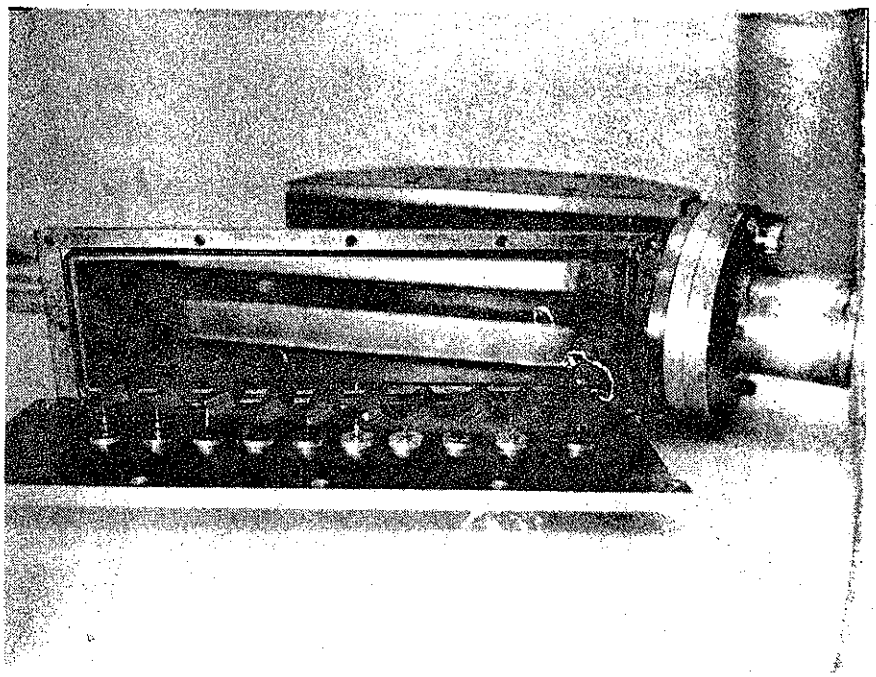

FIGURE A-5. MSA GRAPHITE DETECTORS

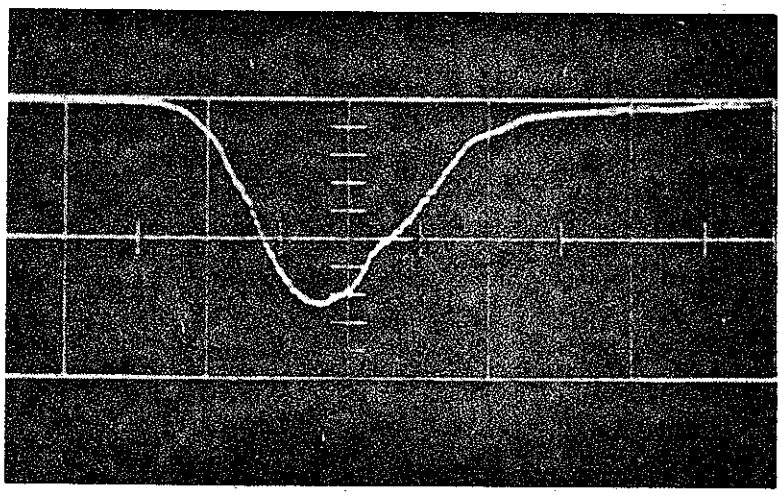

Note:

20 μsec/cm	Sweep Speed
17.8 V/cm	Sensitivity

FIGURE A-6. OSCILLOSCOPE TRACE OF CHANNEL 6

With a vertical sensitivity of 17.8 V/cm and a sweep speed of 20 nsec/cm we have

$$1 \text{ cm}^2 = 3.56 \times 10^{-7} \text{ V-sec}$$

Hence

$$A_6 = 6.92 \times 10^{-7} \text{ V-sec}$$

Now the total charge collected on Channel 6 is given by

$$Q_6 = \frac{A_6}{R} \times 1.11$$

$$Q_6 = \frac{6.92 \times 1.11 \times 10^{-7}}{5.0 \times 10} \frac{\text{V-sec}}{\Omega}$$

and

$$Q_6 = 1.53 \times 10^{-8} \text{ C}$$

(The factor 1.11 is used because only 90% of the input signal is transmitted to the oscilloscope.)

Referring to Figure A-4, the total capacitance of each integrator channel is given by

$$C = 5.22 \times 10^{-7} \text{ F}$$

Hence, the integrated output for each channel, in coulombs, is given by

$$Q_i = \Delta V_i \, C$$

where ΔV_i is the net voltage change across the integrating capacitor during the shot. On Shot 3131 we have

$$\Delta V_6 = 2.87 \times 10^{-2} \text{ V}$$

Hence

$$Q_6 = 1.50 \times 10^{-8} \text{ C}$$

in good agreement with the result obtained from the current waveform.

SECTION III

MSA CALIBRATION PROCEDURE

The MSA is calibrated using two separate techniques. One method determines the focal points for electrons of different energies, given the measured magnetic field gradient of the magnet while the other determines the focal point for 1-MeV electrons.

The calculation was performed by means of a computer code developed specifically for that purpose. The code calculates the trajectory of an electron in an inhomogeneous magnetic field given the field gradient, the maximum field strength, the energy of the electron, and the initial position and direction of the electron in the magnetic field. By plotting the trajectories of initially parallel, monoenergetic electrons, one obtains the focal point for these electrons as well as the angle at which these electrons pass through the focal point.

The magnetic field gradient was measured with a Bell 110A Gaussmeter. A ¼-in. grid was used to make B-field measurements of the entire area of the magnet and the fringe field area several inches beyond the pole tips of the magnet. This measurement was made with a B_{max} of 310 G. Later, measurements were made using several different magnet currents to determine whether the field gradient remained uniform over the range of expected operating currents. Figure A-7 illustrates the positions at which these measurements were taken.

The results of a number of these measurements are shown in Table A-1. Refer to Figure A-7 for an explanation of the row and column designations. The values of B in rows 1 and 2 have been normalized to the value of B in row 0. In the table, $A_{10} = B_{1,a}/B_{0,a}$;

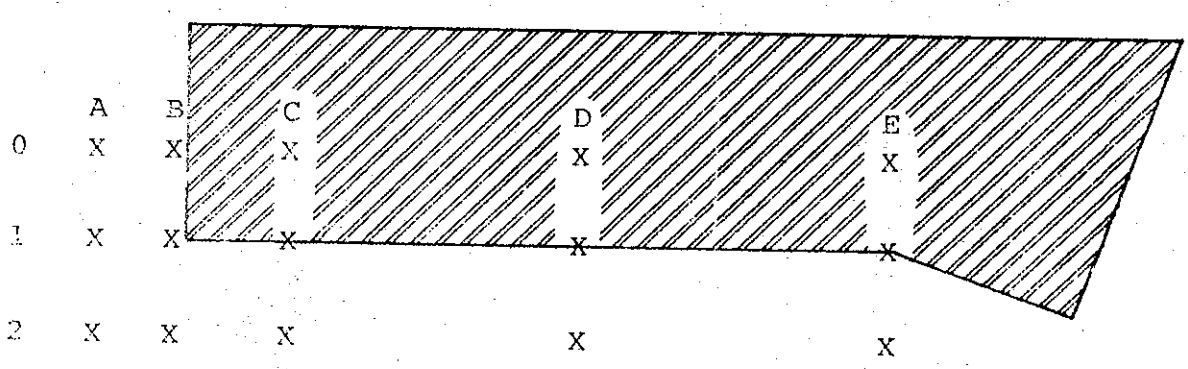

FIGURE A-7. PROBE LOCATIONS FOR B-FIELD MEASUREMENTS

TABLE A-I

RESULTS OF B-FIELD GRADIENT MEASUREMENTS FOR SEVERAL MAGNET CURRENTS

Magnet Current (A)	Column A		Column B		Column C		Column D		Column E	
	A_{10}	A_{20}	B_{10}	B_{20}	C_{10}	C_{20}	D_{10}	D_{20}	E_{10}	E_{20}
5.0	0.896	0.516	0.838	0.240	0.869	0.243	0.869	0.259	0.906	0.283
5.5	0.903	0.522	0.842	0.242	0.855	0.241	0.855	0.256	0.888	0.283
6.0	0.882	0.513	0.832	0.240	0.859	0.240	0.859	0.256	0.890	0.283
6.5	0.895	0.511	0.835	0.239	0.859	0.239	0.859	0.243	0.893	0.281
7.0	0.893	0.534	0.830	0.237	0.857	0.249	0.857	0.255	0.894	0.280
2.1	0.809	0.427	0.711	0.187	0.833	0.233	0.833	0.233	0.855	0.258

where the first B subscript refers to row number, and the second to the column letter. The last row in the table was obtained from the magnetic field gradient incorporated into the computer code. A B_{max} of 310 G implies a magnet current of 2.1 A.

From Table A-I, it appears that discrepancies exist between the field gradient incorporated into the code and those present during actual operation of the MSA. The differences are on the order of 10 and 20% for columns A and B, but are less than 5% for columns C, D, and E. It should be pointed out, however, that for the field strength of greatest interest, that is B_{max} = 900 G, I_m = 6.30 A, the electrons reaching the highest energy channels never pass through the regions represented by Columns A and B. The detector locations were calculated for this field. The highest energy channel in this configuration is 5.0 MeV, much higher than the mean energy expected from the Model 1140 Pulserad. Hence, the field gradient used in the calculation was in error by no more than 5% from the field gradient when the MSA was in use on the Model 1140 Pulserad.

The second method employed in the calibration of the MSA was an experimental determination of the focal point for 1.0-MeV electrons. A 100-μCi sample of Bi^{207} was used as a source of electrons. (One curie is equal to 3.7×10^{10} disintegrations per second.) Bi^{207} decays to Pb^{207} by electron capture, and Pb^{207} subsequently decays to its ground state, radiating a 1.064-MeV and a 0.570-MeV gamma ray in the process. Orbital electrons ejected as a result of these gamma rays were used to calibrate the MSA.

The conversion efficiency, that is, the ratio of electrons ejected to gamma rays produced, of the 1.064-MeV gamma ray, γ_1, is 0.30. For the 0.570-MeV gamma ray, γ_2, the conversion efficiency is only 0.02. Hence, in any given time interval, if we denote by N_{γ_1} and N_{e_1} the number of gamma rays and electrons produced, we can write

$$N_{e_1} = 0.30\, N_{\gamma_1} \quad \text{and} \quad N_{e_2} = 0.02\, N_{\gamma_2}$$

Because $N_{\gamma_2} = N_1$, we have $N_{e_1}/N_{e_2} = 15$

Now $N_e = N_{e_1} + N_{e_2}$. Therefore $N_{e_1} \cong 0.94\, N_e$

The ratio of electrons ejected from the K shell to those ejected from the L shell (those ejected from higher order levels are insignificant) is

$$\text{for } \gamma_1, \frac{K}{L} = 4.0$$

$$\text{for } \gamma_2, \frac{K}{L} = 4.4$$

Hence, we have

$$N_{e_{1K}} \cong 0.75\, N_e$$

$$N_{e_{1L}} \cong 0.19\, N_e$$

$$N_{e_{2K}} \cong 0.05\, N_e$$

$$N_{e_{2L}} \cong 0.01\, N_e$$

The binding energies of the K and L electrons in Pb^{207} are given by

$$E_{B_K} = 0.088 \text{ MeV}$$

$$E_{B_L} = 0.015 \text{ MeV}$$

The spectral distribution of electrons emitted by the Bi^{207} source may be written:

$$N_{e_{1K}} (e^- + 0.976 \text{ MeV}) = 0.75 N_e$$

$$N_{e_{1L}} (e^- + 1.049 \text{ MeV}) = 0.19 N_e$$

$$N_{e_{2K}} (e^- + 0.482 \text{ MeV}) = 0.05 N_e$$

$$N_{e_{2L}} (e^- + 0.555 \text{ MeV}) = 0.01 N_e$$

There are other decay modes for Pb^{207} to the ground state, but these modes contribute only a small fraction of the total gamma ray output, and the distribution derived above is sufficiently accurate for our purposes. Considering the inherent inaccuracies of our experiment, the distribution is essentially

$$N_{e_1} (e^- + 1.0 \text{ MeV}) = 0.94 N_e$$

$$N_{e_2} (e^- + 0.5 \text{ MeV}) = 0.06 N_e$$

Now, the radioactivity of our sample is

$$\rho = 3.7 \times 10^6 \text{ dis/sec}$$

Hence, the total electron flux, n_e, is given by

$$n_e = \frac{dN_e}{dT} = n_{e_1} + n_{e_2}$$

$$n_e = 0.32$$

$$n_e = 1.12 \times 10^6 \text{ sec}^{-1}$$

The 1.0-MeV electron flux in a solid angle of 4π is then

$$n_{e_1} = 1.11 \times 10^6 \text{ sec}^{-1}$$

During the calibration procedure the source was located inside the vacuum chamber, positioned at the circular collimating slit. The rectangular slit, 0.5 by 0.5 cm, was 10.5 cm from the source. The solid angle subtended at the source by the slit is given approximately by

$$\alpha \cong \frac{(0.5 \text{ cm})^2}{(10.5 \text{ cm})^2}$$

$$\alpha \cong 2.27 \times 10^{-3} \text{ steradians}$$

Hence, the electron flux entering the MSA is given by

$$\bar{n}_{e_1} = 2.52 \times 10^3 \text{ electrons/sec}$$

or by

$$\bar{n}_{e_1} = 4.03 \times 10^{-16} \text{ A}$$

To detect this small current a photomultiplier was employed in conjunction with a Pilot B scintillator. A single channel, pulse-height analyzer and counter was used to analyze the photomultiplier output. In addition, a pulse stretcher was designed

for and incorporated into the system to lengthen the photomultiplier pulses, which were too narrow to be recorded by our counter.

After passing through the magnet, the electrons passed through a Mylar window before entering the scintillator. The scintillator, a 0.5- by 0.5- by 0.25-in. piece of Pilot B, was coupled to a Lucite light pipe, which was in turn coupled to the photomultiplier. The photomultiplier (an RCA 6810A) was shielded magnetically with mu-metal foils.

A schematic of the pulse amplifier constructed for this experiment appears in Figure A-8. The amplifier was calibrated for different bias voltages to test its linearity, and the results of these measurements are shown in Figure A-9.

Measurements were made with the photomultiplier at ½-in. intervals along the Mylar window. At each position, four readings were taken at 30-sec intervals and the results averaged. Measurements were made at both B_{max} equal to 0 G and at B_{max} equal to 900 G. A schematic of the experiment is shown in Figure A-10. The difference between these readings is plotted as a function of position in Figure A-11. A geometrical correction factor has been applied to the position readings to account for the fact that the electrons were not incident at right angles to the Mylar window, but were in fact incident at approximately 45 deg. This has the effect of shifting the effective position of the photomultiplier by roughly 1/8-in. toward the collimating region. A further shift in the same direction is justified because of the scattering of the beam by the Mylar window, but this effect has not been included.

Figure A-12 shows the calculated focal points for 1.0- and 2.0-MeV electrons in a field of 900 G. The trajectories of electrons

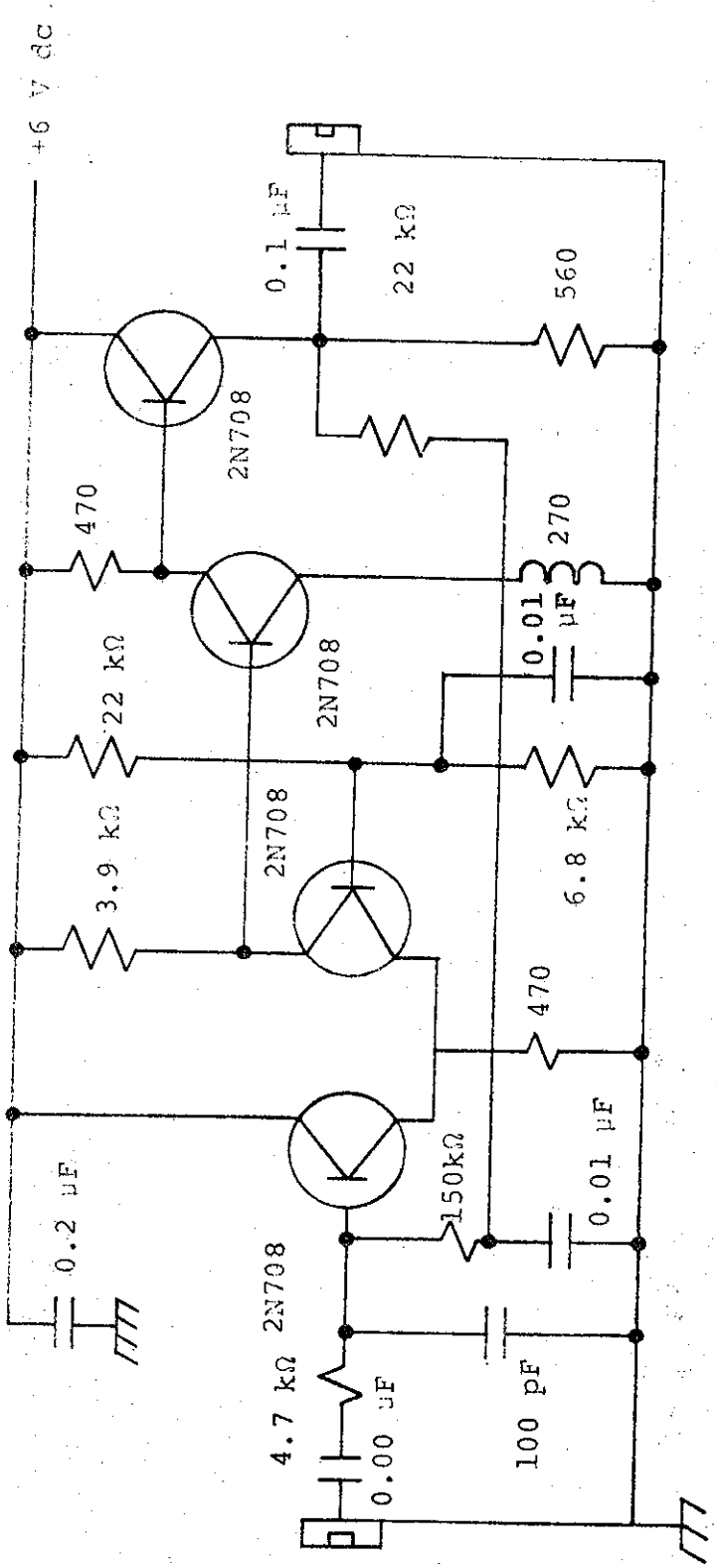

FIGURE A-8. INTEGRATOR-AMPLIFIER FOR PHOTOMULTIPLIER OUTPUT

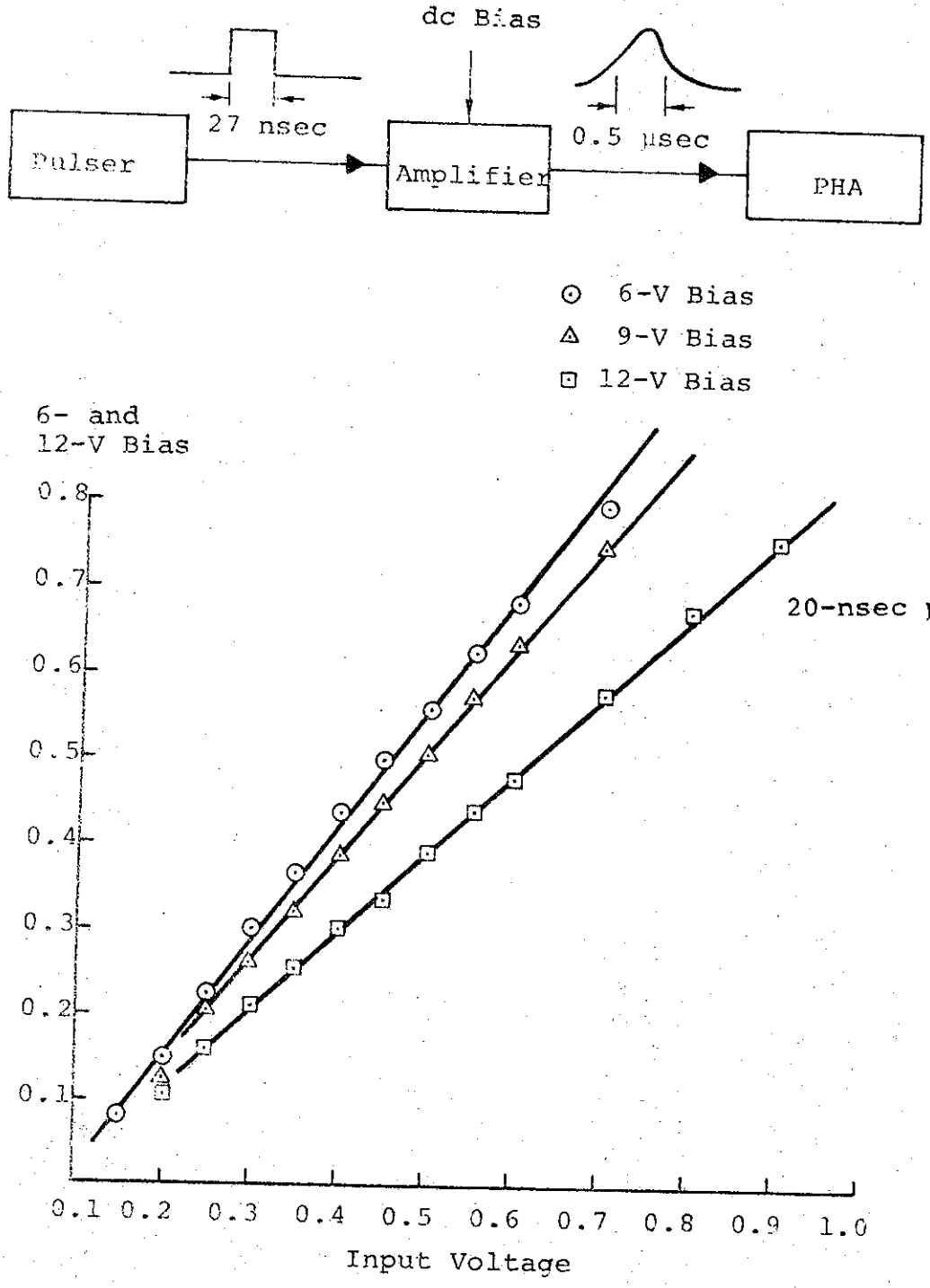

FIGURE A-9. LINEARITY TEST OF INTEGRATOR-AMPLIFIER

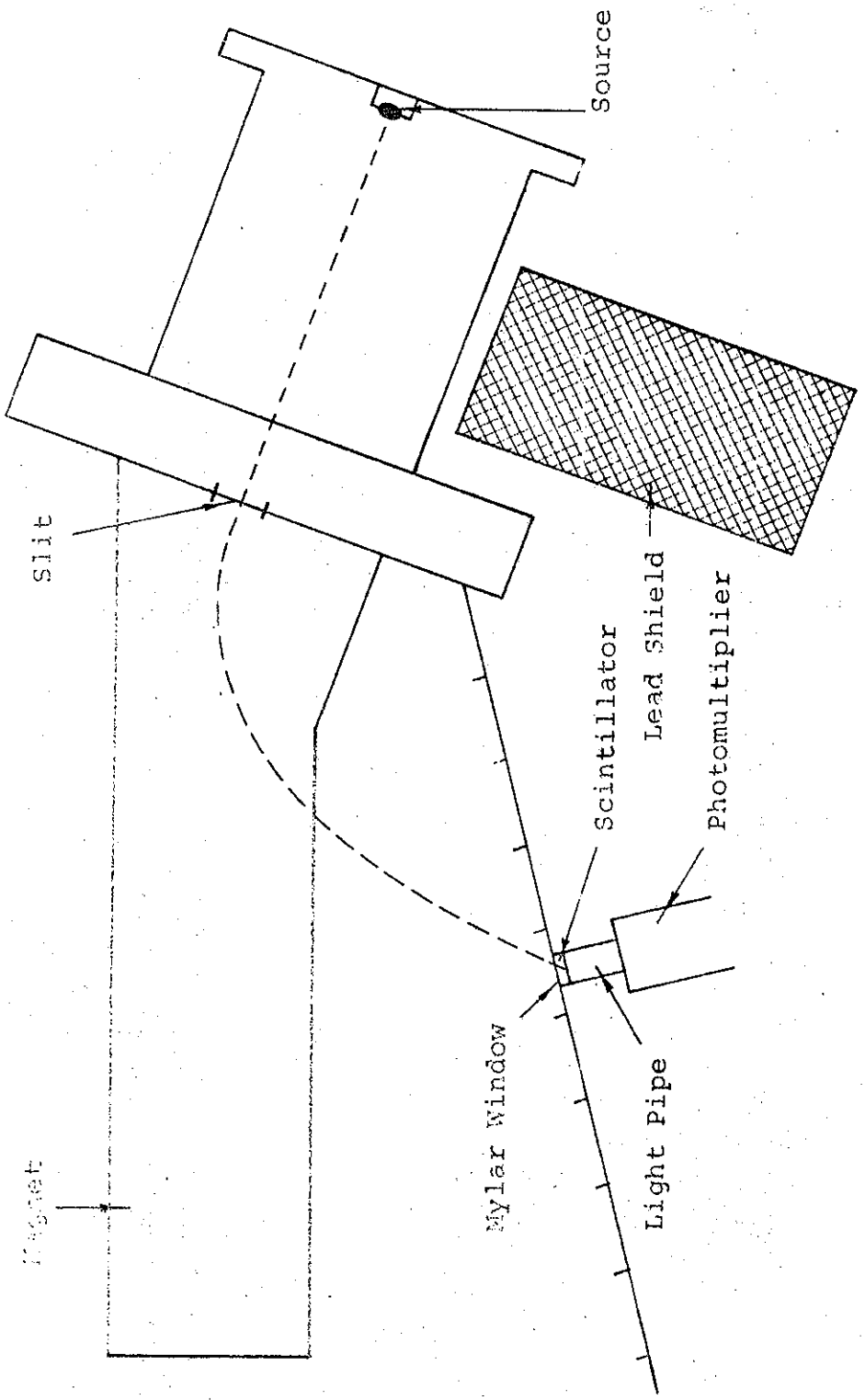

FIGURE A-10. MSA CALIBRATION EXPERIMENT SCHEMATIC

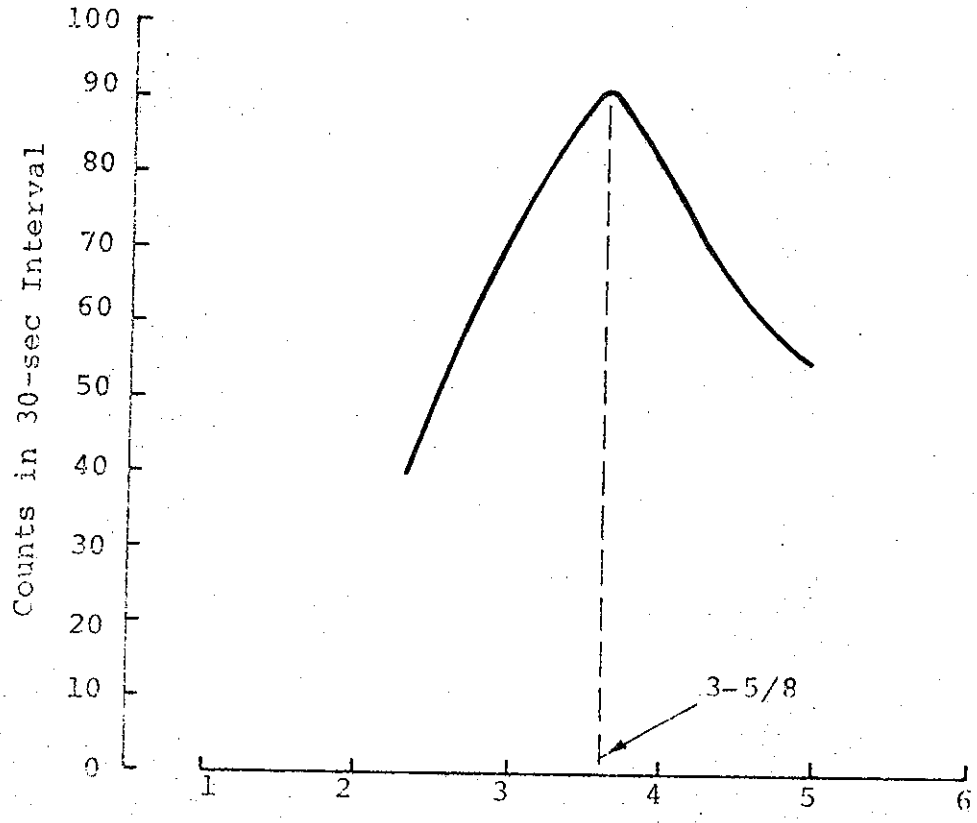

FIGURE A-11. PHOTOMULTIPLIER POSITION VERSUS COUNTING RATE

Note: PM Bias, 1700V; pulse stretcher bias, 9V; minimum pulse height counted, 0.15V

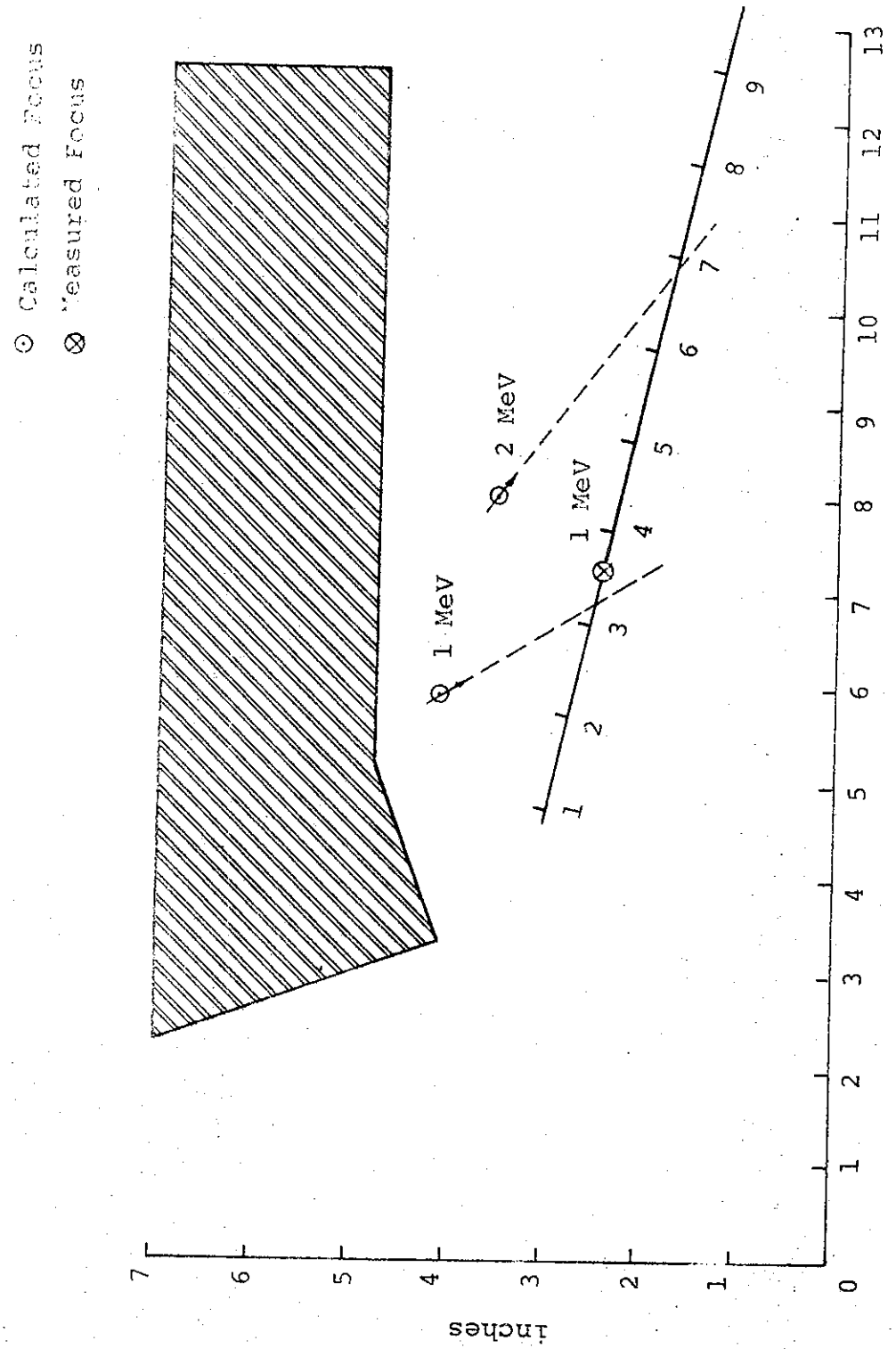

FIGURE A-12. CALCULATED AND MEASURED FOCAL POINTS OF MSA AT 900 GAUSS

entering the MSA on the beam axis have been extended beyond the focal points and through the plane containing the Mylar window. The location of the measured intersection of this plane with 1-MeV electrons is also indicated. With the correction that has been made in the experimental calibration, there is a 10% difference between the measured and calculated focal points. If one were to include scattering effects, this difference presumably would be smaller.

APPENDIX B

BEAM SCATTERING PROFILES

The following beam scattering profiles were plotted from the Model 1140 and 730 Pulserad experiments. Figures B-1 through B-9 present those from the Model 1140 Pulserad and Figures B-10 through B-23 present those from the Model 730.

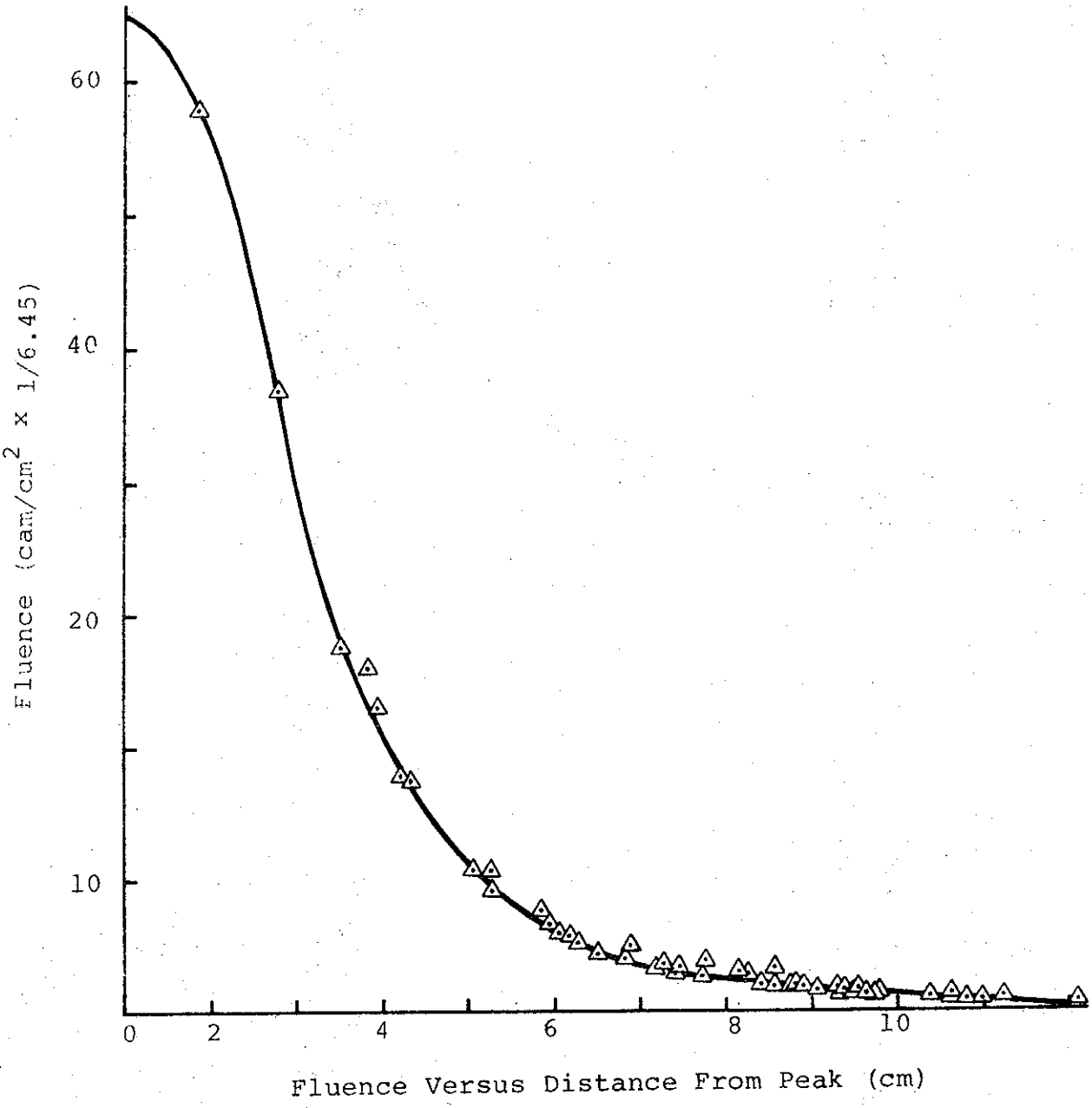

FIGURE B-1. SHOT 3785, ANODE TO CALORIMETER DISTANCE 15 cm, NO SCATTERER, σ_t = 1.82 cm

7885

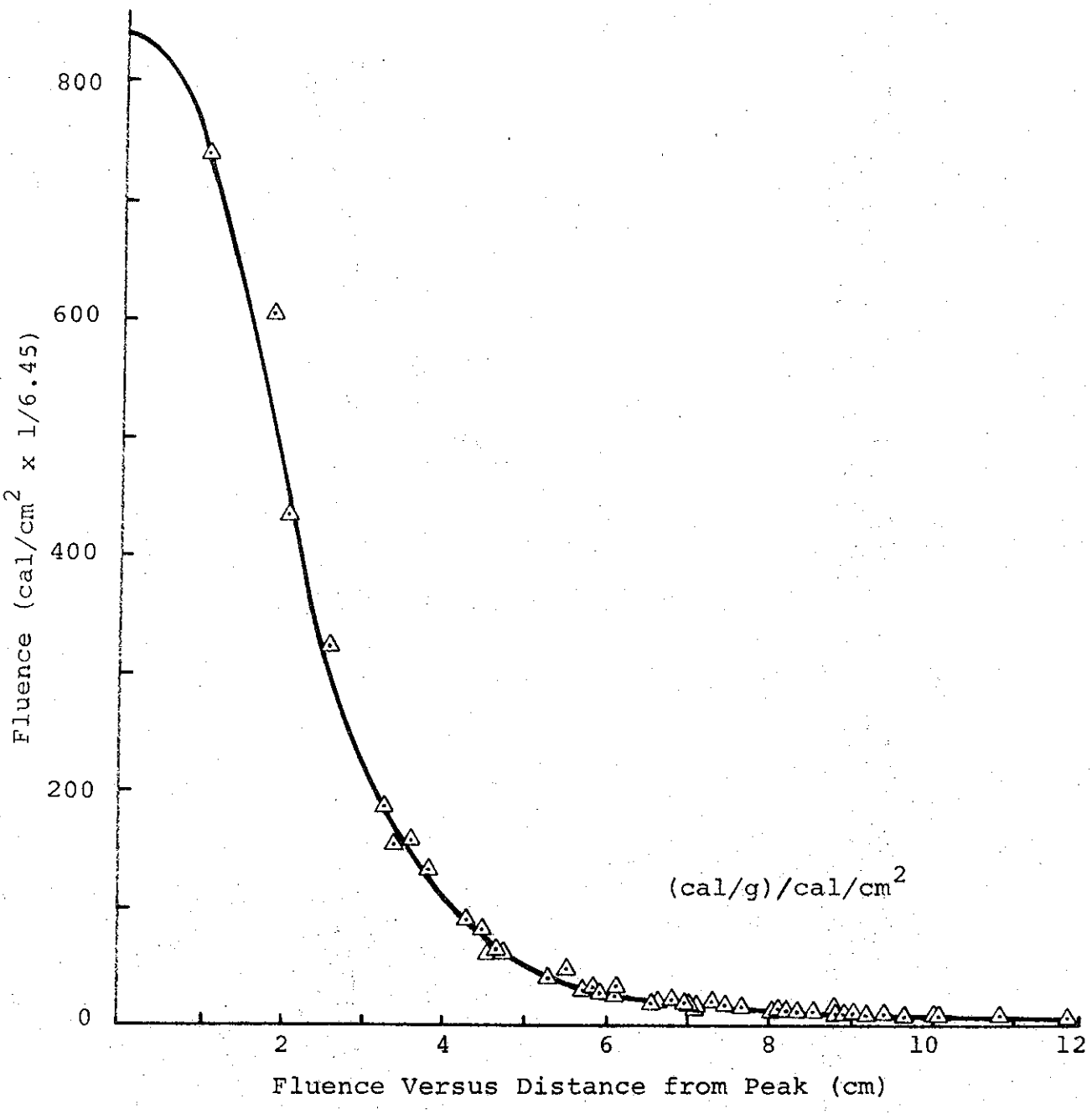

FIGURE B-2. SHOT 3786, NO SCATTERER, σ_t = 1.85 cm

7824

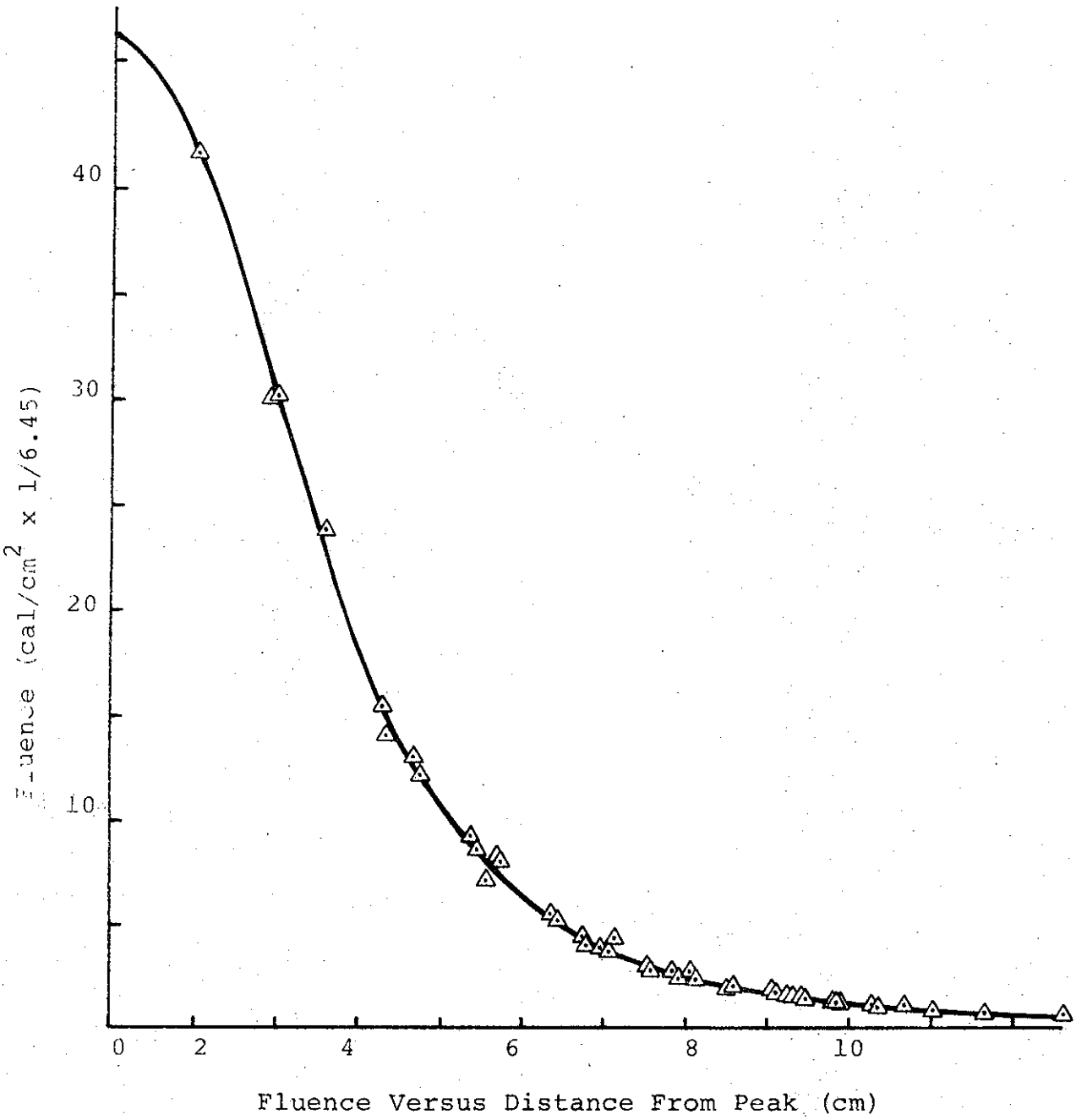

FIGURE B-3. SHOT 3788, 20-mil ALUMINUM SCATTERER, σ_t = 2.12 cm

7883

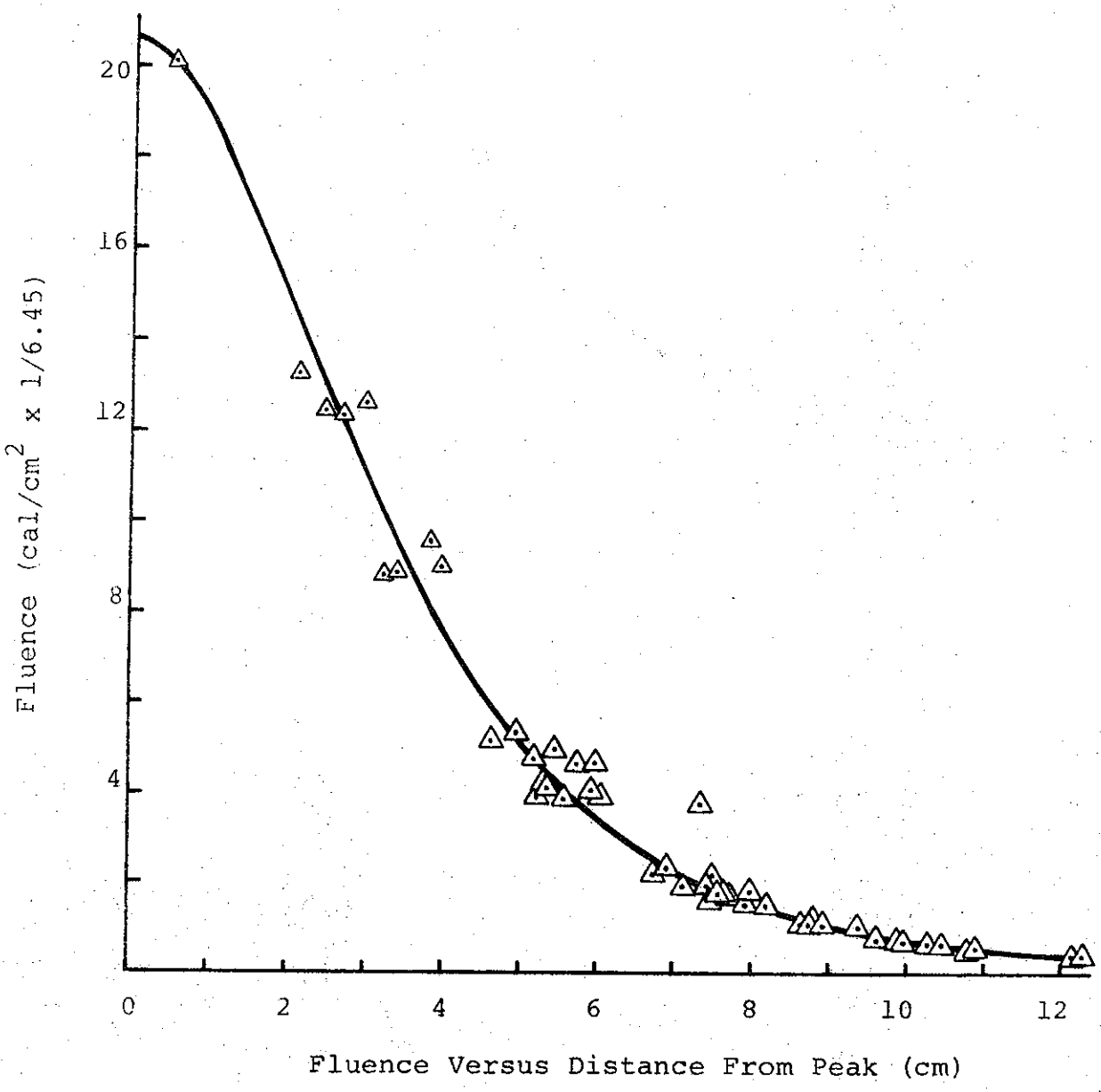

FIGURE B-4. SHOT 3789, 60-mil ALUMINUM SCATTERER, σ_t = 2.6 cm

7882

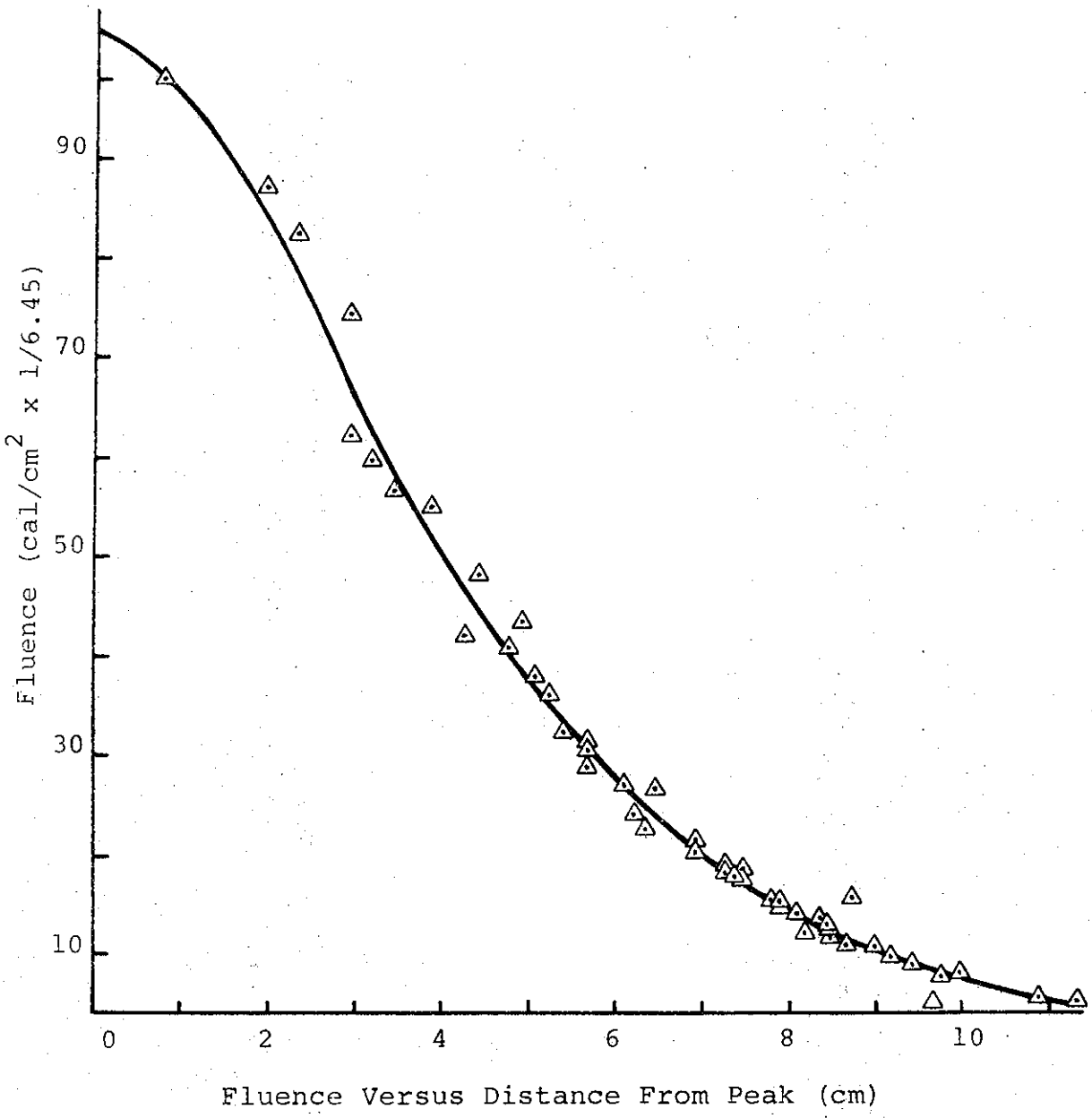

FIGURE B-5. SHOT 3790, 120-mil ALUMINUM SCATTERER, o_t = 3.15 cm

7881

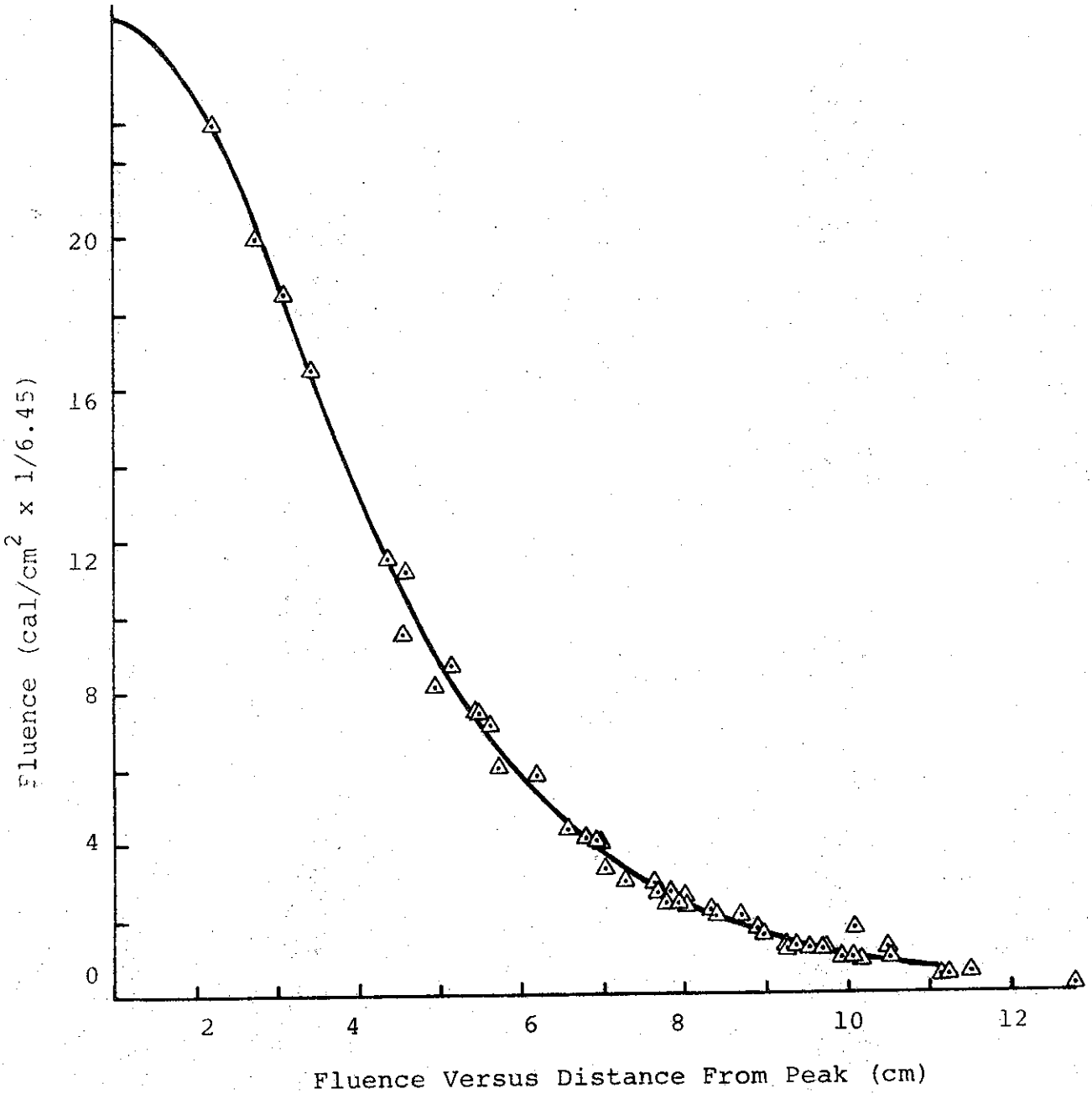

FIGURE B-6. SHOT 3792, 16-mil TITANIUM SCATTERER, σ_t = 2.55 cm

7880

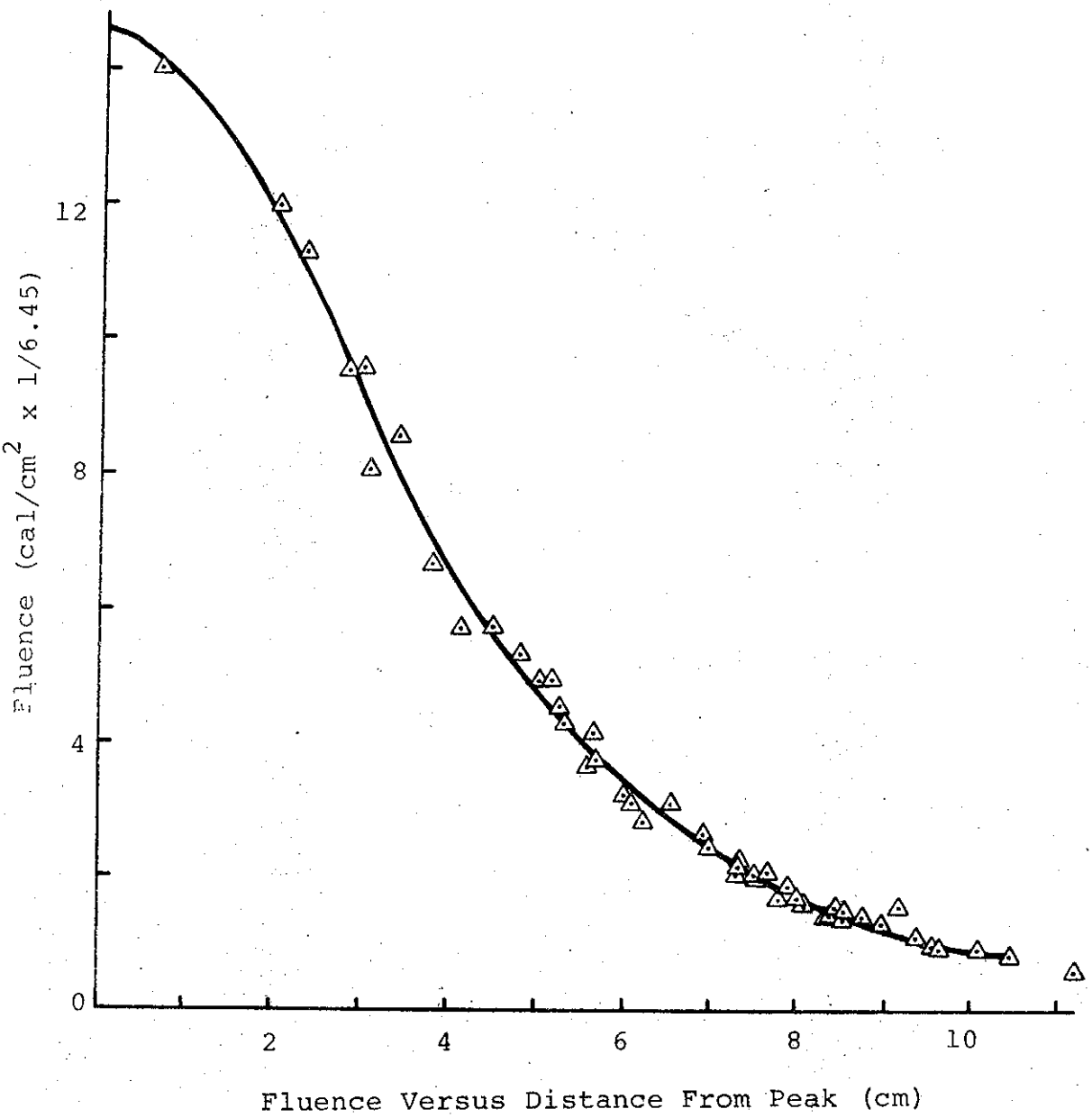

FIGURE B-7. SHOT 3793, 32-mil TITANIUM SCATTERER, σ_t = 3.1 cm

7879

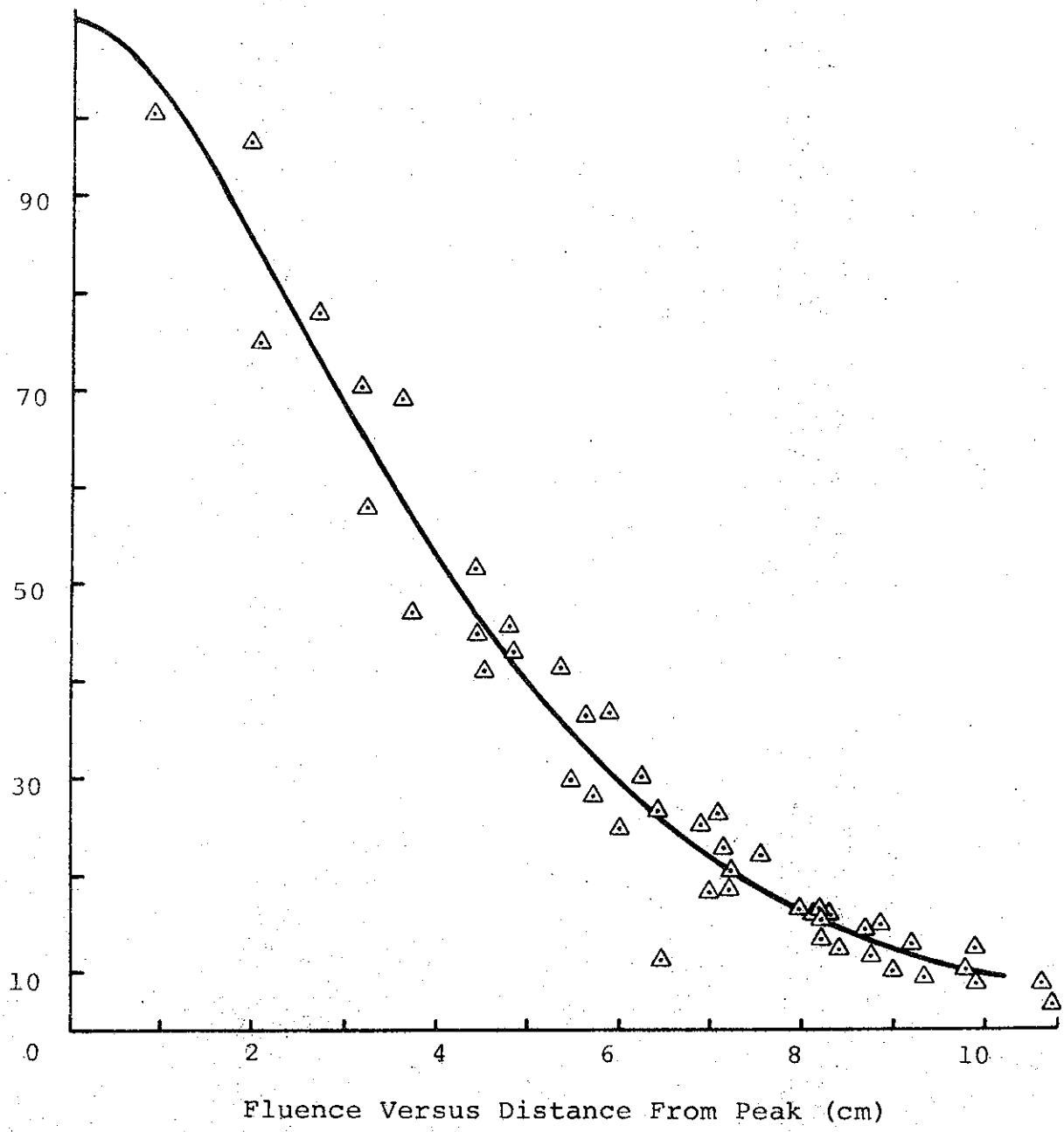

FIGURE B-8. SHOT 3794, 48-mil TITANIUM SCATTERER, σ_t = 3.2 cm

7878

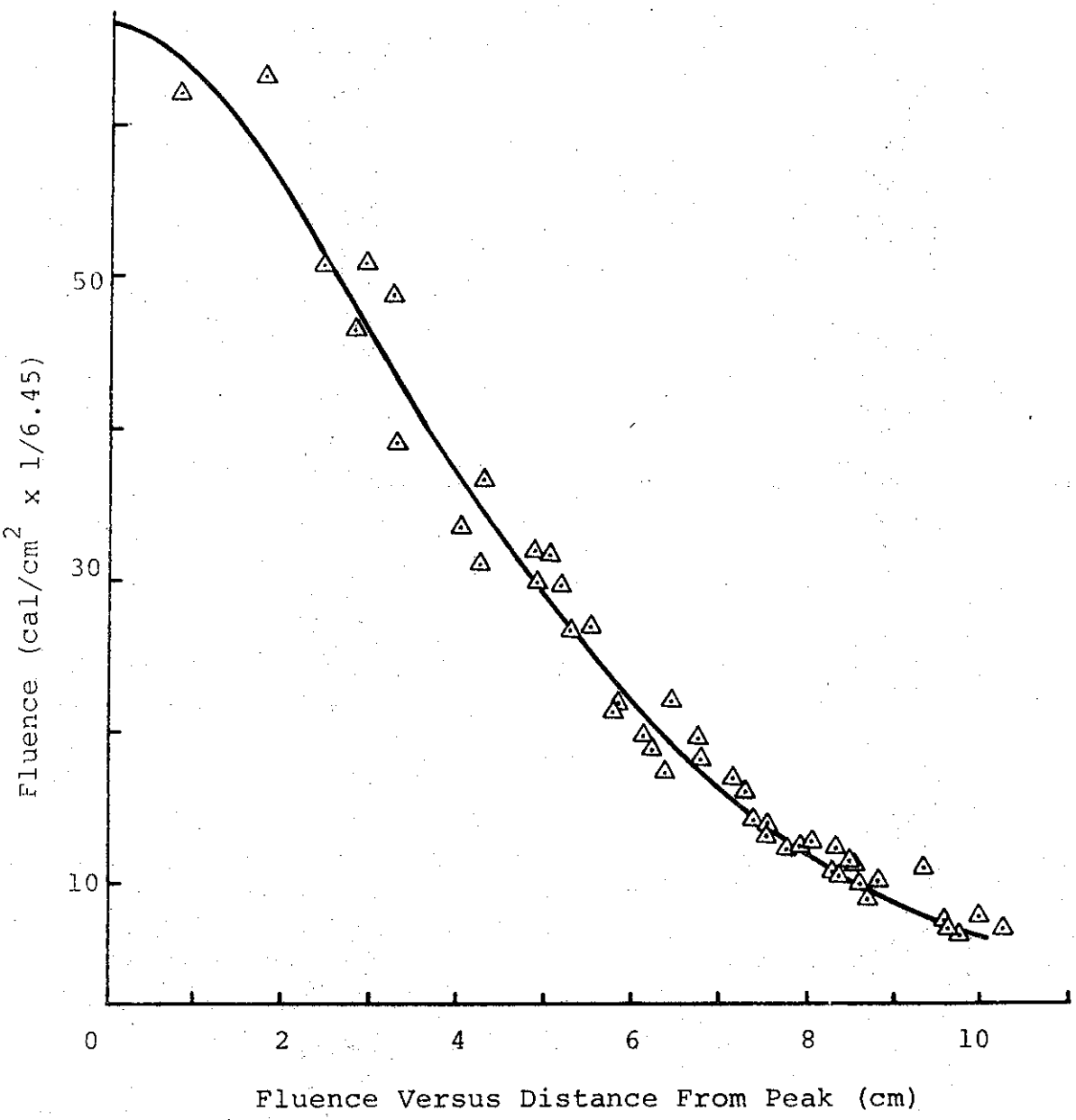

FIGURE B-9. SHOT 3795, 64-mil TITANIUM SCATTERER, c_t = 3.55 cm

7877

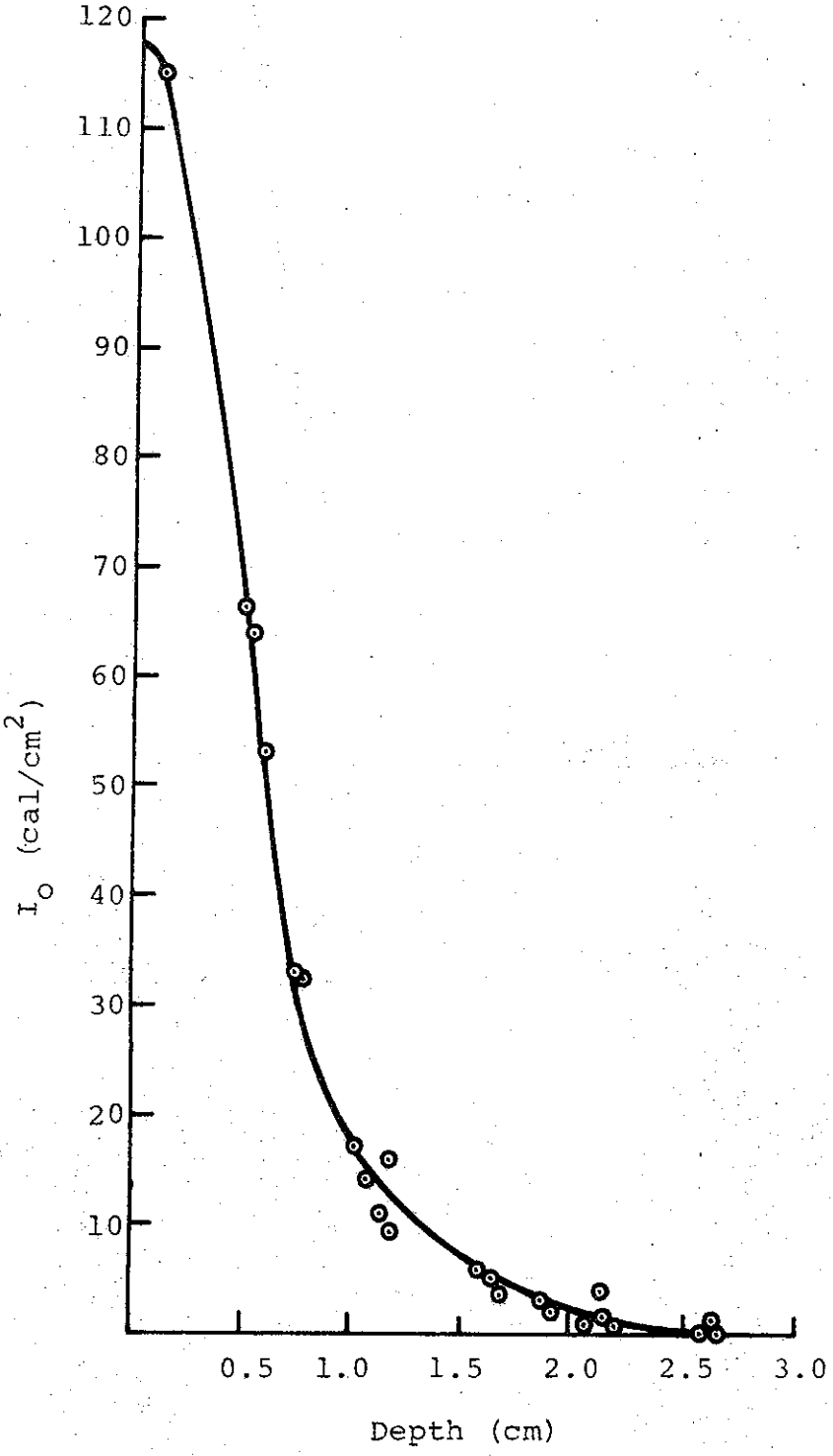

FIGURE B-10. SHOT 9659, CONFIGURATION I (COLLIMATOR PLATES), NO SCATTERER, ANODE TO CALORIMETER DISTANCE 3.5 cm, σ= 0.45 cm

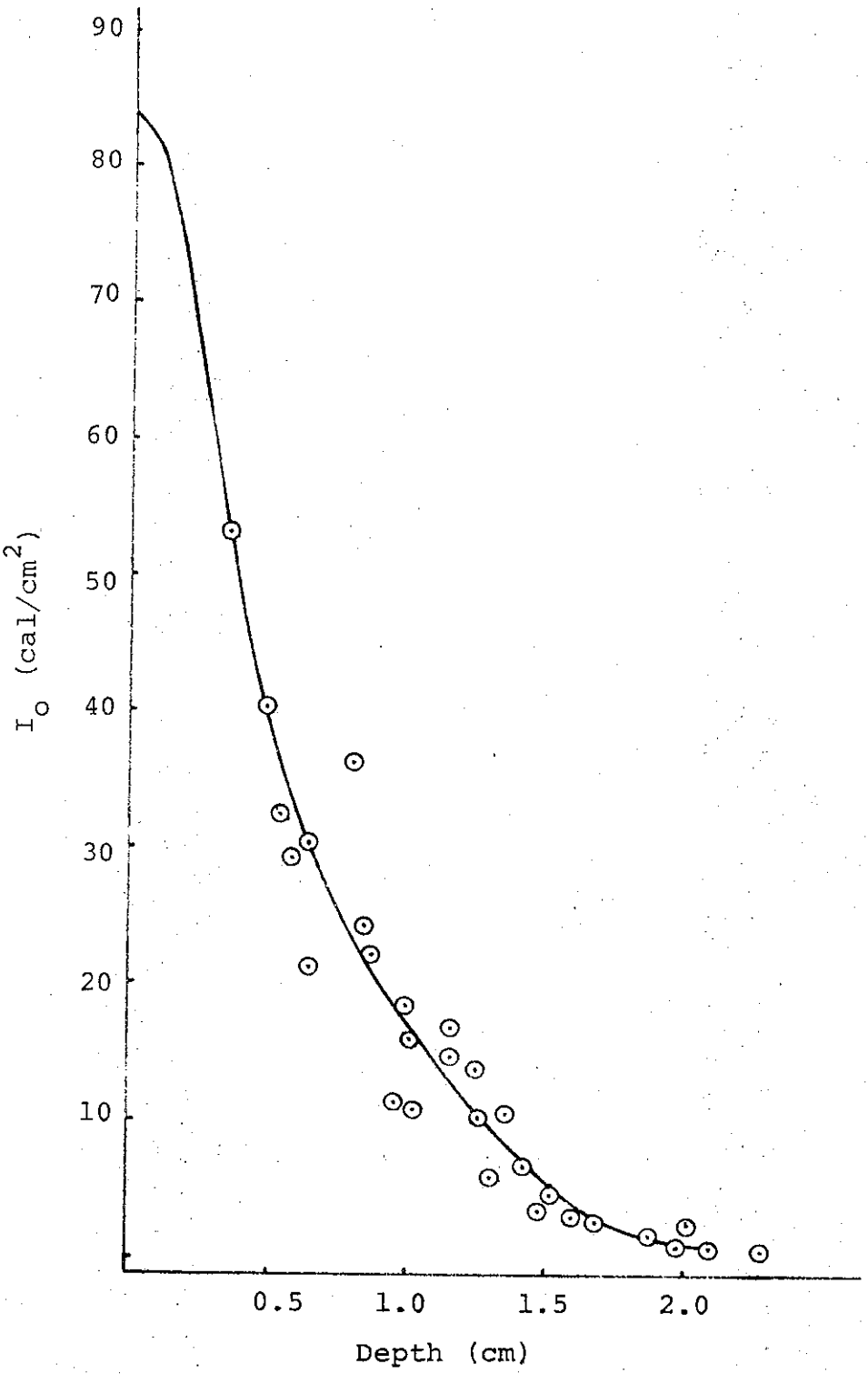

FIGURE B-11. SHOT 9665, CONFIGURATION I (COLLIMATOR PLATES), NO SCATTERER, σ = 0.4 cm

5981

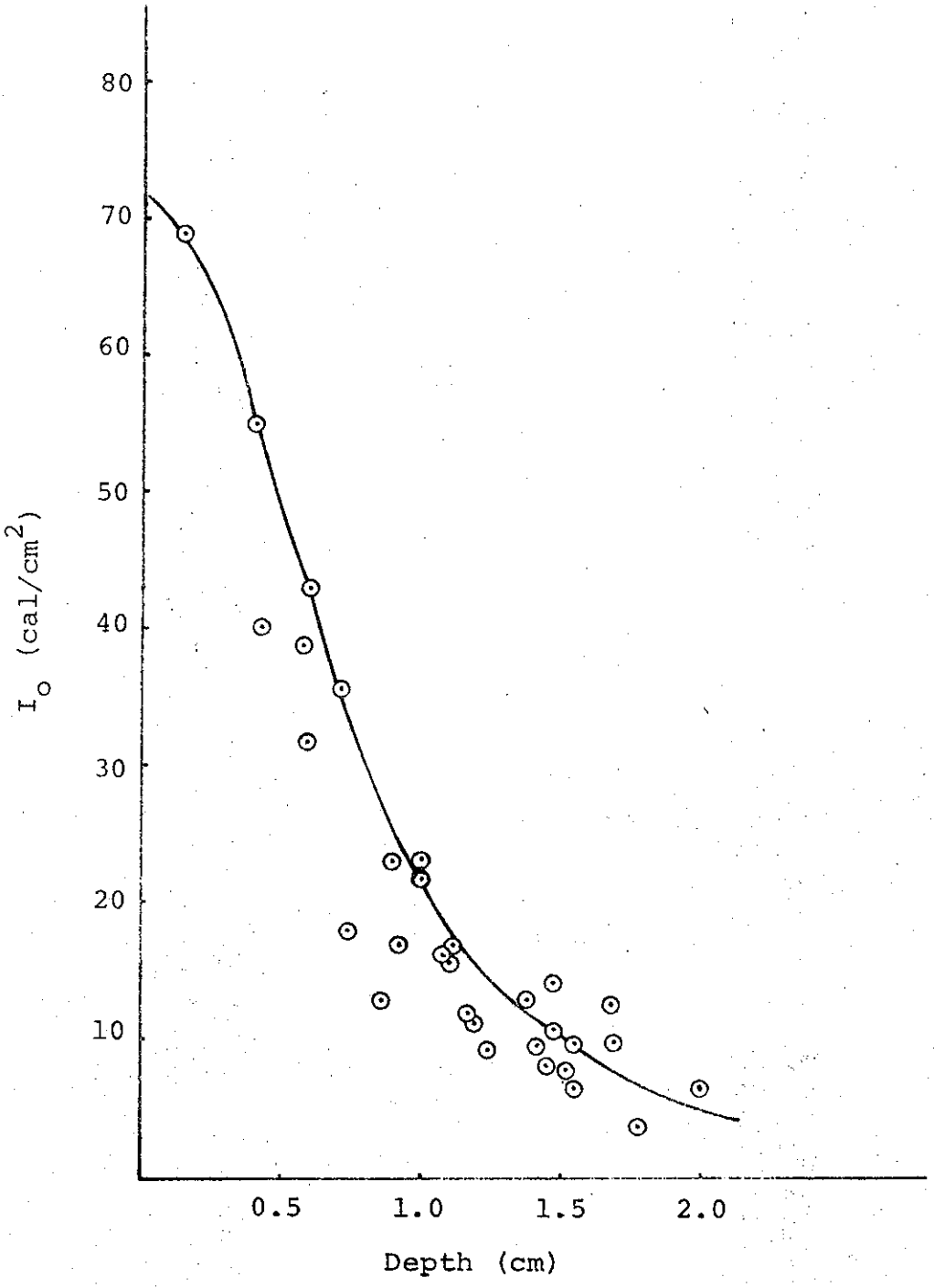

5983

FIGURE B-12. SHOT 9661, CONFIGURATION I (COLLIMATOR PLATES), 0.9-mil ALUMINUM SCATTERER, σ = 0.57 cm

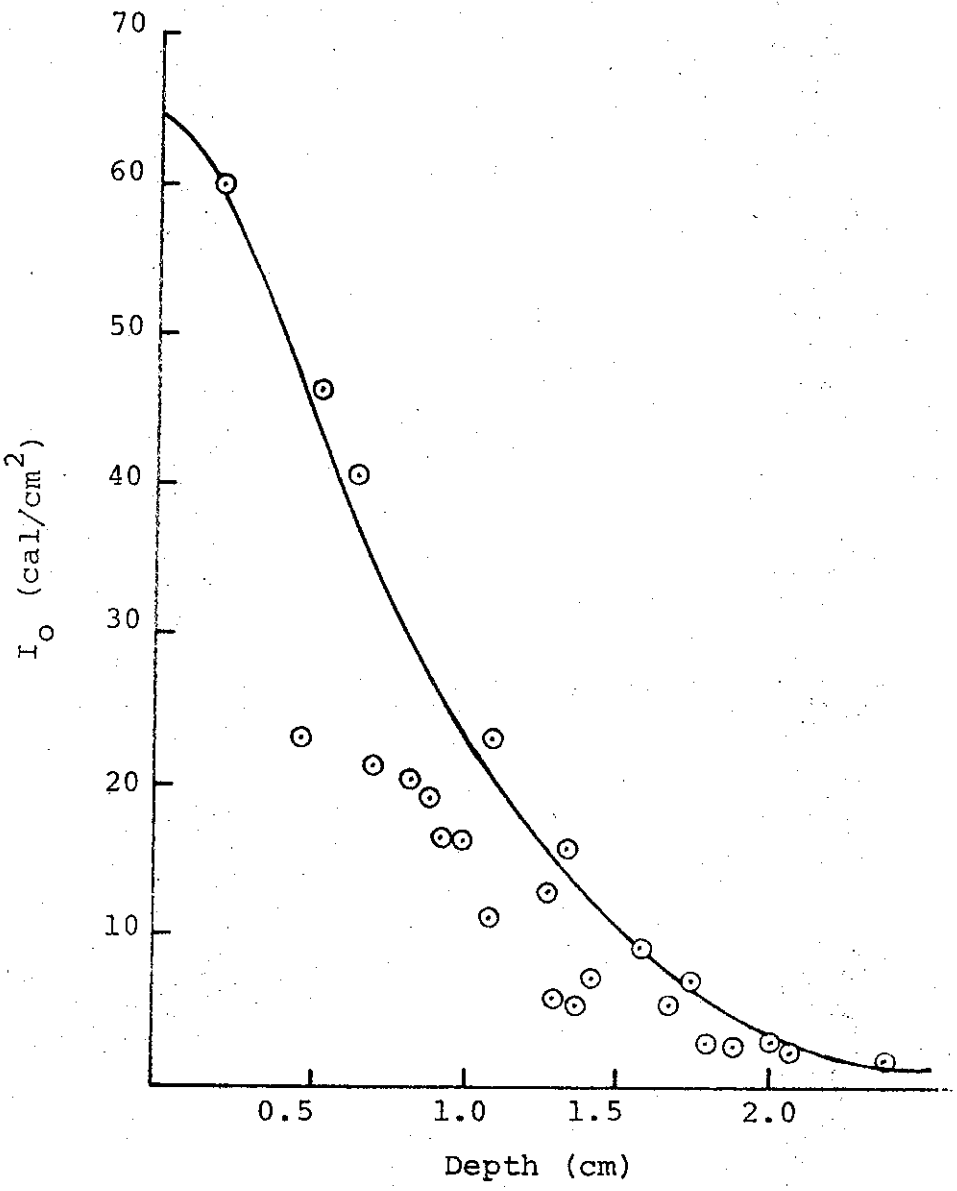

FIGURE B-13. SHOT 9660, CONFIGURATION I (COLLIMATOR PLATES), 1.8-mil ALUMINUM SCATTERER, σ = 0.65 cm

5982

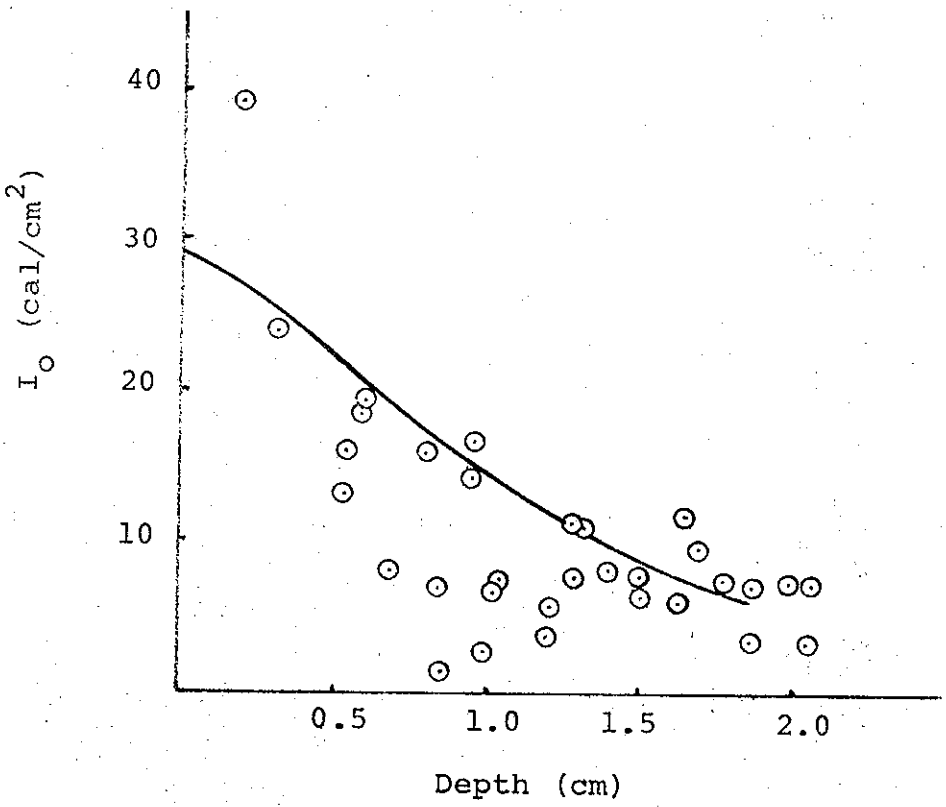

FIGURE B-14. SHOT 9664, CONFIGURATION I (COLLIMATOR PLATES), 2.7-mil ALUMINUM, σ = 0.76 cm

5984

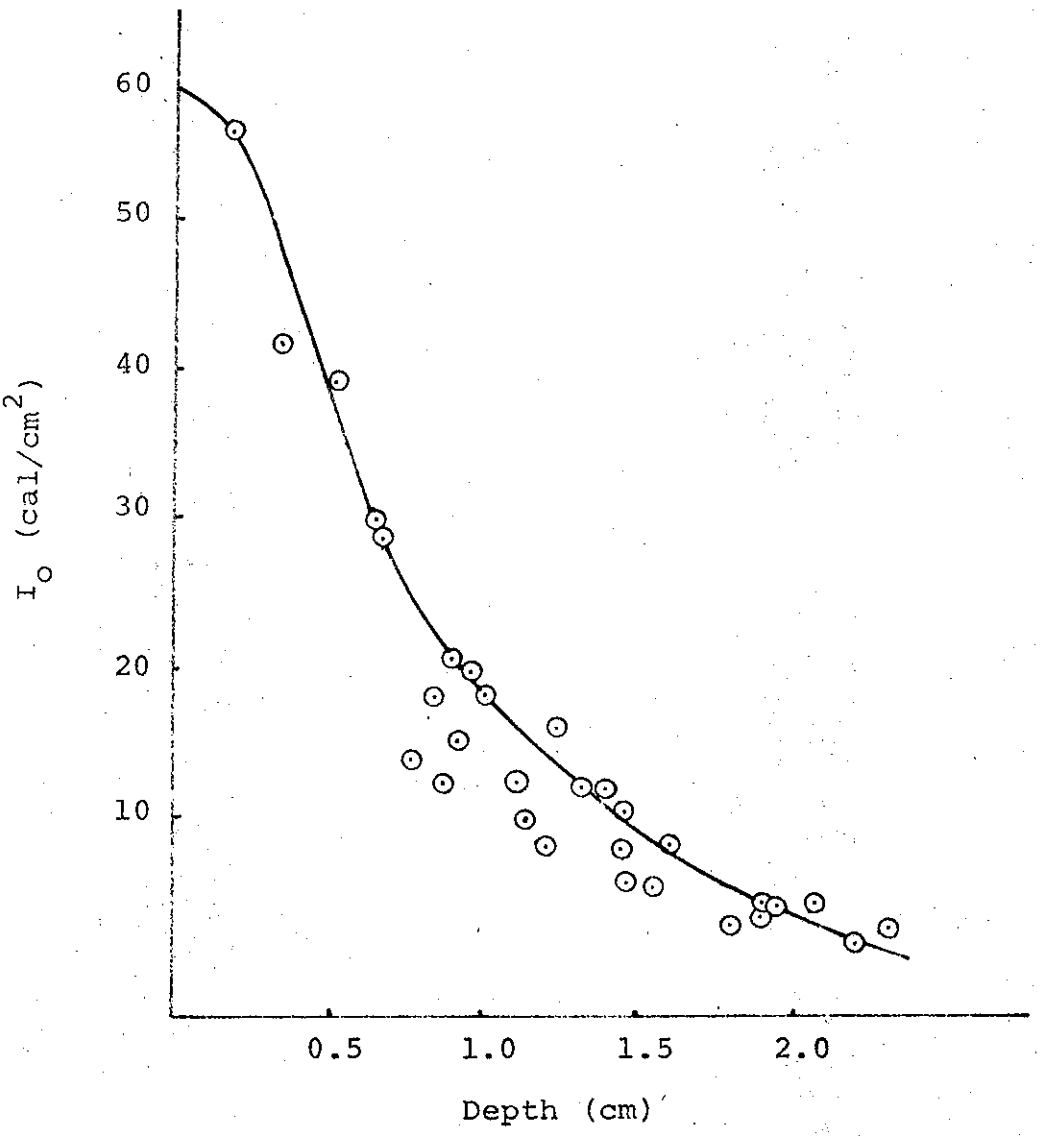

FIGURE B-15. SHOT 9662, CONFIGURATION I (COLLIMATOR PLATES), 0.5-mil TITANIUM SCATTERER, σ = 0.57 cm

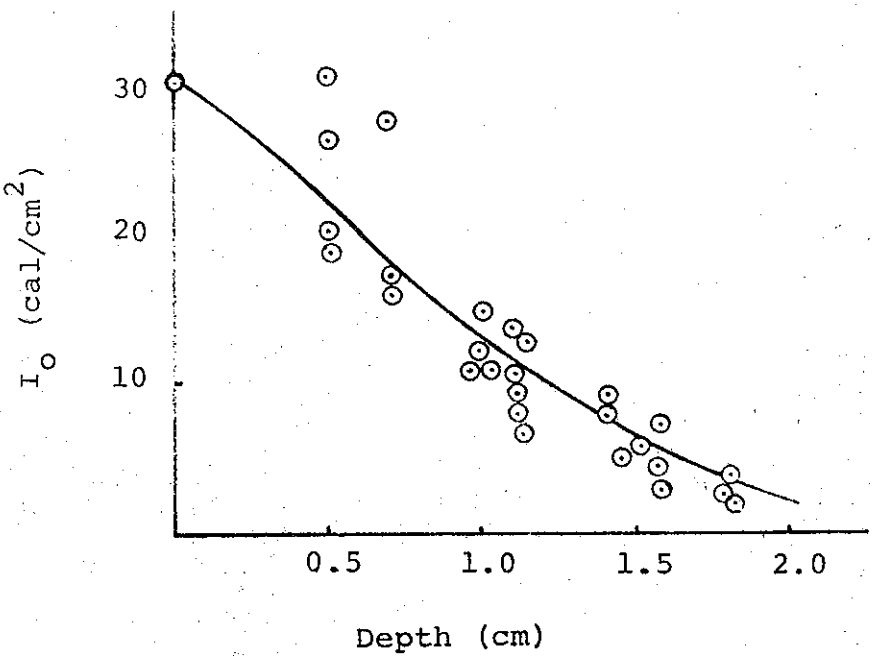

FIGURE B-16. SHOT 9663, CONFIGURATION I (COLLIMATOR PLATES), 1-mil TITANIUM SCATTERER, σ = 0.7 cm

5972

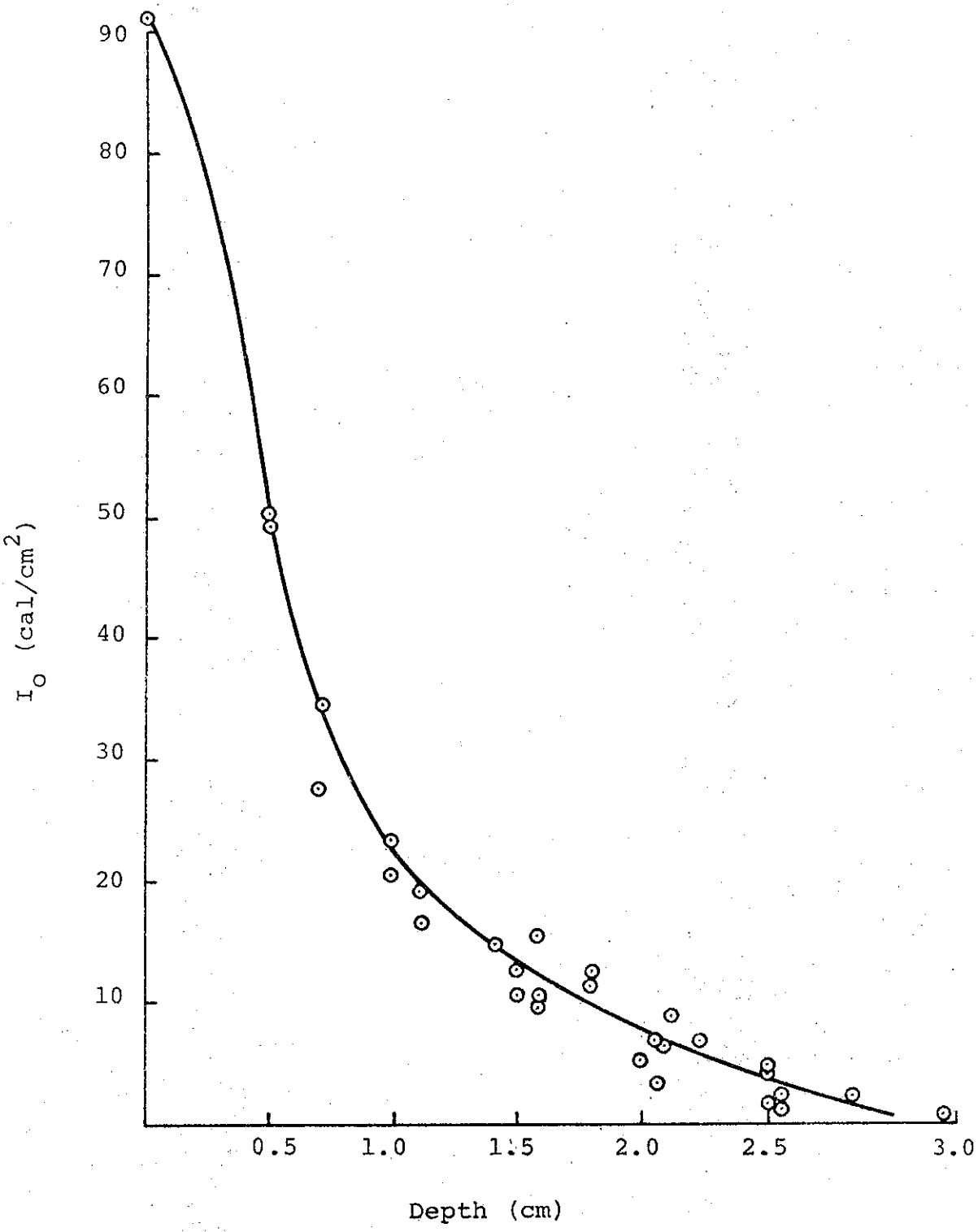

FIGURE B-17. SHOT 9686, CONFIGURATION II (CONE), NO SCATTERER, I_o = 91 cal/cm^2, σ_t = 0.45 cm

5246

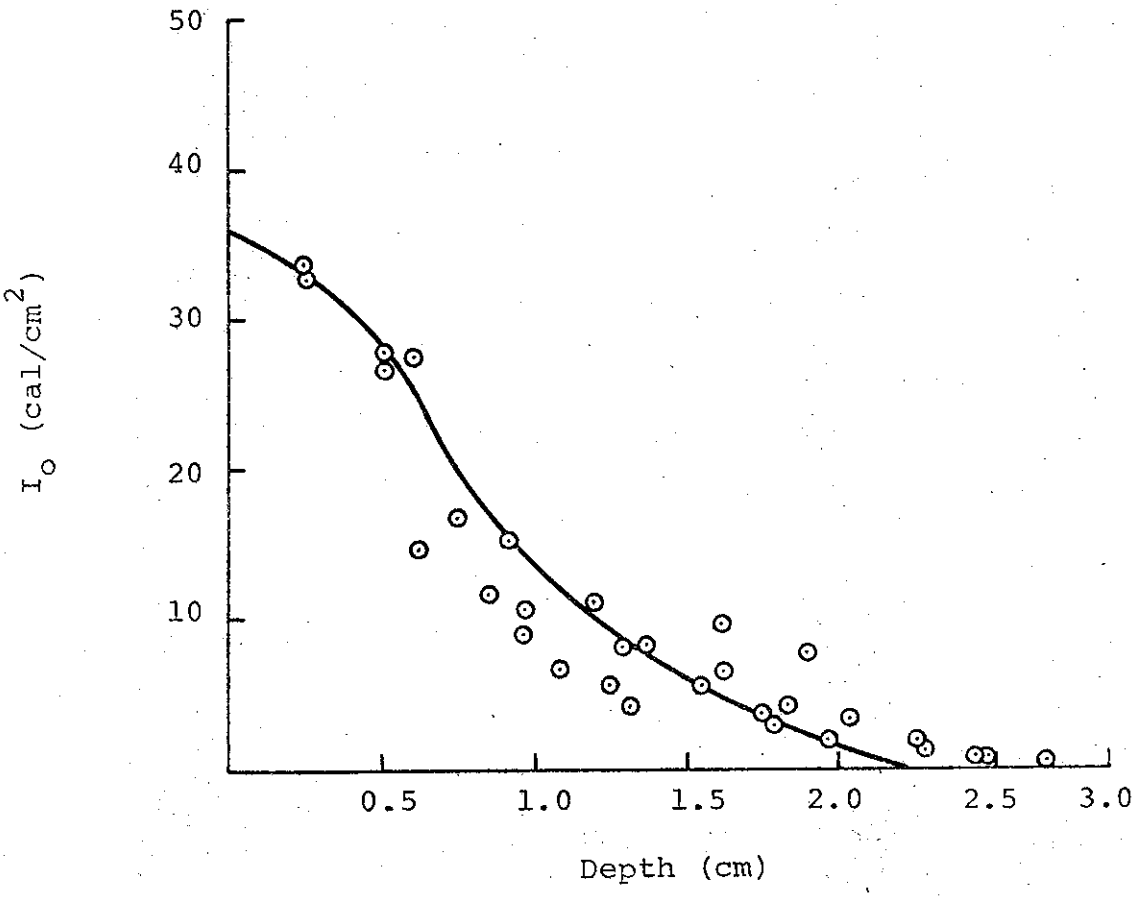

FIGURE B-18. SHOT 9692, CONFIGURATION II (CONE), NO SCATTERER, I_o = 35.5 cal/cm^2, σ_t = 0.7 cm

5953

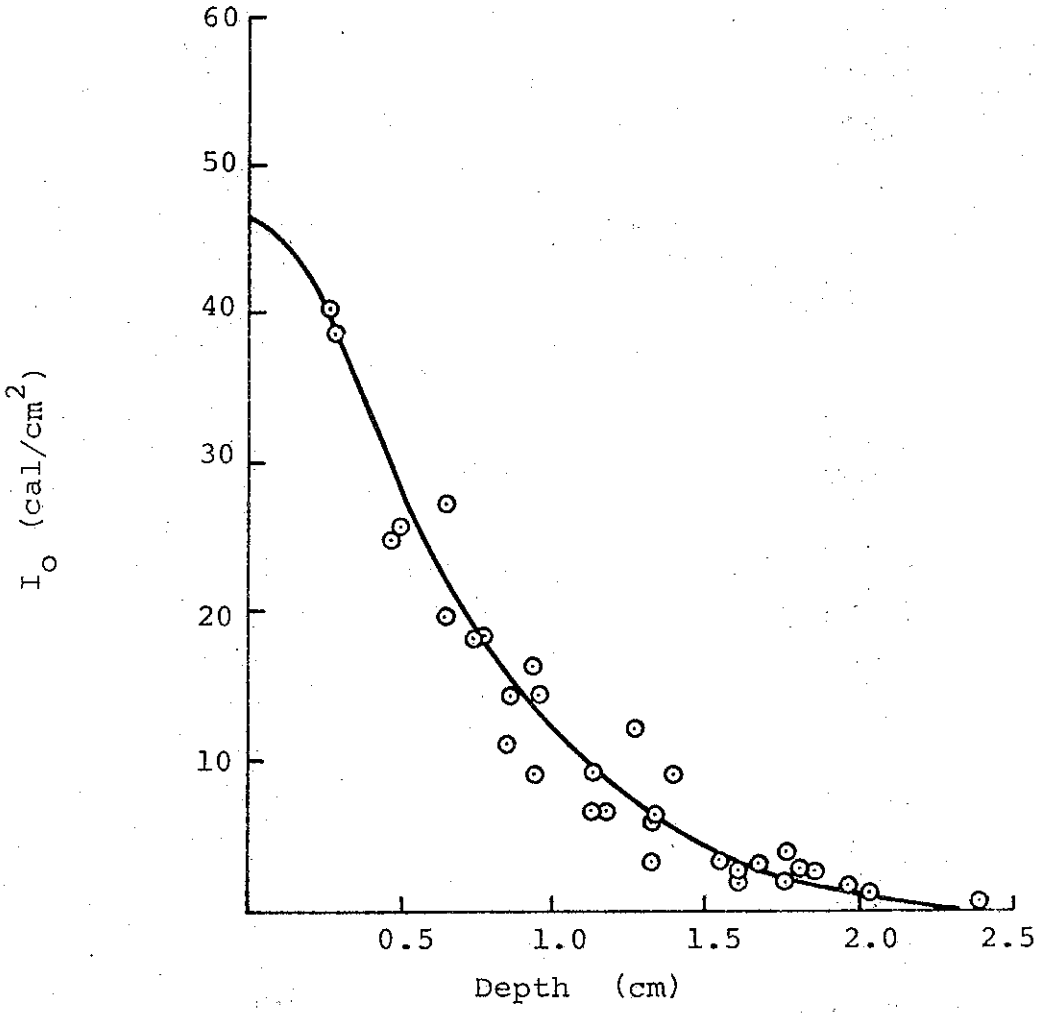

FIGURE B-19. SHOT 9691, CONFIGURATION II (CONE), 0.9-mil ALUMINUM SCATTERER, I_o = 46.5 cal/cm^2, σ_t = 0.51 cm

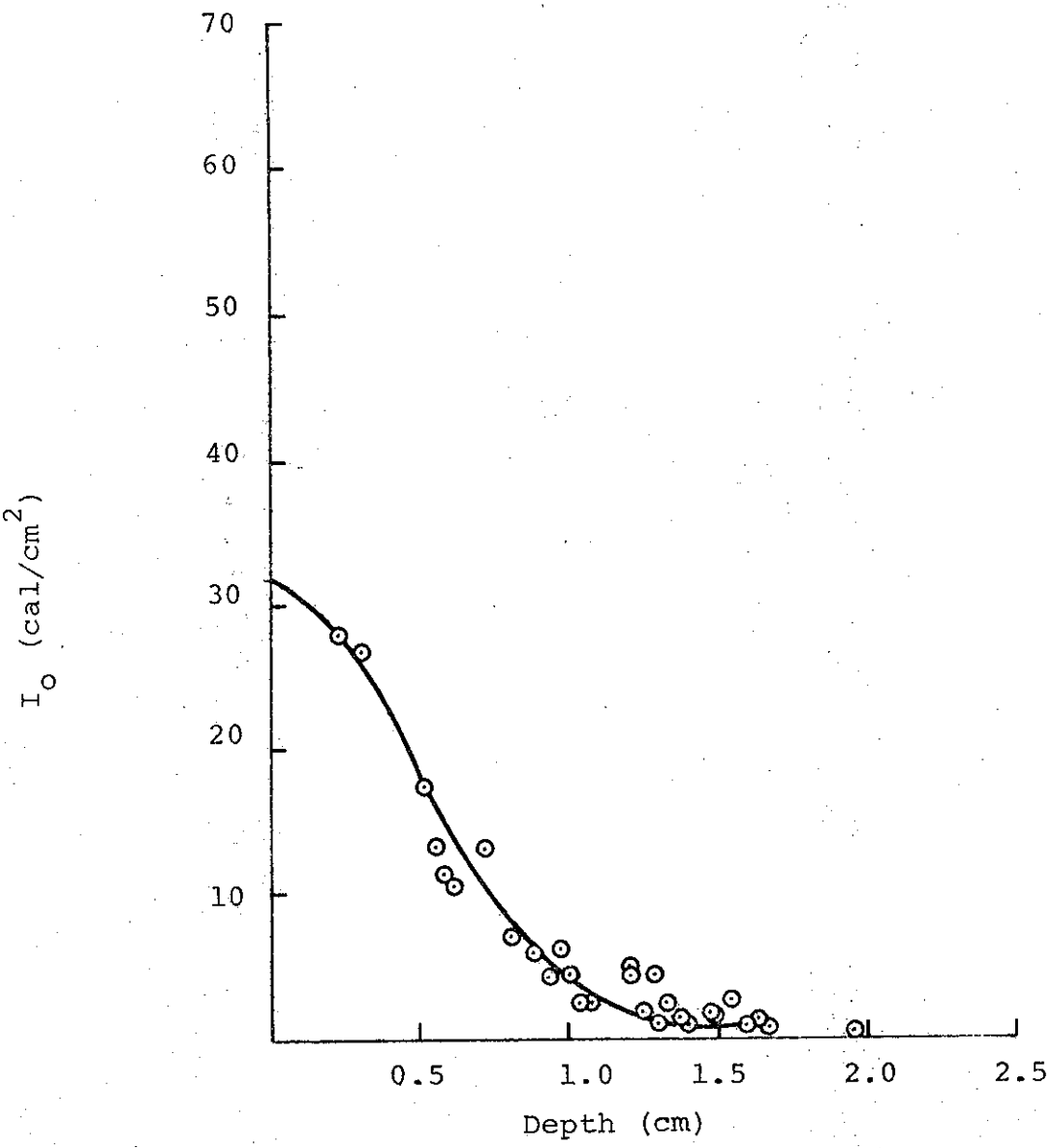

FIGURE B-20. SHOT 9688, CONFIGURATION II (CONE), 1.8-mil ALUMINUM SCATTERER, I_o = 31.5 cal/cm^2, σ_t = 0.47 cm

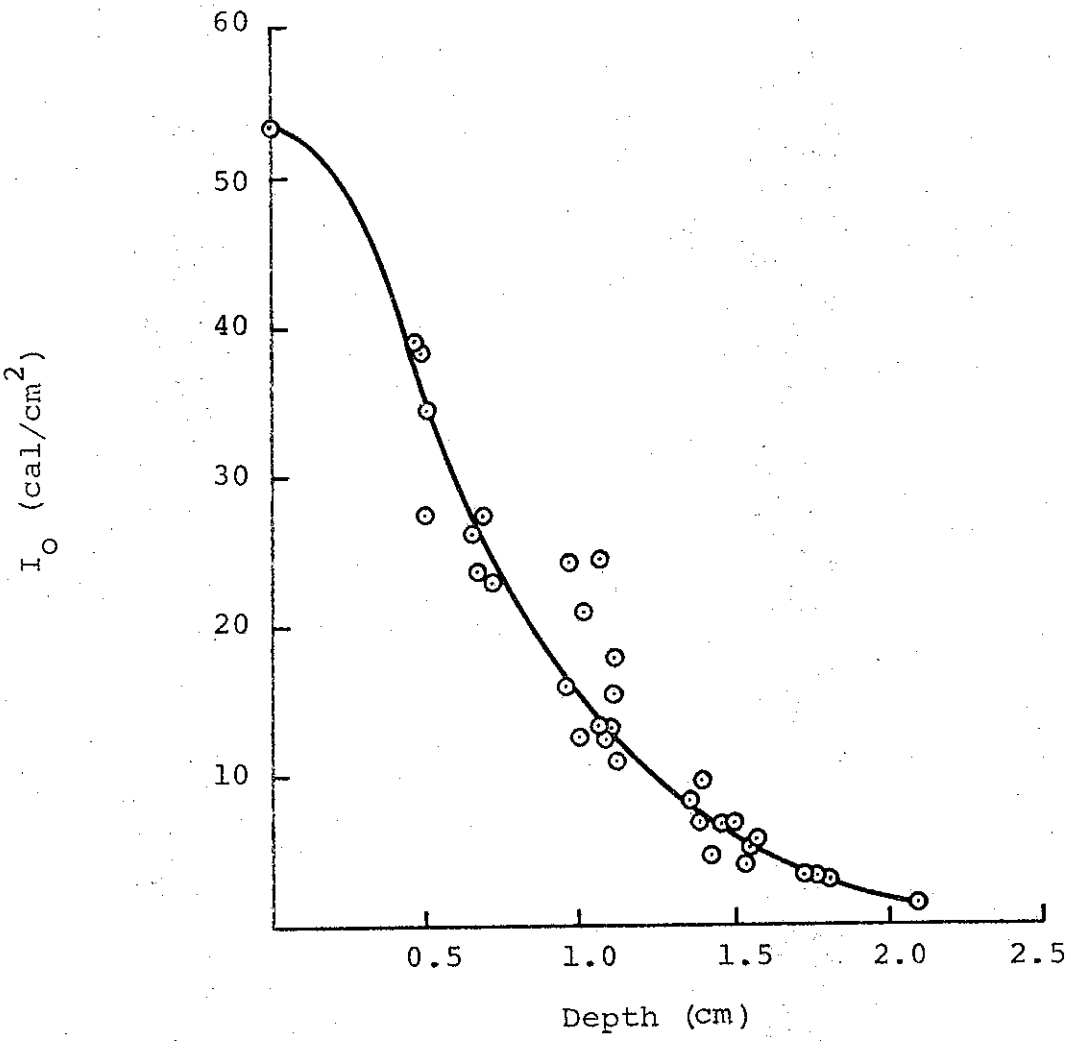

FIGURE B-21. SHOT 9690, CONFIGURATION II (CONE), 2.7-mil ALUMINUM SCATTERER, I_o = 53.5 cal/cm^2, σ_t = 0.55 cm

5950

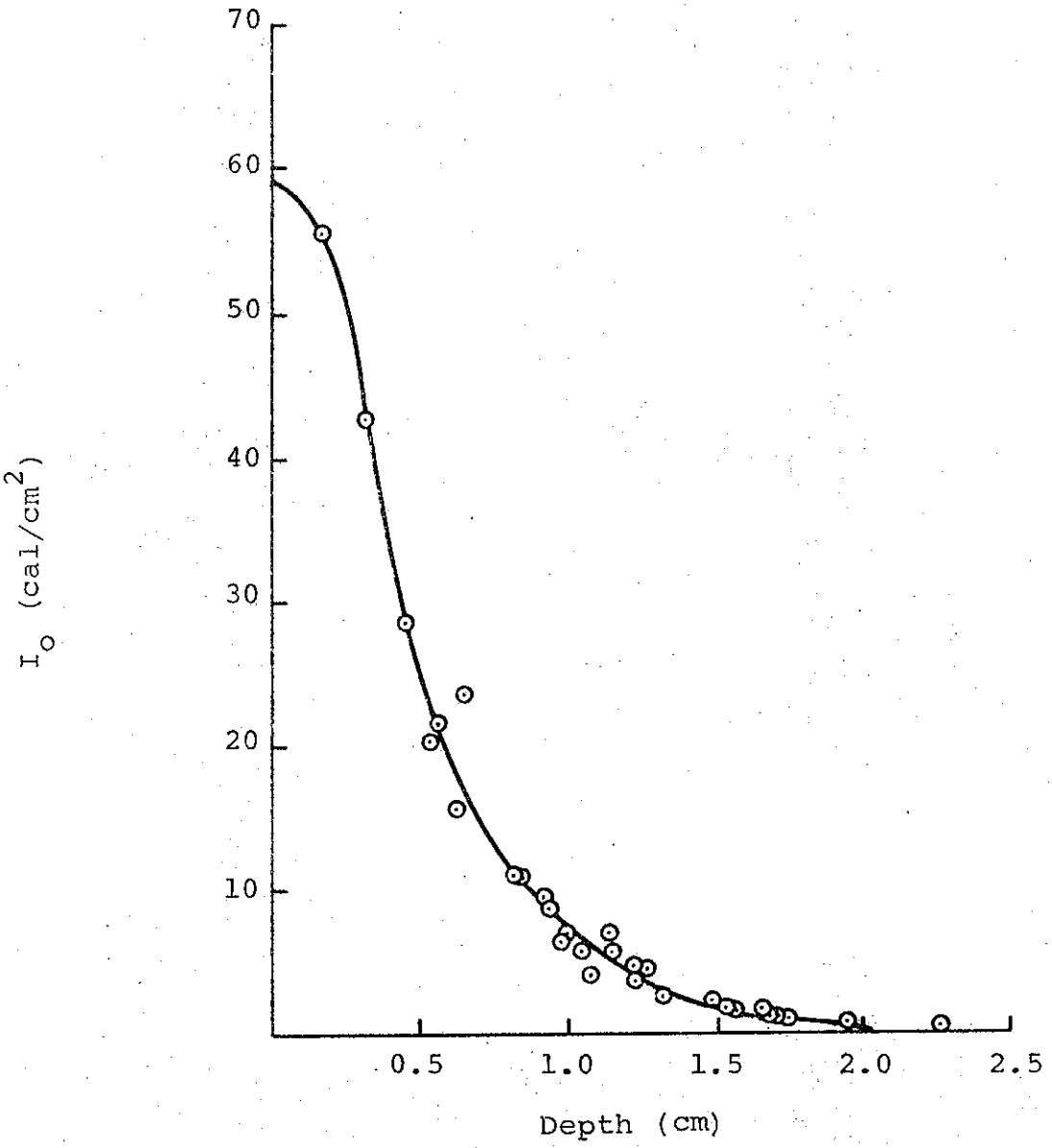

FIGURE B-22. SHOT 9689, CONFIGURATION II (CONE), 0.5-mil TITANIUM, I_o = 59 cal/cm^2, σ_t = 0.39 cm

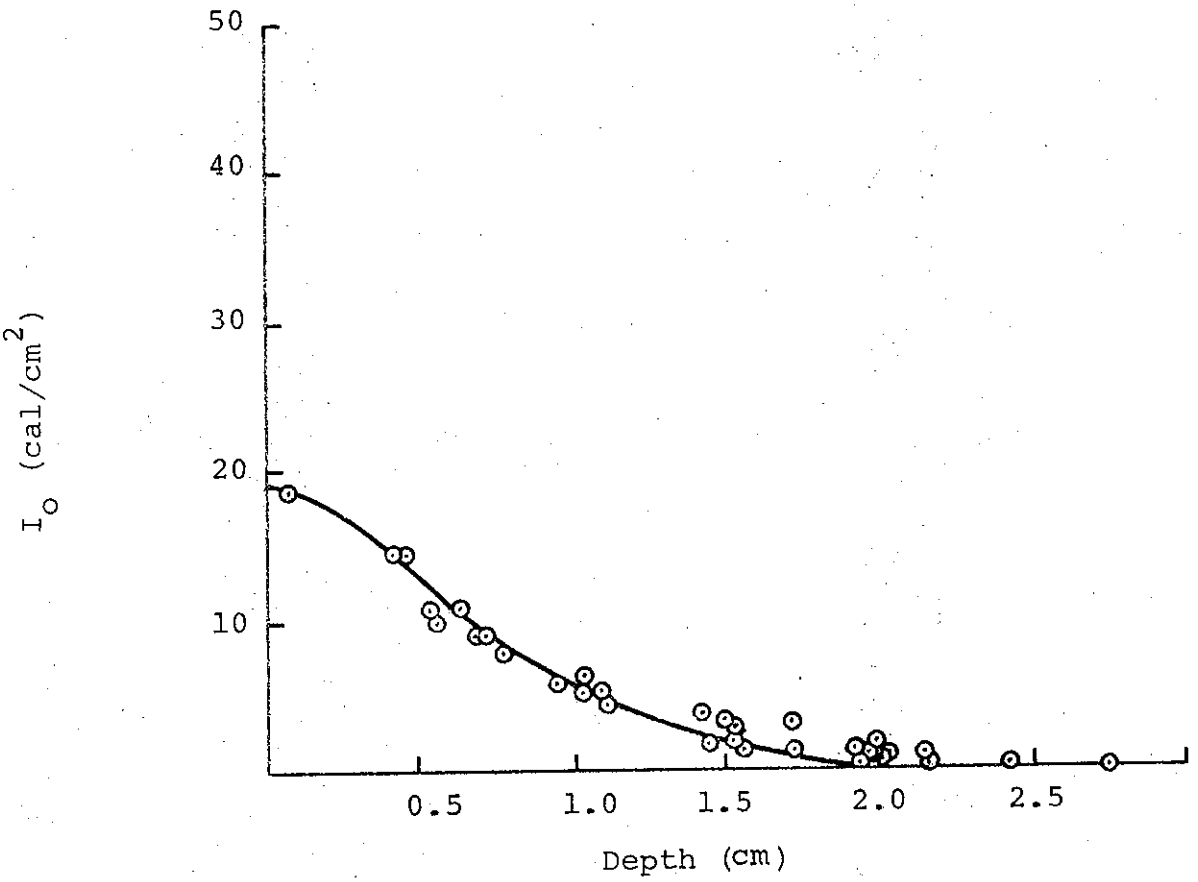

FIGURE B-23. SHOT 9687, CONFIGURATION II (CONE), 1-mil TITANIUM, I_o = 19.5 cal/cm^2, σ_t = 0.55 cm

APPENDIX C

COMPUTER CODE SCATT

The computer code SCATT calculates the multiple scattering distribution using the equations from the Molière theory.

It is assumed that the electrons are generated in a point somewhere on the axis. The energy spectrum is read in as a histogram distribution with a maximum of ten different energies and for each energy an intensity distribution on the anode-window can be chosen as

$$I(r) = a_o + a_1 r^{a_2} + a_3 \exp\,(a_4 r^{a_5}) \qquad (1)$$

where the variables a_o, a_1, ..., a_5, can be chosen for each energy. The thickness of the intermediate scatterer can be chosen as

$$T(r) = T_o + a_1 r^{a_2} + a_3 \exp\,(a_4 r^{a_5}) \qquad (2)$$

where the variables a_1, ..., a_5 are also arbitrary.

Cylindrical coordinates are used to divide the anode-window, the intermediate scatterer, and the target area into surface elements. The intensity due to scattering in an element chosen in the anode-window, is distributed directly onto the target area for electrons passing outside the intermediate scatterer. For electrons hitting the intermediate scatterer, one element is selected at a time and the intensity is redistributed on the target area. Analysis of the symmetry properties of the scattering geometry indicates that only one section of the anode-window and only the upper half of the intermediate scatterer would give the

desired result if the distribution on the target area was rotated and summed to its mirror image.

The cards to be included in the input data deck are described as follows. The options on the cards provide an indication of the versatility of the code.

Input Deck

Card No.	Format	Comments
1	20A4	Heading card. All 80 columns may be used.
2	2I4	First variable is a continuation demand if greater than 1. Second variable should be 1 for intermediate scatterer small (usual case), 2 if intermediate scatterer is large, 3 for no intermediate scatterer.
3	3(6X,F7.2), 2(5X,F8.2)	Anode window (1) thickness (mg/cm^2) (2) atomic No., (3) atomic mass, (4) distance from object (mm), (5) radius (mm).
4		Same for intermediate scatterer.
5		Same for target area. Only (4) and (5) are significant but other variables must have arbitrary (non-zero) values.
6	5F10.5	Coefficients for thickness modulation of intermediate scatterer (variables from Equation (2)).
7	6(2A4,I4)	Number of annulae and sectors for the three considered surfaces. NN1 refers to the number of concentric rings or annulae in which the anode-window is divided and

Card No.	Format	Comments
		KK1 refers to the number of sectors. They are to be read in the order: NN1, KK1, NN2, KK2, NN3, KK3. The only stipulation on the choice of values is that KK1 = KK3 (always).
8	2F7.3,2X,6F8.3	Kinetic energy (MeV), relative intensity (1.0 is max.) and variables in the intensity distributions from Equation (2).
9		There may be up to 9 additional "energy" cards each with the same format as card 8.
Last input card	2F7.3, 2X,6F8.3	The first variable should be greater than 90, the others are arbitrary.
Last card of set	I5,5X,10A4, 10X,5A4	The numeric variable on this card indicates the desired plotting. It should be 4 if no Cal-Comp plotting is desired, 2 if intensity plot in rectangular coordinates is desired and 0 if intensity per annulus should be plotted. The first alphanumeric variable is the heading above the plot and the second is the label on the X-axis of the plot.

There may be any number of similar data sets. After last data set there should be two cards to terminate the code. These are:

1	20A4	Anything
2	2I4	First variable is blank or 0 and second is arbitrary.

APPENDIX D

QUADRUPOLE CODE

SECTION I

DESCRIPTION OF CODE

The following data are input for quadrupole calculations:

1.	EEE	the kinetic energy in MeV
2.	HHH	the effective length of quadrupole fields in centimeter
3.	SSS	the separation of quadrupole fields in centimeter
4.	$\phi\phi\phi$	the object distance from first quad in centimeter
5.	NGRAD1, NSTEP1	the first value of field gradient and the step in field gradient in the first quad, both in G/cm
6.	NGRAD2, NSTEP2	the corresponding quantities for second magnet

The code takes a set of gradients in the two quads and calculates the focusing-defocusing focal length (ZFD) and the defocusing-focusing focal length (ZDF) in centimeter, measured from the edge of the effective field of the second quad. In addition, the focal distances for the first quad, ZF and ZD, are also computed.

The EEE parameter varies fastest (innermost do-loop), followed by $\phi\phi\phi$, SSS, and HHH in that order. HHH must be the same for both quads.

A negative distance means (as in optics) that the focal point lies to the left of the reference plane (diverging rays). Figure D-1 illustrates the various parameters.

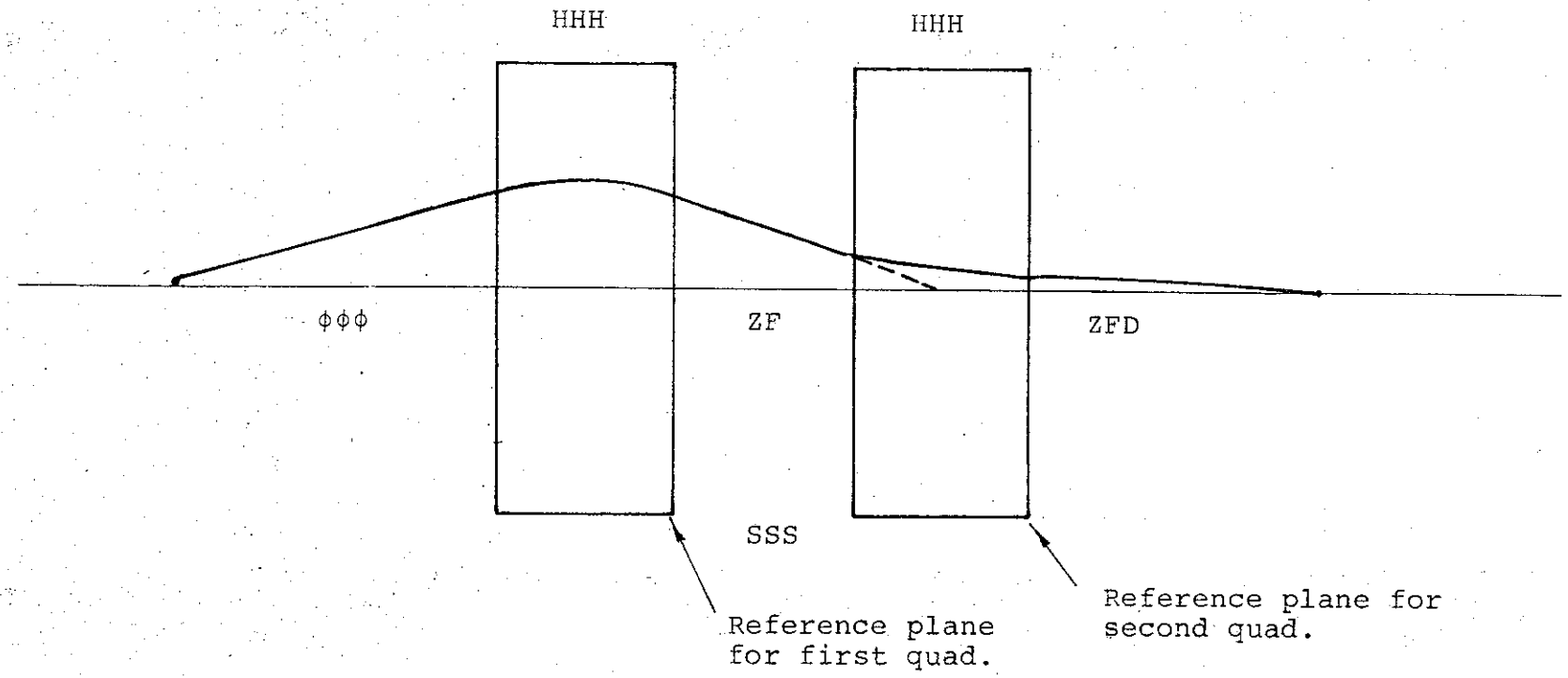

FIGURE D-1. PARAMETERS USED IN QUADRUPOLE CODE

SECTION II

HOW TO USE CODE

Between [11EXEC] and [1*] the following data cards should be inserted:

1. EEE, the kinetic energy in MeV. Format is 10H, 10F7.2: column 1 is blank. Columns 2 to 10 are for label. If EEE > 7900, then no run is made for this value.

2. HHH, the effective length of quadrupole field in cm. Format is 10H, 10F7.2: Column 1 is blank. Columns 2 to 10 are for label. If HHH > 900, then no run is made for this value.

3. SSS, the separation of the quadrupole fields in cm. Format is 10H, 10F7.2: Column 1 is blank. Columns 2 to 10 are for label. If SSS > 900, then no run is made for this value.

4. $\phi\phi\phi$, the object distance from the first quadrupole in cm. Format is 10H, 10F7.2: Column 1 is blank. Columns 2 to 10 are for label. If $\phi\phi\phi$ > 900, then no run is made for this value.

5. NGRAD1, NSTEP1, NGRAD2, NSTEP2, the initial value of the field gradient and the delta step in the field gradient in both magnets in gauss/cm. Column 1 is blank, 2 to 20 for label, I5, 26 to 35 for label, I5, 41 to 60 for label, I5, 66 to 75 for label, I5.

6. Continuation card: If this card has the letters b CONTINUE in columns 1 to 8 (9 to 80 optional) a new data set is read in. All other formats give STOP.

SECTION III

CODE OUTPUT

The code first prints out the input data EEE, HHH, SSS, and $\phi\phi\phi$ complete with labels. Then for each combination of input parameters, the code prints out a 14 x 14 array. Each element in array consists of two numbers, ZFD and ZDF. The rows of the array are labeled by the field gradient in the first quadrupole, and the columns are labeled by the field gradient in the second quadrupole. In addition, a fifteenth column is included which contains ZF and ZD for the first magnet only.

For a given combination of EEE, HHH, SSS, and $\phi\phi\phi$, the two quad system is said to have focused the beam for that combination of field gradients for which ZFD and ZDF are positive and equal.